NUMERICAL INVESTIGATION OF TEMPERATURE DISTRIBUTION ON A HIGH PRESSURE GAS TURBINE BLADE

A Thesis

by

HOOTAN ZIRAKZADEH

Submitted to the Office of Graduate and Professional Studies of
Texas A&M University
in partial fulfillment of the requirements for the degree of

MASTER OF SCIENCE

Chair of Committee,	Je-Chin Han
Committee Members,	Hamn-Ching Chen
	Sy-Bor Wen
Head of Department,	Andreas A. Polycarpou

August 2014

Major Subject: Mechanical Engineering

ABSTRACT

A numerical code is developed to calculate the temperature distributions on the surface of a gas turbine blade. This code is a tool for quick prediction of the temperatures by knowing the boundary conditions and the flow conditions, and doesn't necessarily provide the most accurate results that could be obtained by performing an experiment or precise CFD simulations. Different systems of blade external and internal cooling, such as rib turbulated cooling, impingement cooling, pin-fins, and injection holes for film cooling, are considered in the code by using the appropriate correlations or factors.

When the code is run and the results are obtained a gas turbine blade designer can modify his blade terms and conditions such as mass flow rate, number of injection holes in each passage, even the blade material thickness to find an optimum design for cooling purposes. Code is first applied to an E^3 blade; the external heat transfer coefficients for this blade is inserted as a known boundary condition; Next, code is run for the same blade but this time using the flat plate and convectional correlations for predicting transition on suction side of the blade for external heat transfer coefficient. This code provides an easy way to get a better understanding of the cooling design and its ability to be modified for any gas turbine blade makes it more flexible to be developed as a commercial tool in future. In the next step, code is applied to a Samsung-Rotor2 blade with different cooling design than an E^3 blade and results are presented. Another part is introduced to this project by running a CFD simulation using commercial

software Fluent and Gambit, to capture heat transfer coefficient distributions around the surface of the blade and the obtained values is used back in the code. In the meanwhile some interesting observations made during the CFD simulation is discussed. The CFD simulation is performed for the cases where there are not any data available for external heat transfer coefficient distribution already. Two turbulence models, k-epsilon and SST-Transition were utilized for the 2D CFD study; and for the 3D CFD case, only k-epsilon model was applied. It was revealed that even though SST- Transition has a better prediction of Mach number, but in terms of heat transfer coefficient k-epsilon model provides closer values to the reference values from previous works. Finally, combining the code and the CFD results could act as a useful assistant to give a designer a general and quick idea of how his blade design will perform at the end.

ACKNOWLEDGEMENTS

I would like to thank my advisor, Dr. Han for his support and guidance all through this project. I would also like to thank Dr. Chen and Dr. Wen for being part of my advisory committee.

It is also worth mentioning that this project was sponsored by Samsung Techwin, South Korea, and the code was co-developed by the project co-worker Mr. Nafiz Chowdhury.

Finally, I would also like to thank my colleagues and friends who provided me assistance during this time. So, my appreciations goes to Belal Krad, Hao-Wei Wu, Hung-Chieh Chu, Kun Lu, Nafiz Chowdhury, and Shang Feng Yang, I heartily appreciate all of the help and support that you gave me.

NOMENCLATURE

Symbols

c_p	specific heat of gas (J/KgK)
d	Impingement hole diameter (m)
D	Diameter of leading edge (m)
D_h	hydraulic diameter of the ducts (m)
f	Friction factor
h	Heat transfer coefficient $\left(\frac{W}{m^2K}\right)$
k	thermal conductivity
MPRBL	Backward Loop
N	Rotational speed (rpm)
Nu	Nusselt number
Pr	Prandtl Number
PS	Static pressure (Pa)
q''	Heat flux $\left(\frac{W}{m^2}\right)$
Re	Reynolds number based on hydraulic diameter
SPRBL	Forward Loop
T	Temperature (^oC)
TCF	Temperature of coolant fluid (^oC)
TFILM	Temperature of film (^oC)

TTBCS	Surface temperature of TBC on suction side(^{o}C)
TTBCP	Surface temperature of TBC on pressure side(^{o}C)
TWIP	Inner pressure side wall temperature of blade (^{o}C)
W, $\dot{m}$	Mass flow rate $\left(\frac{Kg}{s}\right)$
X	Distance from injection hole (m)
η	Effectiveness
μ_2	Coolant viscosity at the injection point (Pa-s)
μ_∞	Mainstream viscosity (Pa-s)

Subscripts

1	At inlet of element
2	At exit of element
25	Core compressor inlet plane
f	Film
cf	Coolant fluid
i	Internal
ip	Injection pressure side
is	Injection suction side
p	Pressure side
r	Recovery
s	Suction side
TBC	Thermal barrier coating

TABLE OF CONTENTS

Page

Page

LIST OF FIGURES

Page

Page

Page

Page

Page

LIST OF TABLES

Page

INTRODUCTION AND LITERATURE REVIEW

Internal Cooling

Historically, Turbomachinery components efficiencies in prototype engines fall short of design goals by significant amounts [1]. Modern development in turbine-cooling technology plays a critical role in increasing the thermal efficiency and power out-put of advanced gas turbines [2]. As a turbine's rotor inlet temperature increases, the thermal efficiency and power output increases, too. This fact is clearly depicted by Sautner et al [3] from Pratt & Whitney group in Figure 1. Therefore, to achieve higher performance, the rotor inlet temperatures (RIT), especially in the modern gas turbines, are much higher than even the melting point of the blade material; and, this urge to increase the power output and the drawback of having very high temperatures, makes the need to have better cooling design for the blade essential and inevitable.

The engine cooling system must be designed to ensure that the maximum blade surface temperatures and temperature gradients during operation could be reached without exceeding maximum allowable thermal stresses for the life of the design. Also, the amount of coolant taken from the compressor plays an important role in the final performance of a gas turbine engine. Too little coolant could result in a reduction of the components life duration and too much coolant could result in the reduction of the gas turbine engine performance. Therefore, being able to predict the temperature distribution on the blade's surface while adjusting for the coolant's mass flow rate seems to be an important key-point with which a more advanced design could be approached.

A gas turbine blade uses both internal cooling and external cooling techniques to be protected from very high temperatures of combustion materials. Below, there is a short summary of these cooling methods. For more detailed assessment of these techniques, one could refer to the chapter four of Han et al [2] where many different cooling techniques are presented. According to Han et al [2], a gas turbine cooling system could be divided in three major regions: leading edge, mid-chord section, and trailing edge. After long-time research in the field it has become a common view that leading edge should be cooled down by a jet impingement arrangement, the midchord section of the blade should be normally cooled by serpentine rib-roughened coolant passages, and the trailing edge should be typically cooled by pin-fins or dimpled surfaces. A schematic of these different configurations is shown in Figure 2 [4]. In this study, a combination of these cooling techniques is considered for blade cooling purposes and appropriate formulas and correlations are implemented into the code for these various regions to calculate the rotor blade's surface temperature distributions.

Rib-Turbulated Cooling

Rib-turbulators are cast on the internal walls of a serpentine channel in order to enhance heat transfer by creating more turbulence and also providing more surface area. Heat is conducted from the combustion materials to the external area of the blade and then moves toward the core of the blade and is removed by the internal flow. These ribs enhance the contact area between the internal cooling flow and the blades solid material. Han [5] performed an experimental study of fully developed turbulent air flow in square ducts with two opposite rib-roughened walls to determine the effects of the rib pitch-to-

height and rib height-to-equivalent diameter ratios on friction factor and heat transfer coefficients with Reynolds number varied between 7000 and 90,000. Based on the four-sided, smooth-duct correlation and the four-sided, ribbed-duct similarity law, a general prediction method for average friction factor and average Stanton number in rectangular ducts with two smooth and two opposite ribbed walls was developed. They concluded that the heat transfer performance for a non-rotational ribbed channel depends mostly on the channel aspect ratio of the channel.

Flow separation in channels with the presence of the ribs, and the effect of rib arrangement in this separation, have been the topic of many different research works. Two of the most important parameters affecting this re-attachment are height of the rib and the ribs spacing known as pitch of the ribs; these two parameters heavily affect the region where the flow separation starts to occur and also the region of re-attachment (see Figure 3 provided by Han et al [2]). The vortices and turbulent flow made by ribs increases heat transfer coefficients, but in the meanwhile the drawback of higher pressure drop is present, too.

Also, many research has been done to figure out the best alignment of the ribs for reaching to higher heat transfer coefficients while having lower pressure drops. Han and Park [6] investigated the heat transfer enhancement for the case of an angled rib with respect to the incoming flow. They concluded that the angled rib configurations had increasing centerline Nusselt number ratios after the fully developed region due to the secondary flows created by the angled ribs. Han and Zhang [7] studied the effects of continuous and broken ribs. The results indicated that for 60̊ and 45̊ broken ribs, Nusselt

number ratios are much higher than the continuous ribs; in the same time, the friction factors were relatively the same for both cases.

Pin-Fin Cooling

Pin-fins increase the heat transfer coefficient by increasing the contact surface area between the fluid and the solid material of the blade. Pins add to the free stream turbulence levels and create vortices which result in higher heat transfer coefficients. These vortices originate from two locations, one at the wake of the pins, and the other one, Horseshoe vortices build up at the upstream base of the pin. Similar to the ribs, the drawback of using pins is having noticeable pressure drops. Pin-fins are usually installed on the trailing edge section of a gas turbine blade since there is limited spacing for application of other methods such as rib turbulators or jet impingement. They usually expand along the entire span of channel from bottom wall to the top wall.

One interesting observation with pin-fins is the trend in change of heat transfer coefficient at the start of the channel. For a smooth channel, Nusselt numbers are highest at the start of the channel, where boundary layer starts to develop, and as we move toward the downstream side and fully developed flow, Nusselt number values drop. In in Pin-finned channel, right after the inlet, there is an increase in the Nusselt number amount. This could be attributed to the presence of horseshoe vortices which are created after the first row of pins. And then, these vortices move to the downstream and result in the increase of Nusselt numbers in those regions, too. Therefore, since the turbulence increases as the flow proceeds to the following rows, the localized Nusselt number gradually increases.

The effect of arrangement of pin-fins on heat transfer has been investigated by Chyu, M.K. et al [8]. It is shown that the staggered arrangement has slightly higher Sherwood number values than the in-line arrangement.

Jet Impingement Cooling

Jet impingement cooling is the most effective way of increasing heat transfer coefficients locally and that's why this method is used in the leading edge of the gas turbine blade where thermal loads are the highest. Like other techniques, the first disadvantage of this method is its pressure drop; second, the implementation of impingement jet cooling into the body of the blade results in hollow spaces and makes the blade structure weaker. Research by Wright and Han [9] has shown that with increasing Reynolds number, decreasing jet-to-target spacing, or decreasing jet-to-jet spacing the heat transfer coefficient on the targeted surface increases. In this study, related correlations for prediction of internal heat transfer coefficient at the leading edge are utilized.

Turn Effect

The internal cooling passage of the blade is a multi-pass serpentine channel with several turns at its path. This turn in the flow direction results in a flow attachment and change of heat transfer coefficients in this zone. This effect is called the "Turn Effect". Ekkad and Han [10] used liquid crystal transient thermography technique to analyze the heat transfer coefficient distributions of two-pass square channels with 180 degree turn. Surface of the blade was covered with liquid crystal spray and surface temperature was recorded. After calculating the heat transfer coefficients it was found that the Nusselt

number ratio (Nu/Nuo) in second passage is nearly 2-3 times higher than it is in first passage due to the turn effect. In this project a factor is considered for this effect in each element in the turn portion of the channel.

Effect of Blowing Ratio

Blowing ratio (M) is defined as:

$$M = \frac{\rho_c V_c}{\rho_m V_m} \tag{1}$$

where ρ_c is the coolant density, V_c is the coolant velocity, ρ_m is the mainstream density, and V_m is the mainstream velocity. Blowing ratio is a representation of mass flux ratio between coolant jet and the mainstream flow. With an increase in the blowing ratio, film cooling effectiveness increases up to some point, and after that, further increase would result in the reduction of film cooling effectiveness. This is due to the penetration of the jet into the mainstream flow and the lift-off effect. Blowing ratio in this project plays a role in the calculation of effectiveness correlation introduced by Jabbari and Goldstein [11].

Effect of Free-Stream Turbulence

In a real gas turbine engine, after the combustor turbulence intensities are high and they affect the heat transfer coefficient values over the blade's surface. The range of turbulence intensities at the inlet of a first stage gas turbine rotor is somewhat between 7 to 20 percent. As flow moves to the downstream side, turbulence intensity starts to decay. In this project a turbulence intensity of 15% was considered at the inlet of the rotor stage for the CFD simulation.

Blade's Tip Portion

The tip of a gas turbine goes under very large thermal loads which could result in the tip failure and melt-down of this section. These high thermal loads are due to the very large temperatures of hot gases flowing over the gap between the tip and shroud of turbine cascade. Then, since the gap is narrow and there is huge pressure difference between the pressure side and suction side of the blade, flow starts to accelerate and this acceleration leads to a thin boundary layer and very high heat transfer coefficients. Another drawback of hot gas flowing through the gap is the increase in losses, and as a consequence loss of efficiency.

There are some ways to increase the efficiency for instance by using the squealer shaped tips instead of the smooth ones. Metzger et al.[12], and Chyu et al. [13] performed experiments on a squealer tip using varying depth to width and gap to width ratios. They concluded that for a given pressure difference across the gap there is an optimum value of depth to width ratio. After this ratio, no further flow reduction will occur.

As a first step, in this project, the tip portion is chosen to be smooth for the CFD simulation; Cases such as a squealer shaped tip is a potential topic for future works.

Computational Fluid Dynamics (CFD)

Computational fluid dynamics (CFD) is trending to become an essential design tool in the gas turbine world due to its cheaper, and at the same time, faster performance in comparison to conduct physical experiments.

Many computational studies on various aspects of gas turbine blades have been done by different groups. One of the CFD works which has considered for the tip clearance, too, is done by Yang et al. [14]. They simulated the leakage flow and heat transfer on a flat tip, a double squealer tip and a single suction-side squealer tip of a scaled up GE-E³ blade. The simulation results showed that the heat transfer coefficient decreases with increasing squealer cavity depth, but the shallow squealer cavity is the most effective configuration to reduce the heat load in the blade tip region.

There are numerous other CFD works related to the gas turbines in the literature (Chen et al [15], Wei et al [16]).

Research Objectives

A numerical code is developed to calculate the temperature distributions on the surface of a gas turbine blade. This code is a tool for quick prediction of the temperatures by knowing the boundary conditions and the flow conditions, and doesn't necessarily provide the most accurate results that could be obtained by performing an experiment or precise CFD simulations. Different systems of blade external and internal cooling, such as rib turbulated cooling, impingement cooling, pin-fins, and injection holes for film cooling, are considered in the code by using the appropriate correlations or factors.

When the code is run and the results are obtained a gas turbine blade designer can modify his blade terms and conditions such as mass flow rate, number of injection holes in each passage, even the blade material thickness to find an optimum design for cooling purposes. Code is first applied to an E³ blade; the external heat transfer

coefficients for this blade is inserted as a boundary condition from the work of Halila et al[1]; Next, code is run for the same blade but this time using the flat plate and convectional correlations for predicting transition on suction side of the blade for external heat transfer coefficient. This code provides an easy way to get a better understanding of the cooling design and its ability to be modified for any gas turbine blade makes it more flexible to be developed as a commercial tool in future. In the next step, code is applied to a Samsung-Rotor2 blade with different cooling design than an E^3 blade and results are presented. Another part is introduced to this project by running a CFD simulation using commercial software Fluent and Gambit, to capture heat transfer coefficient distributions around the surface of the blade and the obtained values is used back in the code. In the meanwhile some interesting observations made during the CFD simulation is discussed. The CFD simulation is performed for the cases where there are not any data available for external heat transfer coefficient distribution already. Two turbulence models, k-epsilon and SST-Transition were utilized for the 2D CFD study; and for the 3D CFD case, only k-epsilon model was applied. It was revealed that even though SST- Transition has a better prediction of Mach number, but in terms of heat transfer coefficient k-epsilon model provides closer values to the reference NASA report [1].Finally, combining the code and the CFD results could act as a useful assistant to give a designer a general and quick idea of how his blade design will perform at the end.

The work in this thesis is an extended version of the final report written for accomplishment of a sponsored project by Samsung Techwin [17].

GOVERNING EQUATIONS AND MODEL DESCRIPTION

Initially, this model is approximated as a one-dimensional system which, after breaking down the blade to a set of discretized elements, the related formulas and correlations are applied to each element. According to this convention, the blade must be divided into discrete elements of same size in the chord and span directions; this has been done for an E^3 blade as seen in Figure 4. The choice of element numbers in the chord direction depends on the size and number of internal coolant passages. The blade will necessarily be divided at the centerline of each duct wall so that each element is as wide as the coolant duct associated with it plus half of each duct wall (see Figure 4). The choice of dimension of the element in the span direction is fully independent and is a compromise between increased accuracy (see Figure 4). Further, at each unit, mass is allowed to enter or leave the system but heat may not be transferred by conduction. Heat is transferred at the artificial divisions only as an increase in the internal energy of the mass transferred. Conduction is allowed in this model only from external blade surface into the internal coolant duct. In each finite element, convection is seen to be the primary method of heat transfer. Finally, the model is constructed from an energy balance and continuity equations for a discreet, one-dimensional finite element.

Also, the blade's geometry, from both side and top views including all the ducts' and elements' geometrical values used in the code, are presented in Figure 5 [2] and Table 1.

Table 1- E³ blade detailed ducts and elements geomtrical values

Rib Thickness	0.00115 m

Duct No	Width of the element along pressure side (m)	Width of the element along Suction side (m)	X-sectional Area, A_c (m^2)	Perimeter,P (m)	Hydraulic Dia,D_H(m)
1(LE)	0.00187325	0.00187325	1.51946E-06	0.005605	0.001084358
2	0.002065	0.002065	1.02498E-05	0.01189735	0.00344608
3	0.00160185	0.0031211	1.25318E-05	0.01544915	0.003244656
4	0.0028615	0.0028615	1.35091E-05	0.0150332	0.003594462
5	0.0008437	0.0008437	2.84624E-06	0.0086199	0.001320776
6	0.0016815	0.0016815	4.9465E-06	0.009204	0.002149718
7	0.00553125	0.006549	4.66672E-06	0.0140066	0.001332719
8(TE)	0.010325	0.010325	6.09175E-06	0.02183	0.001116216

Total length of Pressure side (m)	Total length of Suction side (m)
0.0329869	0.04351545

Calculation of Convective Heat Transfer Coefficients

The convection (internal and external) and conduction through the suction and pressure side of the blade are calculated using experimental correlations, described in the following paragraphs.

External heat transfer coefficient calculation

The external heat transfer coefficients are calculated based on two physical models. The first model assumes that at the leading edge of the blade the heat transfer coefficient may be estimated by flow over a cylinder.

$$h_{c\phi} = 1.14\left(k_f/D\right)(\rho V_\infty D/\mu)^{0.5}\Pr^{0.4}(1-(\phi/90)^3)\ \ [0^o < \Phi < 90^o] \qquad (2)$$

In the second model, the convective heat transfer coefficient is calculated for the rest of the curve length along the suction and pressure side by simulating as external flow over flat plate. The heat transfer coefficient is estimated using the following laminar and turbulent correlations. The appropriate equation is chosen based on the

critical Reynolds number (Re_c=3X10^5). As the oncoming flow contains high free stream turbulence (FST) in it and roughness on the blade surface lead to the early transition, so to consider all the effects it is required to consider that specific value of critical Reynolds number.

$$h_x = 0.332 \ \frac{k}{x} \ Re_x^{1/2} \ Pr^{1/3} \ [\text{Laminar}] \tag{3}$$

$$h_x = 0.0288 \ \frac{k}{x} Pr^{1/3} Re_x^{0.8} \ [\text{Turbulent}] \tag{4}$$

Internal heat transfer coefficient calculation

The internal convective heat transfer coefficient of the model will be computed for three different possibilities based on particular blade design. The internal convective heat transfer coefficient for the central region of the blade element will be estimated using conventional Dittus-Boelter equation for forced convection through a smooth duct using equation 5. This equation is only applicable for turbulent flow inside a duct.

$$\bar{h}_c = 0.023 \ \left(\frac{k}{D_H}\right) Re_x^{0.8} Pr_f^{1/3} \tag{5}$$

To enhance the blade cooling efficiency, modern design of turbine blade includes turbulence promoters called rib tabulator. Based on experiments, heat transfer can be improved from 2 to 3.0 times than that of smooth surface. Thus, initially heat transfer coefficient is computed considering smooth surface and then it is enhanced by a factor in present case it is 2.0. Again, if there any turning at the hub or tip, then the heat transfer coefficient is estimated as 2.0 times of that.

$$\frac{h_{TP}}{h_{smooth}} = 2.0 \tag{6}$$

$$\frac{h_{\text{Turning Region}}}{h_{\text{Straight Region}}} = 2.0 \tag{7}$$

The leading edge portion of a turbine blade is the most crucial part as it sees the high inlet temperature. Thus, special treatment has been taken under the consideration. Jet impingement cooling scheme is employed inside the leading edge where coolant stream is directed to hit the surface at regular intervals. This heat transfer coefficient is computed using the equation (8).

$$\bar{h}_c = 0.63 \ \frac{k}{d}(Re)^{0.7}\left(\frac{d}{S}\right)^{0.5}\left(\frac{d}{D}\right)^{0.6} \exp\left[-1.27\frac{l}{d}\left(\frac{d}{S}\right)^{0.5}\left(\frac{d}{D}\right)^{1.2}\right] \tag{8}$$

where k is coolant fluid thermal conductivity, d is Impingement hole diameter, S is distance between impingement holes, l is jet to target plate separation distance, and D is diameter of the target plate (leading edge).

Due to external flow acceleration and the resultant increase in the external convective heat transfer coefficient, it is essential to achieve higher value of internal convective heat transfer coefficient on the trailing edge. That's why pin-fin arrangement is employed to obtain higher value of convective heat transfer.

$$\bar{h}_c = 0.33 \ \frac{k_f}{D}(Re_D)^{0.6}\mathrm{Pr_f}^{0.3} \tag{9}$$

where, D = Pin Diameter.

Film cooling

Film cooling scheme can play a vital role to achieve higher turbine entry temperature. Film cooling helps boundary layer to cool down to a certain limit and increases the cooling effectiveness that results a uniform temperature distribution on the

blade surface. Film cooling effectiveness is calculated by using the following set of equations from Reference [2]. These equations can predict the experimental results quite well for a certain range of ξ [10~100]. But for the rest of the range [0~10] a constant value of $\bar{\eta} = 0.45$ is selected based on experiments.

$$\xi = \left[{}^{(X + 1.909D)}/_{MS} \right] \left(Re_2 \frac{\mu_2}{\mu_\infty} \right)^{-0.25} \qquad (10-a)$$

$$\bar{\eta} = (1 + 0.249\xi)^{-0.8} \qquad (10-b)$$

The film cooling effectiveness is used to compute the film temperature of fluid from the corrected hot gas temperature. Initially, the hot gas temperature is calculated based on the span location. Then, this temperature is modified for the aerodynamic heating that produced by the kinetic energy of a high velocity stream moving over a stationary body.

$$T_f = T_r(1 - \eta) + \eta \overline{T}_{CF} \qquad (11)$$

$$T_r = T_\infty + \frac{Pr^{RE} V_\infty^2}{2C_p} \quad \left[RF = \frac{1}{2} \text{for laminar flow}, RF = \frac{1}{3} \text{for turbulent flow} \right] \qquad (12)$$

Mass Flow Rate Calculation

Flow through a duct or pin-fin passage

To initiate the iterative method, an estimate of the flow rate [from boundary condition] for a particular coolant passage is entered into the system as input and the program is run. The pressure drop due to friction is computed for a smooth duct condition using equation (13).

$$p_1 - p_2 = f \frac{L}{D} \frac{\rho V^2}{2g_c} \qquad (13)$$

In real design, ducts have internal turbulence promoters, repeated ribs, which are deliberated to increase the frictional pressure drop. In order to predict the friction factor on a rib roughened surface, it is required to consider the some key factors such as reattachment, separation and sometimes recirculation. Based on these factors, there are quite good amount of correlations are in literature now a days. However, we can consider the following relationships from Han et al [2] where friction factor for ribbed wall can be computed.

$$\mathrm{R}(\mathrm{e}^{+}) = \left(\frac{2}{\mathrm{f}}\right)^{1/2} + 2.5\ln\left(\frac{2\mathrm{e}}{\mathrm{D}}\,\frac{2\mathrm{W}}{\mathrm{W}+\mathrm{H}}\right) + 2.5 \tag{14}$$

where $\mathrm{R}(\mathrm{e}^{+})$ is the dimensionless velocity at the tip of the ribs, f is the friction factor, e is the rib height D is the hydraulic diameter, W is the flow channel width, and H is the channel height.

And for heat transfer coefficient we have.

$$\mathrm{G}(\mathrm{e}^{+}, \mathrm{Pr}) = \mathrm{R}(\mathrm{e}^{+}) + \frac{(\mathrm{f}/2\mathrm{St}_{\mathrm{r}})-1}{(\mathrm{f}/2)^{1/2}} \tag{15}$$

where $\mathrm{G}(\mathrm{e}^{+}, \mathrm{Pr})$ is the dimensionless temperature at the tip of the ribs, $\mathrm{R}(\mathrm{e}^{+})$ is the dimensionless velocity at the tip of the ribs, f is the friction factor, and St_r is the Stanton Number. Also, we have.

$$\frac{\mathrm{R}}{(\mathrm{P}/\mathrm{e}/10)^{0.35}(\mathrm{W}/\mathrm{H})^{\mathrm{m}}} = 1.23 - 27.07(\alpha/90^{0}) + 17.86(\alpha/90^{0})^{2} \tag{16}$$

$$\mathrm{G} = 2.24\left(\frac{\mathrm{W}}{\mathrm{H}}\right)^{0.1}\left(\frac{\alpha}{90^{0}}\right)^{\mathrm{m}}\left(\frac{\mathrm{P}/\mathrm{e}}{10}\right)^{\mathrm{n}}(\mathrm{e}^{+})^{0.35} \tag{17}$$

$$G = C(e^{+})^{n} \tag{18}$$

where R is the Roughness function, e is the Rib Height, W is the flow channel width, H is the flow channel height, and α is the rib angle; and, G is the heat transfer roughness function, e^{+} is the Reynolds number, and C is an arbitrary coefficient.

In this report, a correction factor is used to estimate the friction factor (f) in order to obtain a realistic estimation for the rib tabulator condition. Again, friction factor is modified in the turning region by a factor of 4.0 than that of straight region case.

$$\frac{f_{TP}}{f_{smooth}} = 8 \tag{19}$$

$$\frac{f_{Turning\ Region}}{f_{Straight\ Region}} = 4 \tag{20}$$

For pin-fin passage pressure drop is higher and estimated using the following equation.

$$\Delta p = \frac{f' \rho U^{2}\ N}{2} \tag{21}$$

where

$$f' = \left[0.25 + \frac{0.118}{\left(\frac{S_T - D_0}{D_0}\right)^{1.08}}\right]\left(\frac{G_{max}\, D_0}{\mu_b}\right)^{-0.16} \tag{22}$$

Pumping pressure

The change in pressure due to pumping effect is also considered in this model. This pumping effect may serve to either increase or decrease the static pressure based on the direction of the coolant flow.

$$\frac{\gamma}{\gamma-1}\left[1-\left(\frac{P_{S_1}}{P_{S_2}}\right)^{\frac{\gamma-1}{\gamma}}\right]=\left(\frac{N}{T_o}\right)^2\left(\frac{\pi}{30}\right)^2\left[\frac{{r_1}^2-{r_2}^2}{2*144\,R}\right] \tag{23}$$

The mass injection rate into the surrounding hot gas (film cooling) is calculated utilizing the same equation that used for orifice flow calculation

$$\frac{W\sqrt{T_s}}{(C_D A)P_s}=\sqrt{\frac{2g_c}{R}\frac{\gamma}{\gamma-1}}\cdot\frac{\sqrt{\left(\frac{P_{S_i}}{P_{S_o}}\right)^{\frac{\gamma-1}{\gamma}}-1}}{\frac{P_{S_i}}{P_{S_o}}} \tag{24}$$

The internal static pressure is used as the driving force for the injection into the surrounding external boundary layer (film cooling).The program is capable of calculating the injection rate into either the suction side/the pressure side, neither or both based on the design of a blade. Injection is made through regularly spaced holes of equal diameter (film cooling hole). The injected mass flow rate is subtracted from the mass flow rate in the duct and the static pressure is recomputed. The computed pressure-and mass flow rate become the inlet conditions to the adjacent element and the procedure is repeated until the tip is reached. If at any element, in the duct the internal pressure is less than the external pressure, then the program stops and generates the appropriate error message.

If the duct is multi-pass, then the procedure is repeated (with film cooling injection if required) until the correct number of passes has been made with satisfactory convergence is obtained.

Flow through the leading edge portion

Flow through the passage adjacent to the leading edge is handled in the similar manners except the calculation procedure of the mass injection rate. The coolant is

impinged into the leading edge inner wall that is computed using the equation for orifice flow [previously mentioned]. The pressure inside the leading edge duct is not possible to calculate in the same manner. Since there is no available method to determine this pressure, so it is calculated in iterative method. For simplicity, the static pressure inside the leading edge at the first element is considered as the average of external and adjacent duct element pressure and continues. The check criterion is made by estimating the residual of mass that remains in the last element. Generally, the residual should be near zero.

Calculation of Blade Metal Temperature

To calculate the temperature of a single element, it is required to compute the internal and external convective heat transfer coefficients at that specific surface location of the blade. However, these calculations are made based on three situations of heat transfer for a general element.

1. External convection from external gas flow to the suction and pressure sides.
2. Radiation from the hot gas
3. Conduction through the suction and pressure side blade material.
4. Internal convection from the suction and pressure sides to coolant.

For the convenient approach, the radiation effects are assumed to be negligible in the heat balance equation. However, from literature [18], this assumption is justified. Based on previous paragraph, the heat transfer mechanisms are modeled in the following manners. The corresponding relations that are implemented in this model are also shown in the equation forms and depicted in Figure 6.

$$\overline{T}_{CF} = \frac{1}{2}\left(T_{CF2} + T_{CF1}\right) \tag{25}$$

$$\dot{m}C_p(T_{CF2} - T_{CF1}) = \left[\frac{T_f - T_{CF}}{\frac{1}{h_o A_o} + \frac{\delta}{A_o k} + \frac{\delta_{TBC}}{A_o k_{TBC}} + \frac{1}{h_i A_i + \text{Mtanh ml}}}\right]_S + \left[\frac{T_f - T_{CF}}{\frac{1}{h_o A_o} + \frac{\delta}{A_o k} + \frac{\delta_{TBC}}{A_o k_{TBC}} + \frac{1}{h_i A_i + \text{Mtanh ml}}}\right]_P \tag{26}$$

$$\left[\frac{T_f - T_{wos}}{\frac{1}{h_o A_o} + \frac{\delta_{TBC}}{A_o k_{TBC}}}\right]_S = \left[\frac{T_{wos} - T_{wis}}{\frac{\delta}{A_o k}}\right]_S \tag{27}$$

$$\left[\frac{T_f - T_{wos}}{\frac{1}{h_o A_o} + \frac{\delta_{TBC}}{A_o k_{TBC}}}\right]_S = \left[\frac{T_{wis} - T_{CF}}{\frac{1}{h_i A_i + \text{Mtanh ml}}}\right]_S \tag{28}$$

$$\left[\frac{T_f - T_{wos}}{\frac{1}{h_o A_o} + \frac{\delta_{TBC}}{A_o k_{TBC}}}\right]_P = \left[\frac{T_{wos} - T_{wis}}{\frac{\delta}{A_o k}}\right]_P \tag{29}$$

$$\left[\frac{T_f - T_{wos}}{\frac{1}{h_o A_o} + \frac{\delta_{TBC}}{A_o k_{TBC}}}\right]_P = \left[\frac{T_{wis} - T_{CF}}{\frac{1}{h_i A_i + \text{Mtanh ml}}}\right]_P \tag{30}$$

Finally, a flowchart, showing how the algorithm of the code works is shown in Figure 7. It is divided into two major sections, where one of them solves for the midchord to trailing edge section and the other one solves for midchord to leading edge section (SPRBL)

Governing Equations and Grid Generation for CFD

As mentioned before, the temperature distribution results over the blade are obtained using two different heat transfer coefficients distributions. First is from the work of Halila et al [1]; but there are situations where the heat transfer coefficient distribution over the blade is not known; for these cases, a CFD simulation should be run to obtain the heat transfer coefficient values and apply them as a boundary condition to the code. In this section, a summary of the CFD simulation theories used for this research and grid generation procedure are presented. The grid generation for the domain is done using commercial software Gambit and the simulation s performed by Fluent 13. Two different turbulence simulation models i.e. Standard k-epsilon, and SST-Transition are used to process the flow.

Standard k-epsilon model

The standard k- epsilon model is a semi-empirical model based on model transport equations for the turbulence kinetic energy (k) and its dissipation rate (epsilon). The model transport equation for k is derived from the exact equation, while the model transport equation for epsilon is obtained using physical reasoning and bears little resemblance to its mathematically exact counterpart. In the derivation of the k-epsilon model, it is assumed that the flow is fully turbulent, and the effects of molecular viscosity are negligible. The standard k- epsilon model is therefore valid only for fully turbulent flows [19].

The Transport equations for this model are as following.

$$\frac{\partial}{\partial t}(\rho k)+\frac{\partial}{\partial x_i}(\rho k u_i)=\frac{\partial}{\partial x_j}\left[\left(\mu+\frac{\mu_t}{\sigma_k}\right)\frac{\partial k}{\partial x_j}\right]+G_k+G_b-\rho\varepsilon-Y_M+S_k \tag{31}$$

$$\frac{\partial}{\partial t}(\rho \varepsilon)+\frac{\partial}{\partial x_i}(\rho \varepsilon u_i)=\frac{\partial}{\partial x_j}\left[\left(\mu+\frac{\mu_t}{\sigma_\varepsilon}\right)\frac{\partial \varepsilon}{\partial x_j}\right]+C_{1\varepsilon}\frac{\varepsilon}{k}(G_k+C_{3\varepsilon}G_b)-C_{2\varepsilon}\rho\frac{\varepsilon^2}{k}+S_\varepsilon \tag{32}$$

where G_k is the generation of turbulence kinetic energy due to the mean velocity gradients, G_b is the generation of turbulence kinetic energy due to buoyancy, Y_M represents the contribution of the fluctuating dilatation in compressible turbulence to the overall dissipation rate; $C_{1\varepsilon}$, $C_{2\varepsilon}$, $C_{3\varepsilon}$ are constants; and, σ_ε and σ_k are the turbulent Prandtl numbers for k and epsilon, respectively. S_k and S_ε are user-defined source terms [19].

The turbulent viscosity is calculated as

$$\mu_t=\rho C_\mu\frac{k^2}{\varepsilon} \tag{33}$$

where C_μ is a constant. The model constants in Fluent have the following values.

$$C_{1\varepsilon}=1.44,\ C_{2\varepsilon}=1.92,\ C_\mu=0.09,\ \sigma_k=1,\ \sigma_\varepsilon=1.3 \tag{34}$$

These default values have been determined from experiments with air and water for fundamental turbulent shear flows including homogeneous shear flows and decaying isotropic grid turbulence. They have been found to work fairly well for a wide range of wall-bounded and free shear flows [19].

Shear-stress transport (SST) transition model

The shear-stress transport (SST) k-omega turbulence model combines two models to better capture the flow in the regions near the wall. Therefore, SST model has better performance for near-wall regions where there is adverse pressure gradients in the boundary layer in comparison to k-epsilon models. SST utilizes a standard k-epsilon model for calculation of the flow properties in the regions far from the wall; and near the wall, uses the turbulence frequency ω , which is expressed as $\omega = \varepsilon/k$ [s^{-1}], as a second variable instead of epsilon.

The transport equations are as following.

$$\frac{\partial}{\partial t}(\rho k) + \frac{\partial}{\partial x_j}(\rho k u_j) = \frac{\partial}{\partial x_j}\left[\Gamma_k \frac{\partial k}{\partial x_j}\right] + G_k - Y_k + S_k \tag{35}$$

$$\frac{\partial}{\partial t}(\rho \omega) + \frac{\partial}{\partial x_i}(\rho \omega u_i) = \frac{\partial}{\partial x_j}\left[\Gamma_\omega \frac{\partial \omega}{\partial x_j}\right] + G_\omega - Y_\omega + D_\omega + S_\omega \tag{36}$$

Now, the SST Transition model interacts with the SST k-omega turbulence model by modification of the k –equation. This model in Fluent is originated from the work of Menter et al. [20] so that there is no need to know the transition location and it's predicted as part of the simulation.

In order to capture the laminar and transitional boundary layers correctly, the mesh must have a y^+ of approximately one. If the y^+ is too large (that is, > 5), then the transition onset location moves upstream with increasing. It is recommended that you use the bounded second order upwind based discretization for the mean flow, turbulence and transition equations [19].

Grid generation

The CFD simulation for this project was done in both a two dimensional domain and also a three dimensional domains; and different turbulence models were used to obtain for heat transfer coefficient results which required a different specific grid generation for each case.

In the first step, the blade geometry was built in the Solidworks. Two camber lines were used to create the side boundaries. Then, this geometry was exported from Solidworks and later imported into Gambit meshing software. One of the reasons Gambit was chosen for building up the mesh was its flexibility for having the ability of creating a boundary layer mesh around the blade (which is kind of a structured mesh) and combining it with the unstructured tetramesh elements. For better capturing of the data near the blade, a boundary layer (B.L.) mesh was created around the blade. The first layer's thickness of the B.L. mesh is adjusted so that the proper values for Y+ would appear on the blade's surface for both k-epsilon and SST-Transition models. Before meshing the volume of the fluid, all the edges and faces were pre-meshed manually to have a more optimum number of elements in the grid; then, an unstructured mesh was used for the simulation. The resolution of the mesh near the blade's tip is so that there is more number of nodes in that zone. For faster calculations and performance, as we go farther from the blade into the fluid domain, the mesh size becomes larger and larger (Figures 8 and 9).

A total number of 20208 and 36202 nodes were used to create two dimensional k-epsilon and SST-transition mesh domain, respectively. These numbers are obtained

after the simulation was run for different grids for each turbulence model and then the same convergence was observed in the average value of blade's surface average heat transfer coefficient to make sure grid is independent of number of nodes. An interesting observation during the mesh independency process was that, for different grids the difference in flow parameter such as mass flow rates at inlet and outlet were not that much. But concerning the heat transfer coefficients, the difference was really noticeable.

The Boundary Conditions at the sides are periodic boundary conditions and the domain is created periodically, too. For the inlet and outlet boundary conditions the values used in the simulation are shown in Table 2.

Table 2–Boundary conditions at inlet and outlet

Condition	Value
Inlet Total Pressure	21 atm
Inlet Total Temperature	1700 C, 1400 C
Outlet Static Pressure	10 atm
Outlet Total Temperature	1023 C

For turbulence parameters, fifteen percent turbulence intensity at the inlet and eight percent turbulence at the outlet are considered. Fluid is assumed to be an Ideal-Gas. Blade's surface has a constant average temperature of 1273 K. Later in Fluent software, two different turbulence models were used for simulation of the flow, k-epsilon and SST-transition. The SST-transition model was run for the prediction of

transition location. After the problem was converged to an order of 10^{-4}, contours Pressure and Mach number distribution were extracted.

Next, an attempt was made to produce 3D CFD simulation to capture the effect of secondary flow that results from the passage endwall and tip leakage. After the heat transfer coefficients are compared to the results of Halila et al. [1] for the midspan section, the results for the tip and hub regions of the blade could be used back in the code for calculating temperatures.

Therefore, for the 3D simulation, the grid generation was more complex including more details for the blade and cascade geometry. The domain and the generated mesh can be seen in Figures 10 to 14. Also, an outlook of the fluid volume unstructured mesh is shown in Figure 15. One of the disadvantages of using a structured mesh is that it requires a long time to accomplish the meshing process; but, it is known that it minimizes energy dissipation inside the mesh elements and often leads to better agreement with measurements. On the other hand, automatic meshing with an unstructured grid minimizes the meshing time, but the geometrical preparation should be done very properly. The geometry for this study was complex and at some points an acceptable structured mesh could not be created, especially near the trailing edge of the blade where the dimensions of the blade are really small. For the structured mesh case, some unacceptable angles (<5°) were observed in the elements which is negative for convergence and CFD accuracy. Therefore, a structured mesh couldn't be reached in the time frame we had and the work was done with an unstructured grid.

The 3D Mesh for the k-epsilon model is consisted of about 4.5 million nodes. Since, due to the high pressure gradients in the cascade, near wall region is a key issue in this work, in order to get detailed information about this region, distance from boundary to nearest point should be small enough to keep Y+ values in the appropriate range for each related turbulence model.

Some considerations in the creation of the 3D geometry are:

- Hub and Casing have a curved profile (Figure 11).
- 1% of spanwise direction length as the tip clearance, finer mesh for this section (Figures 12 and 13).
- Finer mesh near the hub and tip wall region (Figure 14).
- Boundary layer mesh for the blade considering finer mesh at the stagnation point and near the trailing edge (Figures 13 and 14).
- The main flow domain is meshed by an unstructured grid.

Considering the hub and shroud curvature in the simulation is important because the curvature of these surfaces could result in acceleration or deceleration of the flow in near-wall regions and affect the pressure gradients. These regions with high pressure gradients are the ones where separation is most likely to happen. The geometrical details such as blade profile, cascade dimensions, and blades spacing are extracted from a NASA report by Halila et al [3] for a high pressure first stage gas turbine blade. Domain is periodic which means it could represent all other blades installed on the rotor of the turbine engine. Assumption of periodic boundary conditions reduces the CPU usage time and complexity of the simulation by a huge amount.

Code was run for the same boundary conditions of the 2D mesh and results for different sections from hub to tip are reported in the next chapter. Also, contours of heat transfer coefficient on suction and pressure side are presented based on mean temperature method. At the same time, the resulted heat transfer coefficient distributions were utilized in the existing code. With this purpose in mind, heat transfer coefficient is chosen for three different region such as hub portion (20% span near hub), mid-span portion (60% of span) and tip portion (20% span near tip).

Code was run for the same boundary conditions for both 2D and 3D cases. A summary of these conditions can be found in Table 2 and also are depicted in Figure 16. The chord length of the blade is about 3 centimeters. In addition to that the inlet flow attack angle according to Figure 17 [3] is about 45 degrees for the midspan section. In the initial stage, the simulation was done for both a rotating cascade and also a stationary cascade; but since, it's a convention to report the data in the relative frame, the results of the rotating cascade will be the same as the stationary one. Consequently, the rest of the work was done in a stationary frame giving zero rotational velocity to the cascade.

As shown in Figure 18, the Y+ values for k-epsilon model are controlled to fall majorly between 30 and 300; for those values lower than 30 and more than 11.225, Fluent automatically uses wall functions.

Standard wall functions are based on the work of Launder and Spalding [21], and have been widely used specially for simulation of flows in industrial flows. The formulation of these wall functions is as follows.

$$u^+ = \frac{u_p}{u_\tau} = \frac{1}{\kappa}\ln y^+ + \frac{1}{\kappa}\ln E \tag{37}$$

where u_p is the mean velocity parallel to the wall, u_τ is the shear velocity, $u_\tau = \sqrt{\tau_w/\rho}$, τ_w is the wall shear stress, E = 9.793, κ = 0.4187 is the von Karman constant, and Y^+ is the dimensionless distance from the wall.

$$y^+ = \frac{\rho u_\tau y}{\mu} \tag{38}$$

If the flow is in local equilibrium i.e. the production and dissipation are very close to each other, then:

$$u_\tau = c_\mu^{1/4}\sqrt{k} \tag{39}$$

The logarithmic law for mean velocity is known to be valid for 30 <Y+ < 300. In Fluent, the log-law is employed when Y+>11.225. When the mesh is such that Y+< 11.225 at the wall-adjacent cells, Fluent applies the laminar stress-strain relationship that can be written as [19]:

$$Y^+ = u^+ \tag{40}$$

Values of Y+ are also shown for SST-Transition model in Figure 19 for the 2D mesh. As can be seen all the values are below 1 which is the criteria for SST-Transition model.

The current work is on a high pressure gas turbine blade. High pressure stage of the gas turbines usually has a smaller radius in comparison to the low pressure stages; and fluid flow is really complex, highly turbulent and includes really strong secondary flows. Navier-Stokes is the governing equations of the fluid flow and they are

discretized to be solved computationally. Next Chapter will include the results of the written code and the CFD work done by commercial finite volume software Fluent 13. Theory of the turbulence models was discussed in this chapter. All calculations in CFD part are considered in the steady state conditions. Therefore, it is not aimed to optimize any geometry or any other parameter. This work is only an investigation of the heat transfer and the fluid flow of an already designed gas turbine blade, for the data to be used in the written code and obtain temperature of the blade's surface.

RESULTS AND DISCUSSION

This entire chapter will discuss the results obtained from running the code for two different types of blades, first an E^3 (Energy Efficient Engine) Rortor-1 blade, and then a second blade namely Samsung Rotor-1 blade with a different design of internal and external cooling system. Next, a simulation, in both 2D and 3D, is run in commercial CFD code Fluent 13.0 for the E^3 blade and heat transfer coefficient results are used back in the code as a boundary condition.

Case I: Prediction of Temperature Distribution for Rotor Inlet Temperature of 1400^{o}C

In the first part, the code is run for an E^3–stage1 HPT blade. Two different rotor inlet temperatures (RIT) are tested, 1400^{o}C which is used by Halila et al [1], and then 1700^{o}C which is the working temperature of modern high efficiency gas turbines used in aerospace applications and is close to the requirements for the G-class blade.

In running the code, some of the data is taken as existing reference data from Halila et al [1]. These data include, the velocity, or the Mach number distribution over the blade (Figure 20 provided by Halila et al [1]), external heat transfer coefficient for CASE I (Figure 21 provided by Halila et al [1]), and the hot gas temperature distribution along the spanwise length of the blade (Figure 22 provided by Halila et al [1]).

The code is broken into two parts. The first part does the calculations for the first half of the blade from stagnation point to the midchord of the blade and it's called the "forward loop". Then, some of the data from this part of the code, such as film cooling effectiveness, and air film properties, which inter-related to the midchord to trailing edge

section of the blade, are transferred to the second loop of the code; this loop is called the "backward loop". This process is shown graphically on Figure 4 of chapter 2 and also Figure 7 as a representation of algorithm of the code. The forward loop uses about 1.63% of compressor's mass flow rate (1.63% of W_{25}) as coolant and does the calculations for the first half of the blade including the leading edge (LE) impingement passage and backward loop (1.67% of W25 mass flow rate) accomplishes the calculations for the second half including trailing edge (TE) pin-fin passage.

A total pressure of 21 atmospheric and a total temperature of 1400^{o}C are considered for the rotor blade as an external condition. The static pressure of 26 atmospheric and a temperature of 628^{o}C are used as internal condition for the coolant at the inlet. Since the operating temperatures are really high, for safer operation, the turbine blades in current engines use thermal barrier coatings (TBC). TBC serves as insulation for the turbine blades and allows for higher RITs, thereby enhancing turbine efficiency. The performance of TBC depends on the aforementioned coating techniques and the coating thickness. Thereby, the effect of using TBC material could be important on the temperature distribution of the blade and in this project it is taken into account as an additional resistance term in calculation of the temperatures.

The 2D model of the blade section is divided in total 64 elements where the 8 sections are in chordwise direction and 8 sections are in spanwise direction (Figure 4).

The program runs in the flow direction and writes the data in that format. So, the results are presented in the similar format. Results are shown for two loops separately. The results are plotted for mass flow distribution, Reynolds number distribution, heat

transfer coefficient distributions and temperature distributions. In plotting the distributions, they followed the same convention as described earlier. They are plotted for both pressure side and suction side.

The results of the code for the forward loop, i.e. midchord to the leading edge, for mass flow rate, Reynolds number, external and internal heat transfer coefficients of blade surface, and finally temperature distributions for suction side and pressure side of the blade and for both cases of with TBC material and without TBC material are depicted in Figures 23 to 29.

For the first and second passages, since there are no injection holes to outside, mass flow rate or Reynolds number is constant (see Figure 23 or Figure 24, element number 1-16) and as a result internal heat transfer coefficient is constant, too. The small difference that exists between the values of internal heat transfer coefficients for these two passages can be attributed to the variable cross sectional area. In the third passage (element number 17-24), an injection of the fluid to the leading edge through the impingement holes occurs and heat transfer coefficient drops. In the leading edge section (element number 25-32), flow has a complicated pattern and the amount of mass flow rate first increases from element number 25 to 29 and then starts to decrease from there until we approach the last element (element number 29-32). As observed above, internal heat transfer coefficient follows the trend of the mass flow rate or Reynolds number and there is peak for its value at element number 29. The reason for a very high amount of internal heat transfer coefficient in the leading edge is due to jet impingement on the very small cross sectional area in comparison to the other passages.

Temperature distributions on Suction Side are shown for the without TBC case in Figure 26 and for the with TBC case in Figure 27. It shows that TBC has good influence in reducing the temperature on the blade surface. See nomenclature for various temperature definitions. Here, TWOS (solid red color line) is turbine blade suction side outer wall temperature. This temperature should be around 1000^{o}C for safe operation. The temperature of element number 25-32 is too low which means they are over cooled due to the high amount of injected coolant to the outer side at the stagnation point.

Also, temperature distributions on pressure side are shown for without TBC case in Figure 28 and with TBC case in Figure 29. It also exhibits that TBC has positive influence in reducing the temperature on the blade surface. TWOP (solid red color line) is turbine blade pressure side outer wall temperature. The same observations are made for pressure side, too i.e. temperatures are tried to be kept below 1000^{o}C for safe operation and elements number 25-32 are over cooled.

After, the results for the forward loop is obtained, some of the data which is shared between two loops is transferred from forward loop to the backward loop. The effect of accumulation of the injected coolant on the external surface of the blade is taken into account for effectiveness values:

$$\eta = \eta_1 + \eta_2(1-\eta_1) + \eta_3(1-\eta_2)(1-\eta_1) + \cdots \quad (41)$$

The data for effectiveness is copied into the backward loop and then process is continued.

In the midchord to trailing edge zone, the nearly constant value of the internal heat transfer coefficient in the trailing edge is due to the constant amount of fluid

flowing through this zone. In the first main passage, as flow moves from element number 9 to 16, some flow is lost due to injection to the trailing edge; and this is the main reason for the reduction of internal heat transfer coefficient in this passage (element number 9-16). Then, h remains constant in the second main passage (element number 17-24) because of no mass flow loss and again, and due to injection of mass to pressure side of the blade (through holes for film cooling), internal heat transfer coefficient will drop in the last passage of backward loop (element number 25-32) (Figures 30 to 32).

Temperature Distributions on suction side and pressure side of the blade are shown for the cases of without TBC in s 33 and 35, and with TBC in 34 and 36. Again, TBC material helps to reduce the temperatures due to its added thermal resistance in the temperature equations.

Pitch line temperature distribution

After all the temperatures are calculated, the results are compared to that of NASA report by Halila et al [1] from which the boundary conditions and geometry of blade was taken. The values are plotted for the TBC case and inlet temperature of 1400^{o}C. In few points the values are quite off because of lack of exact information. In most cases, we assumed some reasonable size of film cooling hole, pin fin diameter and impingement holes, as these data are not supplied. This comparison is shown in Figure 37.

Case II: Prediction of Temperature Distribution for Rotor Inlet Temperature of 1700^{o}C with Spanwise Variable Heat Transfer Coefficient Distribution

In the next case for the E³ blade, temperature distribution is estimated for spanwise variable heat transfer coefficient distribution using leading edge & flat plate model where inlet temperature is considered to be 1700^{o} C. The heat transfer distribution for the hub is applied for the first 20% of the span length, and then the pitch line heat transfer coefficient distribution is applied for the next 60% of it. The rest of the span is treated with tip heat transfer distribution. However, the prediction is only made for TBC case since RIT is high enough in this case.

As Stagnation region heat transfer is more critical area of a blade, and then 25% rise in calculated leading edge heat transfer coefficient is considered in order to consider the effect of free stream turbulence (FST), higher Reynolds number, size of the leading edge diameter, variable eddy size in oncoming flow, roughness on the surface, curvature effect etc. Sample heat transfer coefficient distributions at hub, pitch and tip are presented in 38.

Since interpretation of the results is pretty much similar to the previous section, the results of this case are shown in appendix A through Figures 39 to 45. By looking at the Figures and taking an average of temperatures all over the external and internal surface of the blade, it becomes known that the pitch region of the blade is experiencing more thermal loads than tip and hub portions; also, the tip region has a higher overall average temperature. These values are presented in Tables 3 and 4.

Table 3–Blade's external overall surface temperature distribution (TWO), case II

	Pressure Side	Suction Side	Total Surface
Tip	766.4888	948.1175	857.3031
Pitch	786.9975	980.6913	883.8444
Hub	762.51	897.1438	829.8269

Table 4–Blade's internal overall surface temperature distribution (TWI) , case II

	Pressure Side	Suction Side	Total Surface
Tip	746.2213	886.2988	816.26
Pitch	764.2363	910.3825	837.3094
Hub	736.7313	833.2625	784.9969

Case III: Prediction of Temperature Distribution for Rotor Inlet Temperature of 1700^oC with Transition Model

This case will study the effect of transition model on the temperature distribution to predict the transition on a turbine blade. It is very crucial to have some experimental evidence from heat transfer distribution data. However, a transition model is designed using flat plate correlations. For the leading edge of the blade, heat transfer coefficients are estimated using the following correlation:

$$Nu(\theta) = \frac{h_c(\theta)D}{k} = 1.14\left(\frac{\rho U_\infty D}{\mu}\right)^{0.5} Pr^{0.4}\left(1-\left(\frac{\theta}{90}\right)^3\right), \qquad (0^o \le \theta \le 90^o) \qquad (42)$$

Based on critical Reynolds numbers, laminar to turbulent transition is considered in this model and then the data set is matched with the experimental trend. As other factors such as roughness, pressure gradient along the blade surface, unsteady wake and free stream turbulence can change the transition behavior, so the exact information is very important to understand the external flow physics. In addition to that, stagnation region heat transfer coefficient is increased about 25% more than the computed one to consider the unsteady wake free-stream turbulence present in the oncoming flow. The transition model is presented in 46.

The temperature distribution for this case also considered with thermal barrier coating effect, as the rotor inlet temperature is high enough. Results of this case are shown in Appendix A through Figures 47 to 53. The average temperature of the total surface area is higher for the midchord region according to Tables 5 and 6. One obvious reason for this phenomenon is that the reference temperature at the inlet of the rotor had a parabolic shape with a peak very close to the midsection of the midchord region. Therefore, as a consequence of larger combustion material temperatures close to the midsection of the blade in spanwise, greater temperatures are experienced by this region. That's why usually more attention is spent on the design of a gas turbine blade cooling system, especially close to the mid-range by embedding more number of cooling holes with different and more efficient shapes in this specific zone. In the meanwhile, for the endwall section some methods such as endwall contouring is utilized to achieve better cooling of the blade.

Table 5 –Blade's external overall surface temperature distribution (TWO), case III

	Pressure Side	Suction Side	Total Surface
Tip	779.6575	949.25	864.4538
Pitch	791.6138	975.3038	883.4588
Hub	762.51	897.1438	829.8269

Table 6 –Blade's internal overall surface temperature distribution (TWI), case III

	Pressure Side	Suction Side	Total Surface
Tip	746.2213	886.2988	816.26
Pitch	764.2363	910.3825	837.3094
Hub	736.7313	833.2625	784.9969

Case IV: Prediction for Samsung Rotor-2 Blade Model

In this part, prediction of temperature distribution is conducted on Samsung rotor-2 blade at given conditions. Code is modified according to the new blade's geometrical features and number of ducts. These geometrical specifications can be seen in Table 7 and 8. Also Figure 54 shows a cross section of the blades cooling hole arrangement. Other reference data such as spanwise velocity distribution, chordwise velocity distribution, spanwise reference temperature and total temperature, and also the results of forward loop and backward loop are presented in Appendix A, part IV in Figures 55 to 73. The program is modified to calculate heat transfer coefficient by

considering a smooth channel first and then it is enhanced by 2 times for regular passage and 5 times for pin fin passage to compensate for rib tabulator and pin fins accordingly. For the first two ducts, the coolant is ejected. In this case, at the last element of these two ducts the static pressure is averaged. Based on the internal and external pressure difference, the tip injection hole size is calculated by utilizing a residual parameter. This parameter ensures that the total mass can be injected outside through that hole.

Table 7– Specifications of Samsung blade

Span Length	24 cm
Length of suction side	15.89 cm
Length of pressure side	13.93 cm
Number of blades	40
Rotational speed	300 RPM
Total coolant mass flow rate	6.924 kg/s
Mass flow rate per blade	0.1731 kg/s
Coolant's inlet pressure	7.07 bar
Coolant inlet temperature	421.9°C
TBC thickness	0.4mm
Thermal conductivity of TBC	2 W/m.k

Table 8– Duct geometry of Samsung blade

				Suction Side		Pressure Side	
	Areas (mm^2)	Perimeter (mm)	D_h (mm)	Center distance from Stag (S) (mm)	Element Length Chordwise(S) (mm)	Center distance from Stag (P) (mm)	Element Length Chordwise(P) (mm)
Duct 1	222.69	66.41	13.41332	21.76	43.52	14.75	29.5
Duct 2	232.02	106.099	8.747388	57.0085	26.977	42.5135	26.027
Duct 3	253.77	62.278	16.29949	98.1546	55.3152	81.3888	51.7236
Duct 4	42.32	65.83	2.571472	143.269345	34.91429	123.0791	31.657

CFD Results

In previous sections, flat plate correlations were used for estimation of heat transfer coefficient. But, application of experimental data from simplified geometries like a flat plate on a highly curved surface such as an E^3 blade of a real engine, remains questionable. Flow physics on a highly curved airfoil could yield to results which are considerably different from flat plate studies. Therefore, after the temperatures were obtained for cases I, II, III, and IV, a CFD simulation was run, first in 2D modeling only the pitch line of the blade, and then in 3D, modeling also for hub and the tip region including the tip clearance effect. Fluent solves the compressible Reynolds-averaged Navier-Stokes (RANS) equations based on the finite volume discretization method. Many turbulence models are available in these solver. The turbulence models used in the 2D simulation in the first step were k-epsilon, and SST-Transition model; For turbulence parameters, 15% turbulence intensity at the inlet and 8% at the outlet are considered. Fluid is assumed to be an Ideal-Gas. Blade's surface has a constant average temperature of 1000°C.

Contours of the static pressure and Mach number for k-epsilon model can be seen in Figures 74 and 75. Static pressures have their highest values close to the stagnation point of the blade in leading edge. As flow travels to downstream, static pressure decreases to finally reach to the boundary condition value.

The results for the Mach number distribution can be seen in Figure 76. For the pressure side, good agreement is observed between the CFD results and the reference data. On the suction side, CFD results under-predict the Mach number values for most of

this region. Especially the maximum velocity prediction is lower and more toward the trailing edge of the blade in comparison to the reference report. However, for the leading edge section, CFD results fall pretty much on the reference data. The maximum deviation of Mach number in the pressure side from the reference data is about 25%. At around 40% surface distance from the leading edge on suction side of the reference data, Mach number exceeds 1 which is an indicator of supersonic flow; however, results from CFD using the k-epsilon model don't enter a supersonic zone on suction side.

Next, the SST-Transition model was used for the computation of this problem. As seen in Figures 77 and 78, there is a shock near the trailing edge of the blade. This phenomenon was not perfectly captured by the k-epsilon model. The effect of this shock can also be seen in Figure 79 where Mach number plots of the SST-Transition model and NASA report are compared together.

For both SST-Transition and k-epsilon models, Mach number prediction on pressure side shows good agreement with the NASA report; while for the suction side there is some deviation. In contrast to the k-epsilon results, CFD simulation using SST-Transition model predicts a supersonic flow over the suction side of the blade.

Calculation of the heat transfer coefficient is based on two different methods. One is based on the mean fluid temperature of the whole domain:

$$h = \frac{q''}{T_{mean} - T_{wall}} \tag{43}$$

The other approach is based on the adiabatic wall temperature:

$$h = \frac{q''}{T_{adiabatic} - T_{wall}} \tag{44}$$

in which, T_{wall} is equal to 1000°C.

Results for the heat transfer coefficient from different models are presented in Figure 80. SST-Transition model has low estimation of the heat transfer coefficient in comparison to the k-epsilon model. Increase of the heat transfer coefficient in the suction side of the blade for the k-epsilon model can be attributed to the acceleration of the flow. For all models, the highest heat transfer coefficient occurs at the stagnation of the blade. Then, on pressure side, heat transfer coefficient values drops rapidly to about half the value at 14% surface distance for all the models, and then starts to increase gradually over the entire pressure surface to the trailing edge. On the suction side, heat transfer coefficients fall rapidly from the leading edge, then there is an increase in the values which could be related to the acceleration of the flow. For SST model, after the flow acceleration peak there is a second raise in heat transfer coefficient value. A possible explanation for this increase is the happening of transition. This could be further proved by looking at the intermittency contours on the suction side of the blade in Figure 81. Close to the transition region, intermittency values jump from 0 to 1, and this spot is located where the second peak in the heat transfer coefficient of the suction side of the blade is observed. Once transition is completed, heat transfer coefficient values start to decrease gradually toward the trailing edge. Therefore, from the data on suction side and pressure side, it is evident that pressure side boundary layer is fully turbulent from the leading edge, while the suction side boundary layer undergoes a transition from laminar to turbulent. Among different models, k-epsilon model gives a closer estimation of heat

transfer coefficient to the reference values in comparison to SST-Transition, for both methods of the mean temperature and adiabatic wall temperature;

Code was run for the same boundary conditions of the 2D mesh for the 3D case; for the 3D case, parallel computing is employed to reduce time-consumption. Results for different sections from hub to tip are reported in Figures 82 to 85. Blade surface was assumed to have a no-slip boundary condition and uniform wall temperature in all the simulations. Contours of heat transfer coefficient on suction and pressure side are presented in the Figures 86 and 87 based on mean temperature method.

Static Pressure curves around the 3D blade for three locations, 20 percent distance from hub, midspan section, and 20 percent distance from tip region are depicted in Figure 88. From the pressure distributions, it is obvious that the flow on pressure side is much more slower than the suction side, especially up to the first 50-60% percent of the blade surface distance; after that, flow starts to accelerate rapidly on pressure side toward the trailing edge. The pressure distribution on the suction side indicates a highly accelerated flow. The peak velocity according to this graph occurs somewhere in about 70% surface distance from the leading edge for the hub and midspan regions. For the tip region, this spot is surprisingly very close to the leading edge of the blade. The static pressure difference between the pressure side and the suction side is the main driving force for the leakage flow observed in the next figures. As can be seen, the first minimum in the graph shifts down as we go from hub to tip; this can be attributed to the leakage flow through the tip gap.

Heat transfer coefficient distributions versus non-dimensional length for the same three locations are presented in Figure 89. On the suction side, heat transfer coefficient is lowest near tip region. About 20% away from the leading edge for all three regions, there is a sudden increase in the values; this increase is due to the acceleration and/or boundary layer transition of the flow. The same acceleration effect is observed in the pressure side. Heat transfer coefficient distributions near the hub region are much higher than that near the tip region.

The tip of a gas turbine goes under very large thermal loads which could result in the tip failure and melt-down of this section. These high thermal loads are due to the very large temperatures of hot gases flowing over the gap between the tip and shroud of turbine cascade. Then, since the gap is narrow and there is huge pressure difference between the pressure side and suction side of the blade, flow starts to accelerate and this acceleration leads to a thin boundary layer and very high heat transfer coefficients. Another drawback of hot gas flowing through the gap is the increase in losses, and as a consequence loss of efficiency. There are some ways to increase the efficiency for instance by using the squealer shaped tips instead of the smooth ones. Since, in this study, CFD is not the main concern, the tip is chosen to be smooth just for a general understanding of the current turbine in operation. Contours of Static Pressure are shown in Figure 90. Contours of Heat Transfer Coefficient are presented in Figure 91. The patterns of heat transfer coefficient change on the tip portion are to somewhat predictable due to previous research papers in the field. There is a sharp entrance effect in the leading edge of the blade for heat transfer coefficient values where it reaches a

maximum; this could be attributed to the flow reattachment; then there is a drop in heat transfer downstream of that location. Also, by going toward the pressure side Heat Transfer Coefficient starts to decrease on the tip.

Streamlines are produced by releasing particles from the inlet of the cascade. These streamlines can be seen in figures 92 to 94 and they show very well that flow in the tip region is highly three dimensional. The streamlines on suction are lifted up due to the horseshoe vortex effect. The flow leakage from pressure side to suction side, which is a result of higher pressure on pressure side and lower pressure on suction side, is obviously seen on tip of the blade. The separation vortex, which is generated as the incoming flow separates off the inner edge of the pressure side edge, is present everywhere along the pressure side of the blade tip and becomes quite large as we go toward the trailing edge.

One important fact about the tip section is that the pressure difference across the tip also varies widely along the blade. Thus, it is really hard to model this section of the blade very precisely and fully understand, obtain, and provide all the information a designer needs for designing this part of the blade.

There is so much more that could be discussed regarding the CFD results, such as comparison of heat transfer coefficients on the casing and the endwall itself together and also with blade's surface; but unfortunately lack of time at this moment doesn't allow gather more data analysis here in the thesis.

Case V: Temperature Distribution for Rotor Inlet Temperature of 1700^{o}C from CODE and CFD

After the heat transfer coefficients were obtained for tip, pitch, and hub regions from the 3D simulation, they are implemented back into the code and code is run one more time with these new values. The results can be seen in Figures 95 to 101 in Appendix A.

CONCLUSIONS

The purpose of this project was to develop a code and quick model that can be used to design a cooled blade for high pressure gas turbine (HPT). Initially, this project required identification and selection of a potential rotor blade profile to begin with. Later, based on that reference profile, an analytical model was designed that can handle any kind of turbine blade such as G-class Turbine Rotor Blade Cooling. This model is capable of estimating metal temperature distribution of a blade profile to justify the performance of the cooling system design. Also, later, a CFD simulation was run to show that for the cases where external heat transfer coefficients are not available as reference data, still a CFD simulation for an easier geometry of the blade with combination of the code can help us get the surface temperatures.

This report is generated in few steps. First of all, a comparison is made with a reference E3 blade profile that available in open domain. In this comparison, there are some differences due to lack of appropriate information such as the shape and size of the cooling holes, film cooling pattern design, heat transfer distribution, turbulence intensity in the upstream flow, surface roughness etc. However, the temperature distribution patterns showed the conventional trend within a realistic range that gives the confidence of the capability of this program. Secondly, a new set of temperature distribution was observed for the higher rotor inlet temperature to see how it does affect the blade metal temperature for a variable heat transfer coefficient distribution in spanwise direction (from blade hub to tip). Thirdly, an external boundary layer transition model is assumed

and applied to the existing analytical model to obtain a more realistic set of temperature distribution. Thus, the results show a three dimensional distribution of blade metal temperature for a two dimensional analysis of a blade profile in a three dimensional flow field.

Both 2D and 3D CFD were tested. Both $K - Epsilon$ and $SST - Transition$ models were employed. The 3D CFD predictions with K-Epsilon model for the external heat transfer coefficient distribution as well as the blade metal temperature distribution from hub to tip region for rotor inlet temperature of 1700C are reported in the following section, PART B. The 3D CFD model can be further improved in the future study.

In short, some of the observations and conclusions made during the course of this research could be summarized as key-points below:

- The code was capable of predicting the temperature quickly and easily
- Simple correlations for a flat plate and cylinder could be used to predict the general behavior of heat transfer coefficients on a highly curved surface
- Using a TBC material has a big positive influence in reducing the temperatures
- k-epsilon model gave closer values of heat transfer coefficient to the reference report in comparison to the SST-Transition model
- The supersonic flow could be captured by SST-Transition model, but the k-epsilon model failed to predict Mach numbers higher than 1 on the suction side

- Heat transfer coefficients on the surface of the blade after stagnation point, raises due to two reasons: 1)Acceleration of flow 2)Transition from laminar to turbulent
- Streamlines on the suction side of the blade are lifted upwards. This could be related to the existing horseshoe effects.

Finally, this model is quite flexible to any type of modification that is required for new type of turbine blade cooling design. The results can be produced for any kind of change in available parameters such as coolant mass flow rate, size and shape of film cooling holes, impinging jet and pin fin diameter, rib size and orientation, and duct geometry etc. However, the accuracy of the blade metal temperature prediction is highly dependable on specific internal flow and external flow boundary conditions and inlet profiles, i.e. internal and external surface heat transfer coefficient distribution, external pressure, velocity and gas temperature profile either in chordwise or spanwise direction. Eventually, predicting the external surface heat transfer coefficient distribution accurately including the effects of gas stream unsteady high turbulence and surface roughness on boundary layer transition as well as secondary vortices near the hub and tip regions should probably be an important concern for a designer utilizing this code.

REFERENCES

[1] Halila, E. E., Lenahan, D. T., and Thomas, T. T.,1982, “Energy efficient engine, high pressure turbine test hardware detailed design report,” NASA CR-167955.

[2] Han, J.C., Dutta, S., and Ekkad, S.V., 2013, *Gas Turbine Heat Transfer and Cooling Technology*, Taylor and Francis, Inc, New York.

[3] Sautner, M., Clouser, S., and Han, J.C., 1992, “Determination of surface heat transfer and film cooling effectiveness in unsteady wake flow conditions,” AGARD Conference Proceedings, 527, pp. 6-1-6-12.

[4]Han, J.C., and Rallabandi, A.P., 2010, “Turbine blade film cooling using PSP technique”. Frontiers in Heat and Mass Transfer, 1(1), pp 1-21.

[5] Han, J.C., 1984, “Heat transfer and friction in channels with two opposite rib-roughened walls,” ASME Journal of Heat Transfer, 106, pp. 774-781.

[6] Han, J.C., and Park, J.S., 1988, “Developing heat transfer in rectangular channels with rib turbulators”, International Journal of Heat and Mass Transfer, 32(9), pp. 1619-1630.

[7] Han, J.C., and Zhang, Y.M., 1992, “High performance heat transfer ducts with parallel broken and V-shaped angled ribs,” ASME Journal of Heat and Mass Transfer, 35(2), pp. 513-523.

[8] Chyu, M.K., Hsing, Y.C., and Natarajan, V., 1998b, “Heat transfer contributions of pins and endwall in pin-fin arrays: Effects of thermal boundary condition modeling”, International Gas Turbine & Aeroengine Congress & Exhibition, pp. 98-GT-175.

[9] Wright, L.M., and Han, J.C., 2013, “Heat transfer enhancement for turbine blade internal cooling”, ASME Summer Heat Transfer Conference, pp. V003T23A005.

[10] Ekkad, S.V., and Han, J.C., 1997, "Detailed heat transfer distributions in two-pass square channels with rib turbulators," International Journal of Heat and Mass Transfer, 40 (11), pp. 2525-2537.

[11] Jabbari, M.Y., and Goldstein, R.J., 1978, “Adiabati wall temperature and heat transfer downstream of injection through two rows of holes”, ASME Journal of Enginering for Power,100, pp. 303-307.

[12] Metzger, D. E., Bunker, R. S., and Chyu, M. K., 1989, “Cavity heat transfer on a transverse grooved wall in a narrow channel”, Journal of Heat Transfer, 111, pp. 73-79.

[13] Chyu, M.K., Moon, H.K., and Metzger, D.E., 1989, “Heat transfer in the tip region of grooved turbine blades,” Journal of Turbomachinery, 111, pp. 131-138

[14] Yang, H.T., Chen, H.C., and Han, J.C., 2005, “Flow and heat transfer prediction on turbine rotor with various tip configurations”, AIAA 43rd Aerospace Science Meeting and Exhibit, Reno, Nevada, AIAA 2005-573..

[15] Chen, H.C., Jang, Y.J., and Han, J.C., 2000, “Computation of heat transfer in rotating two-pass square channels by a second-moment closure model”, International Journal of Heat and Mass Transfer, 43, pp. 1603-1616.

[16] Wei, L., Weiyang, Q., Kaifu, X., and Hualing, L., 2009, “Numerical simulation of active control on tip leakage flow in axial turbine”, Chinese Journal of Aeronautics, 22, pp. 129-137.

[17] Chowdhury , N., Zirakzadeh , H., and Han , J.C., 2013, “Development of cooled blade for high pressure turbine report”, Sponsored by Samsung Techwin, Texas A&M University, Mechanical Engineering Department, College Station, Texas.

[18] Han, J.C., Ortman, D.W., and Lee, C.P., 1982, “A computer model for gas turbine blade cooling analysis”, ASME Joint Power Generation Conference, pp. 1-7.

[19] Fluent, 2013, FLUENT 13 User’s Manual, Ansys Inc.

[20] Menter, F. R. , Langtry, R. B., Likki, S. R., Suzen, Y. B., Huang, P. G., and Volker., S., 2004, "A correlation based transition model using local variables part 1 -model formulation", ASME-GT, pp. 2004-53452.

[21] Launder, B. E. and Spalding, D. B., 1984, “The numerical computation of turbulent flows”, Computer Methods in Applied Mechanics and Engineering, 3, pp. 269-289.

APPENDIX A

FIGURES

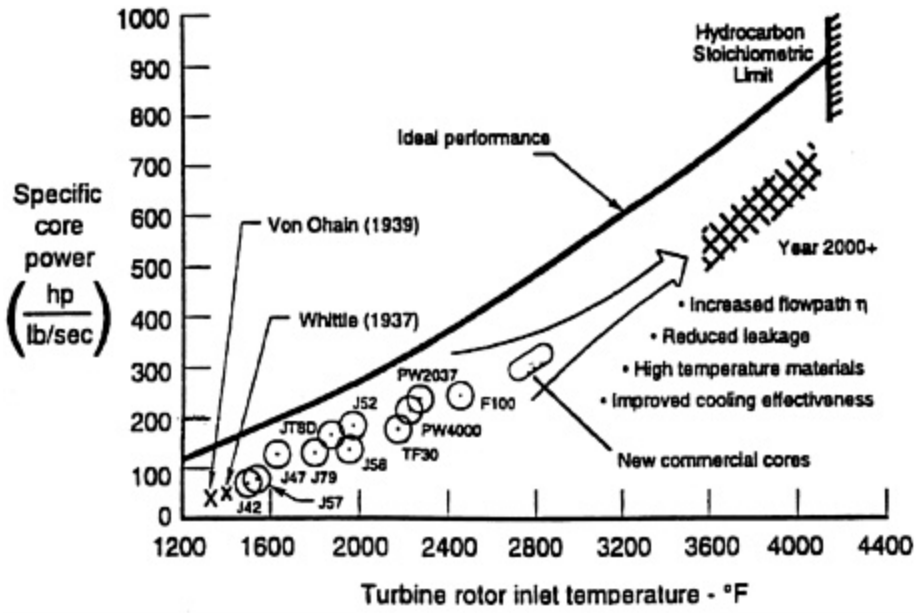

Figure 1 – Gas turbine inlet temperature increase throughout recent decades. Provided from Sautner et al. [3].

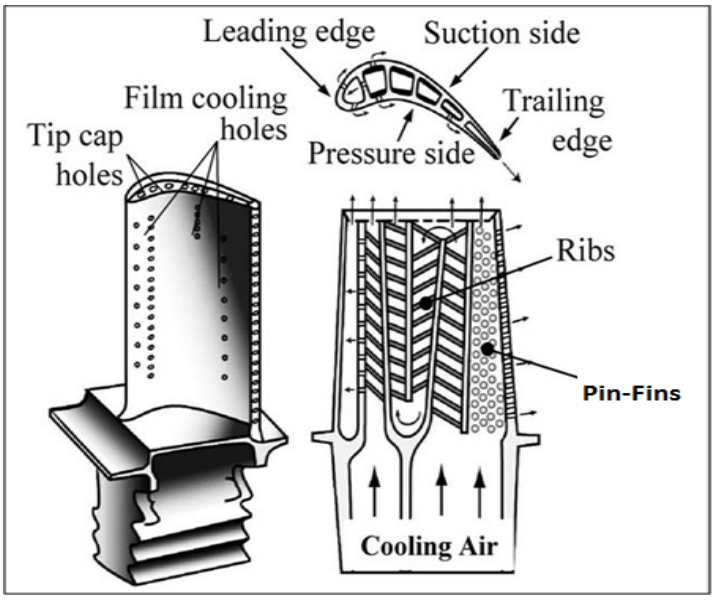

Figure 2 – Different cooling techniques for a typical gas turbine blade. Provided from Han and Rallabandi [4].

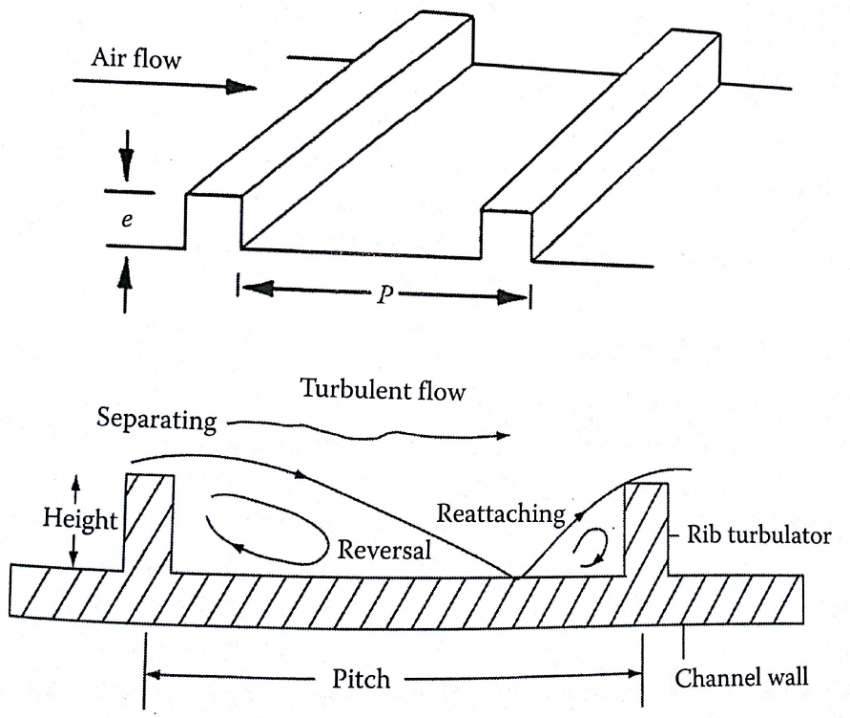

Figure 3 – Side view of a rib-turbulated passage. Provided from Han et al. [2].

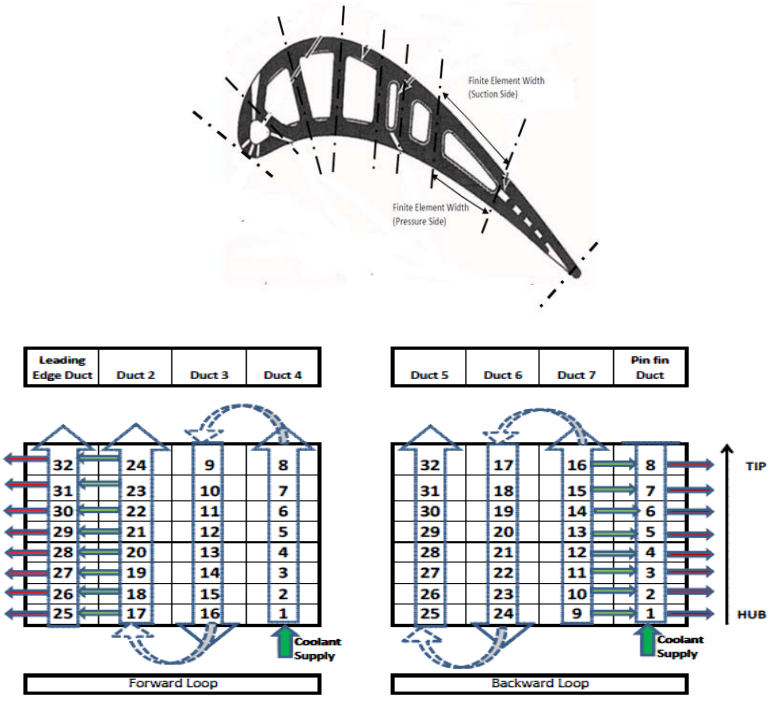

Figure 4– Chordwise and spanwise elements distribution for an E³ blade.

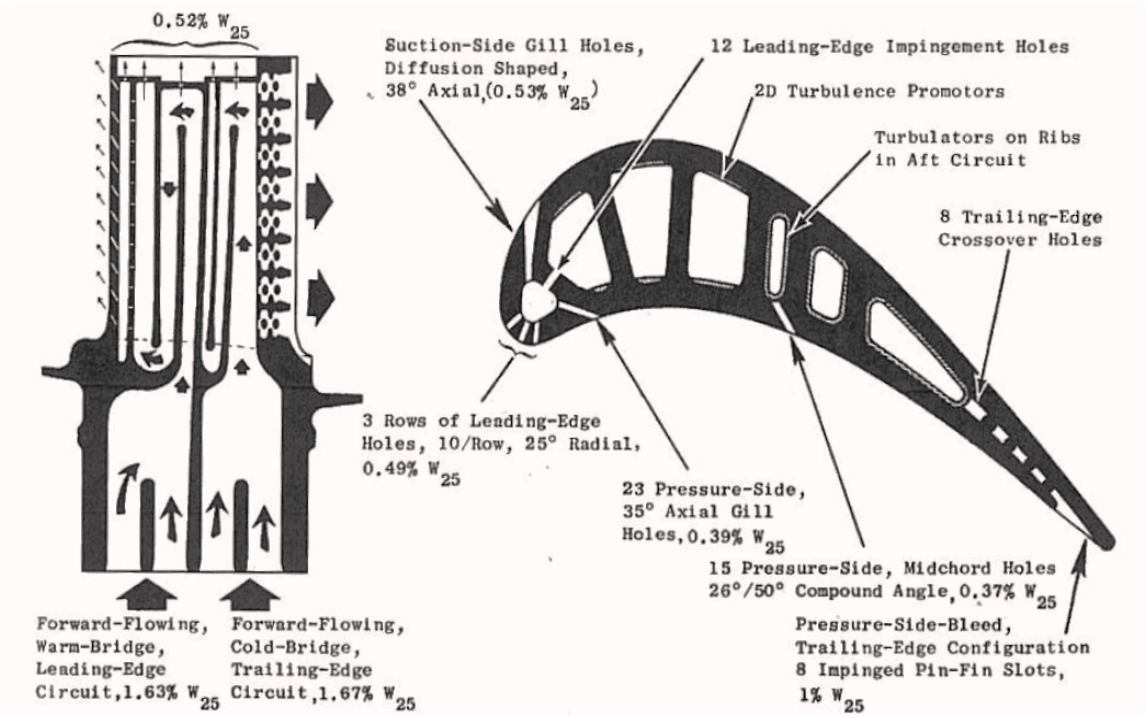

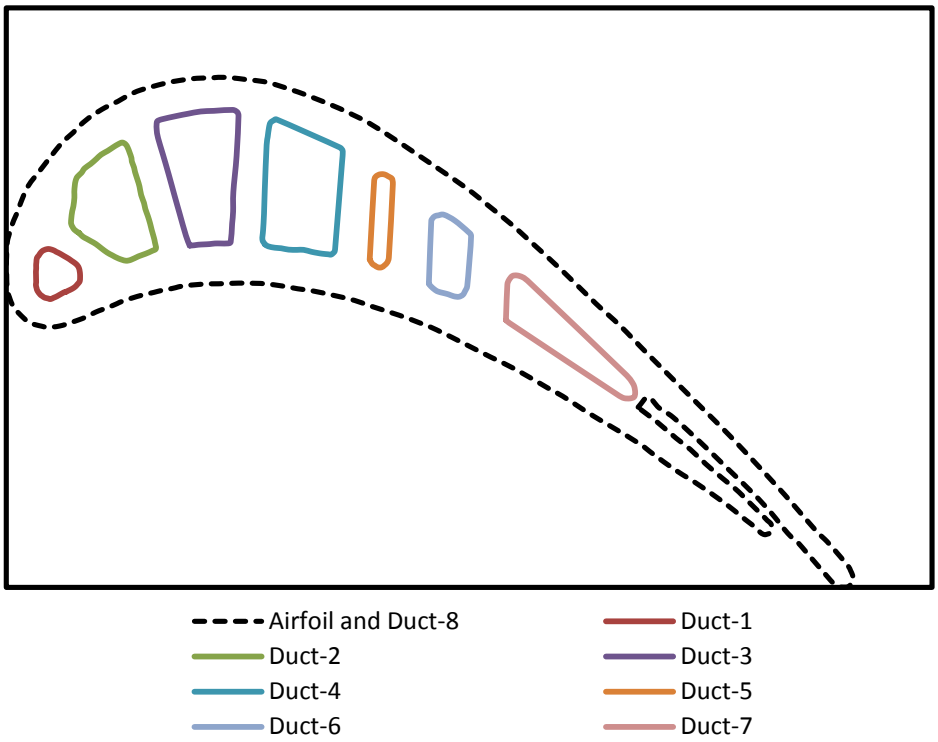

Figure 5– Detailed view of the E³ blade geometry [2].

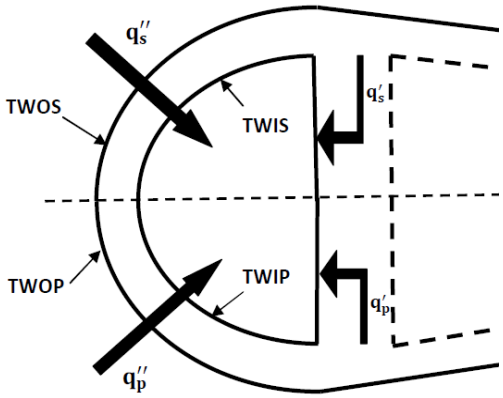

Heat Balance: $Q = q''_s + q''_p + q'_s + q'_s$

$$Q = q_s + q_p$$

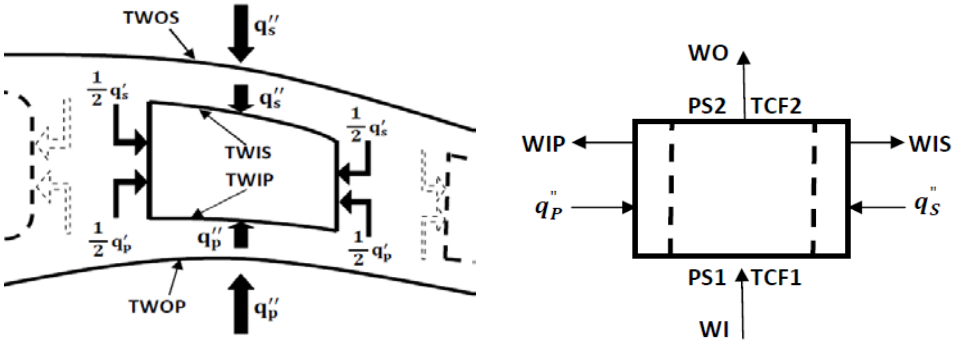

Figure 6- Mechanism of heat transfer and temperature calculations for each element

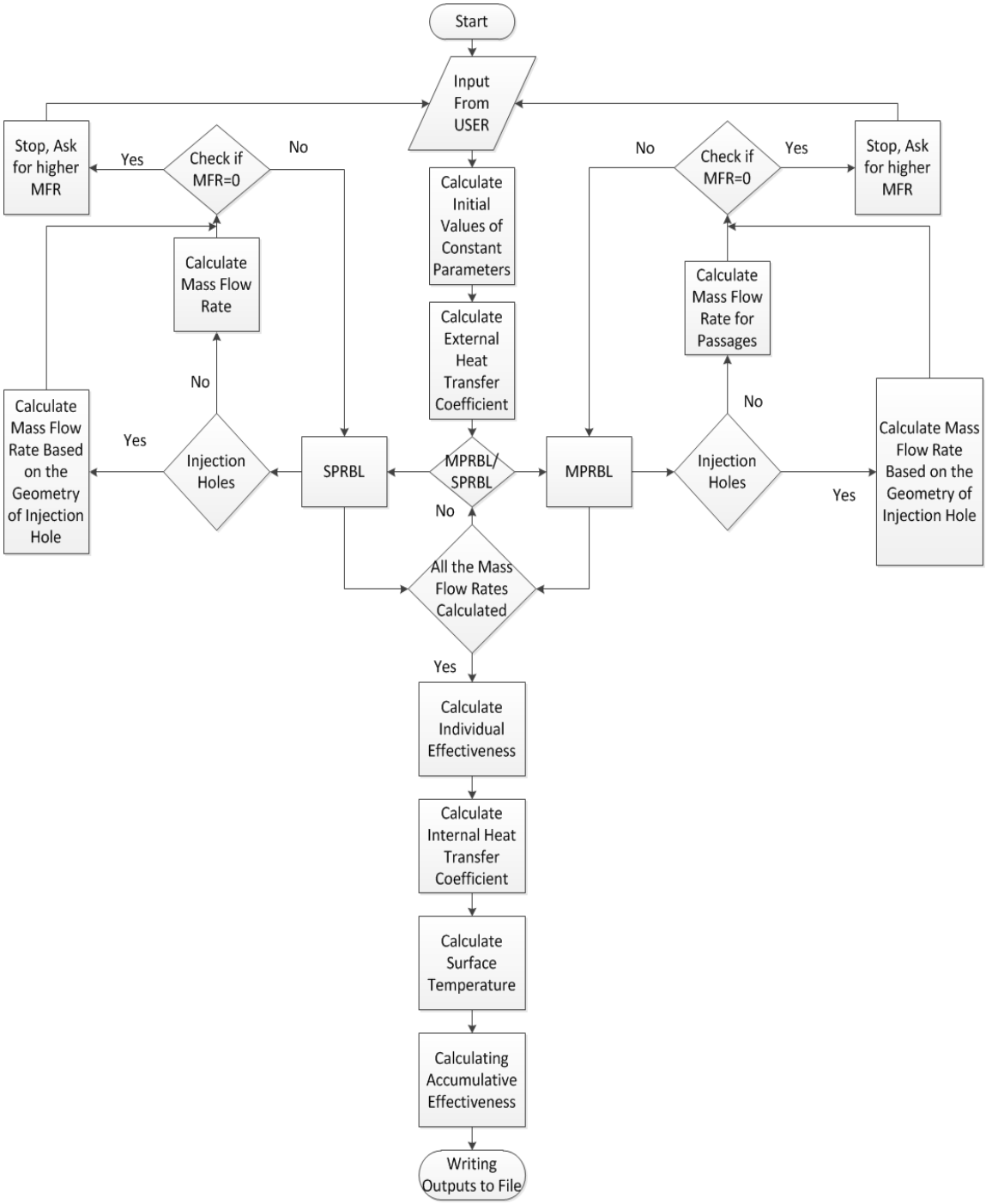

Figure 7- A flowchart of the code functioning

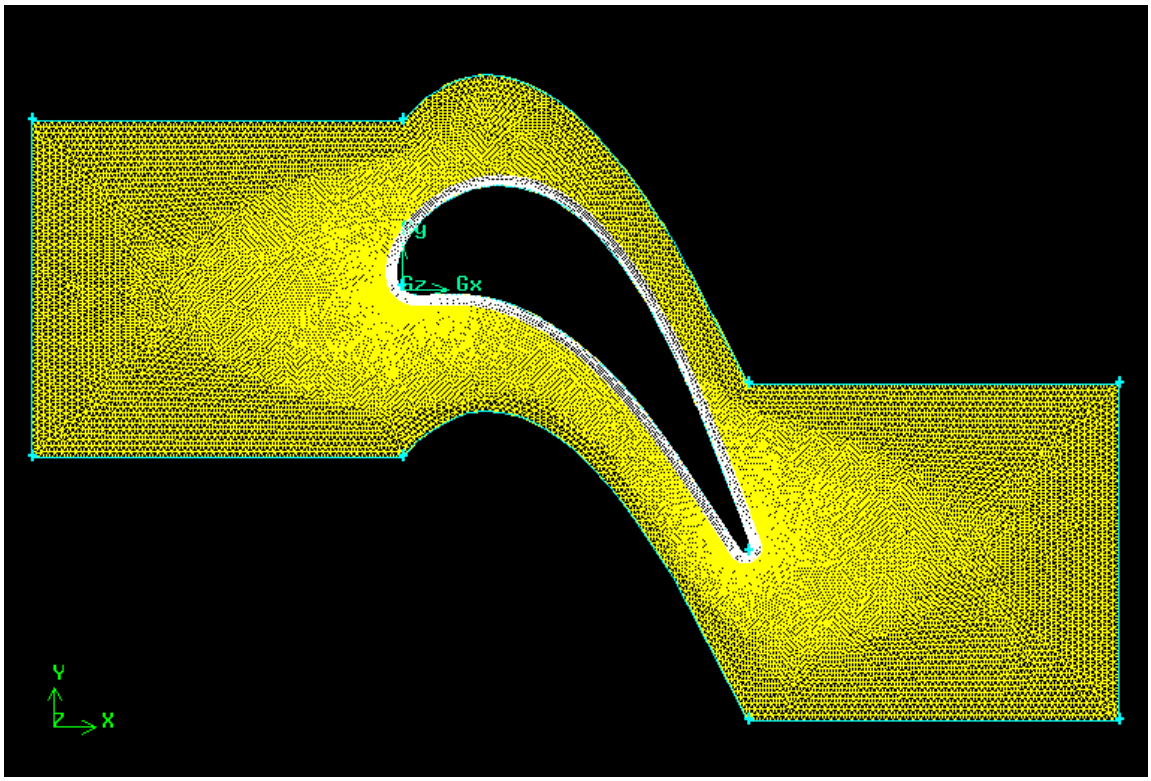

Figure 8– More condense mesh near the blade's surface and Boundary Layer mesh around the blade

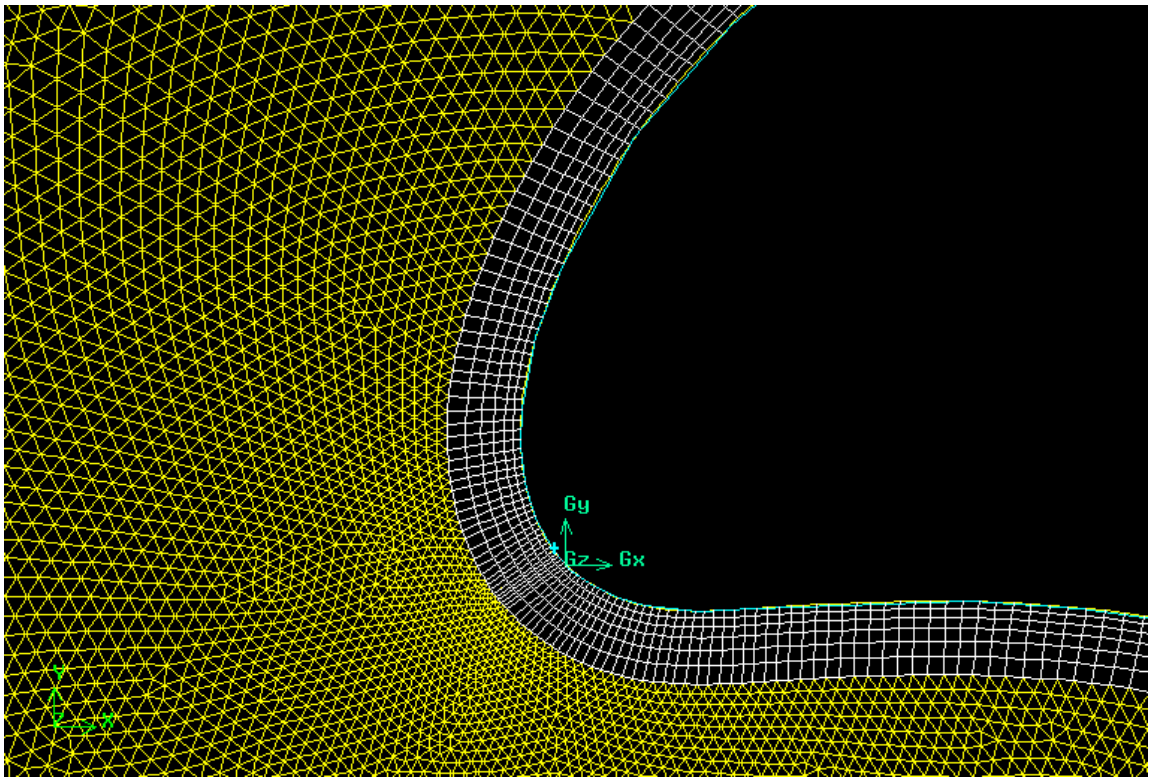

Figure 9– Finer mesh near the leading edge of the blade

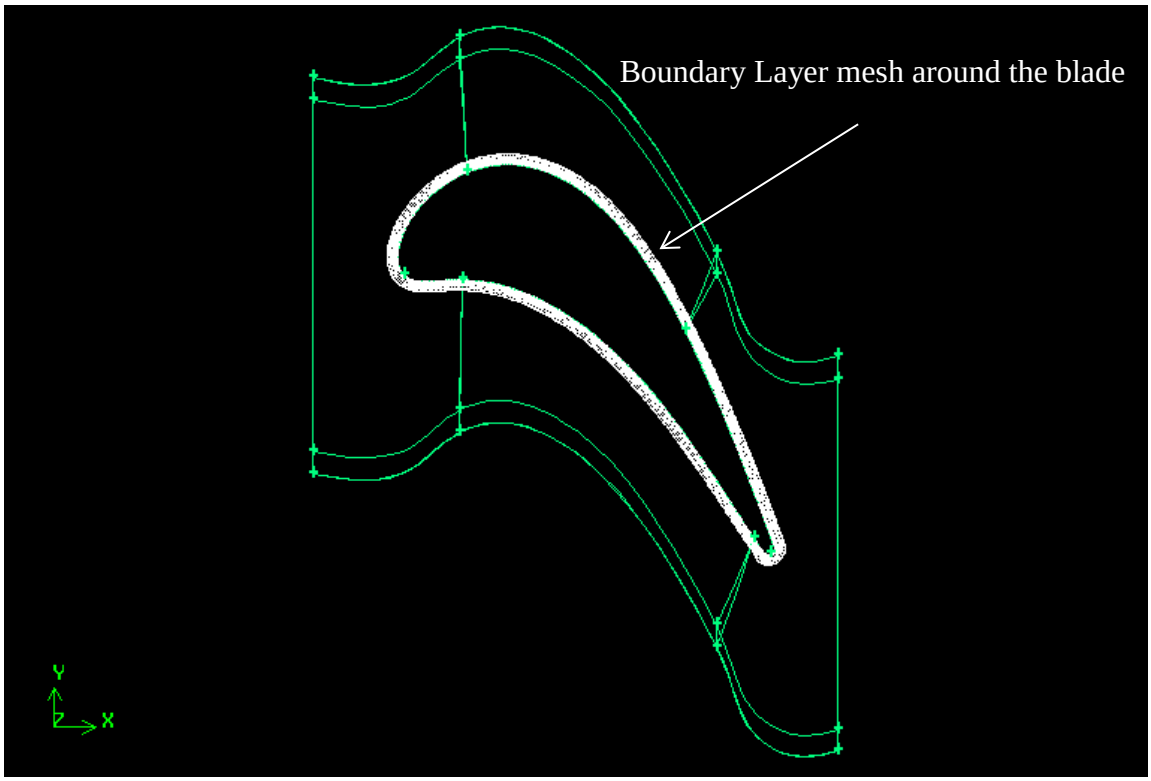

Figure 10– Top view of the 3D domain

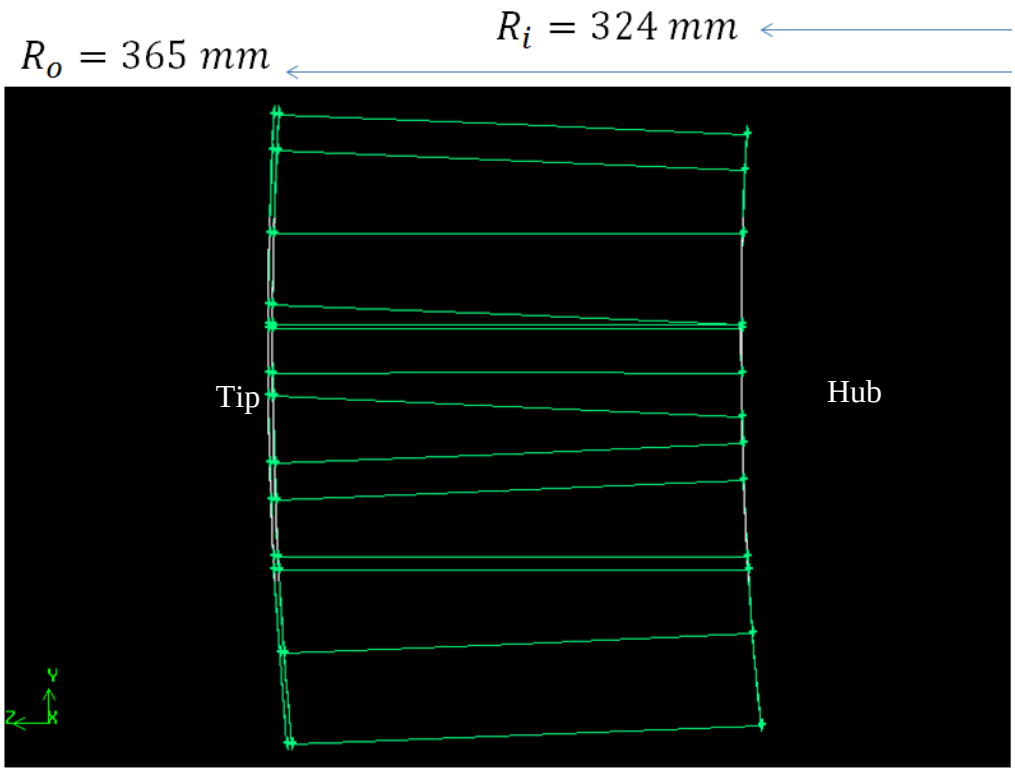

Figure 11– Hub and tip curvature

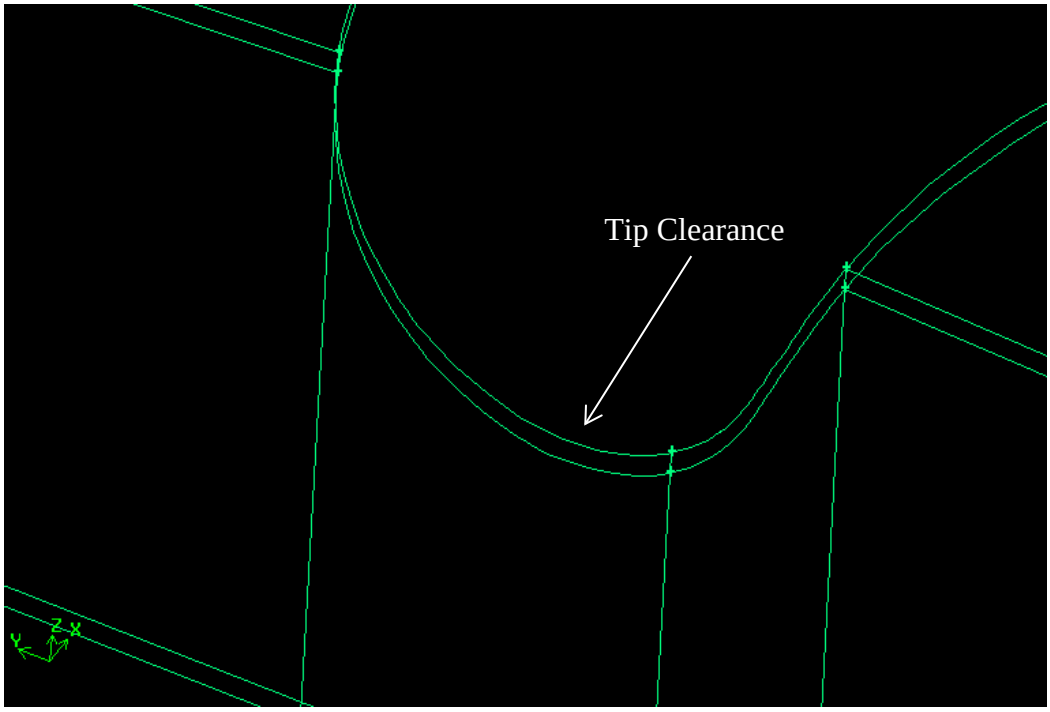

Figure 12– Tip clearance

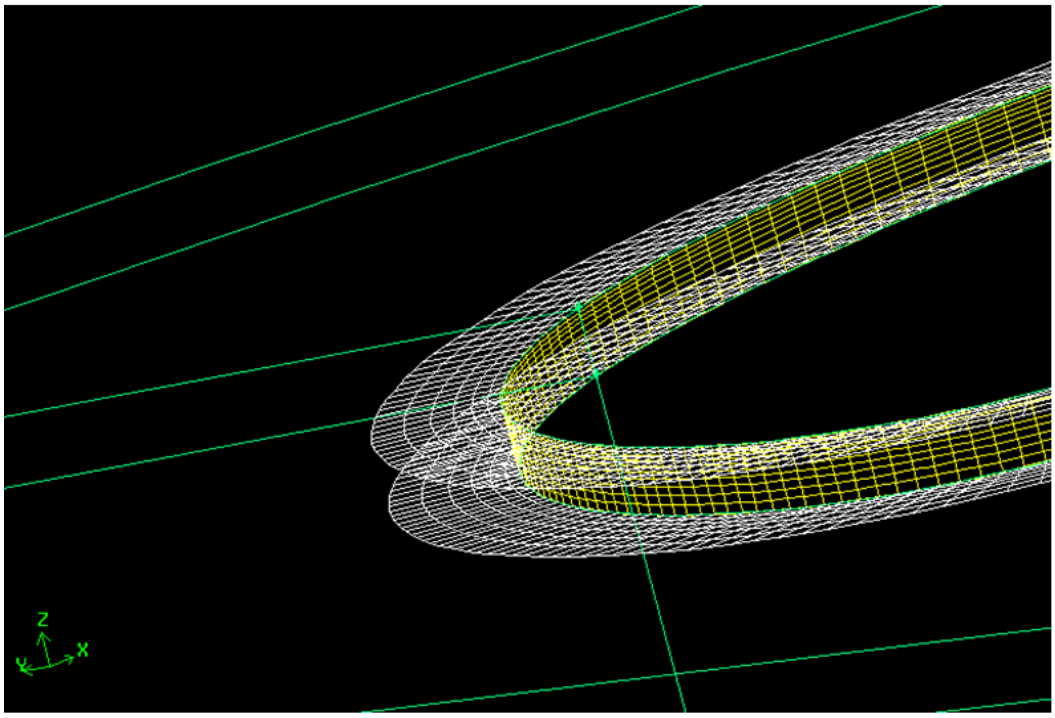

Figure 13– Tip clearance finer mesh

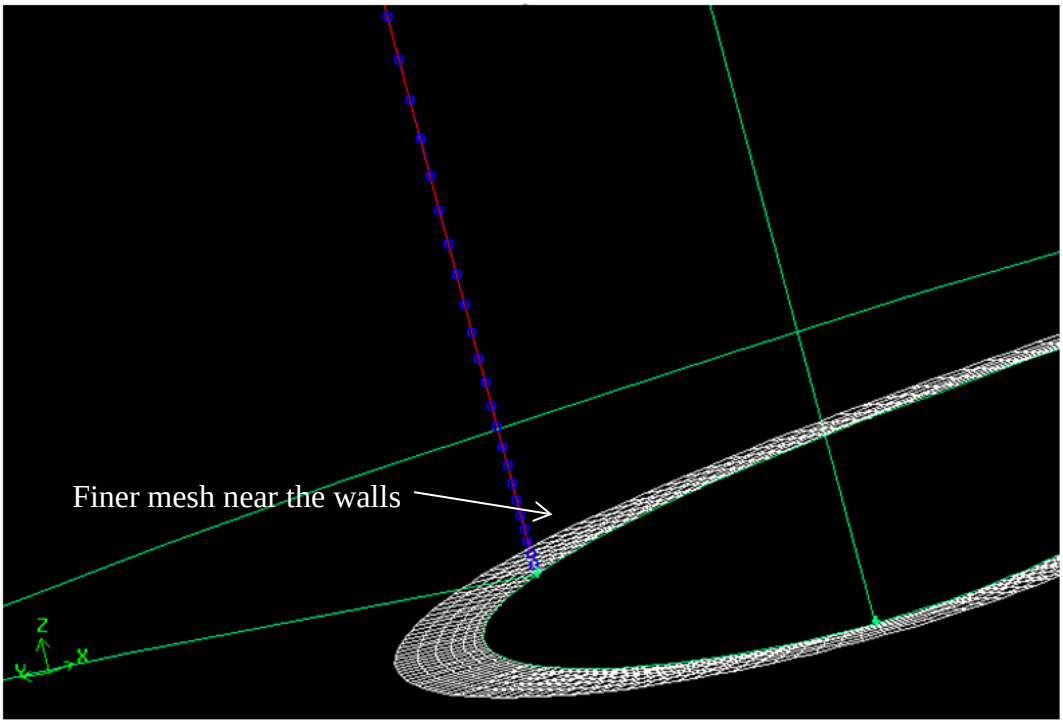

Figure 14– Finer mesh near the hub shown by blue dots

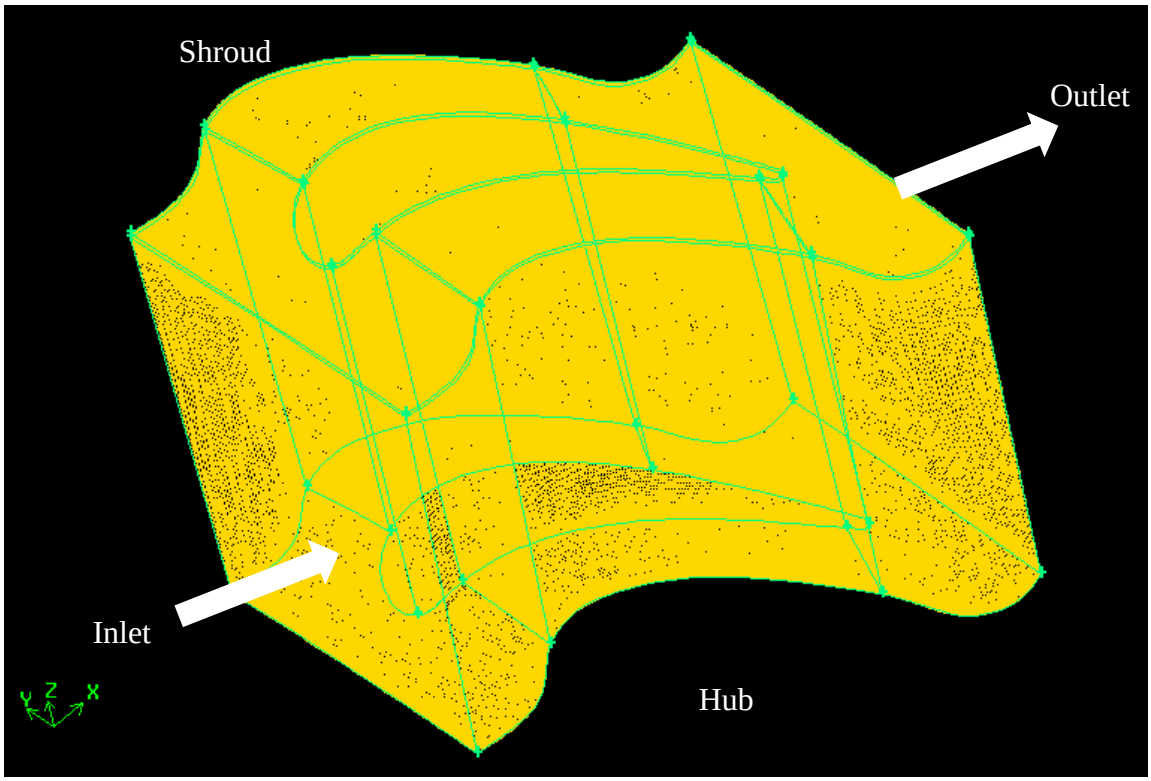

Figure 15– Outlook of the unstructured mesh for the fluid volume in 3D domain

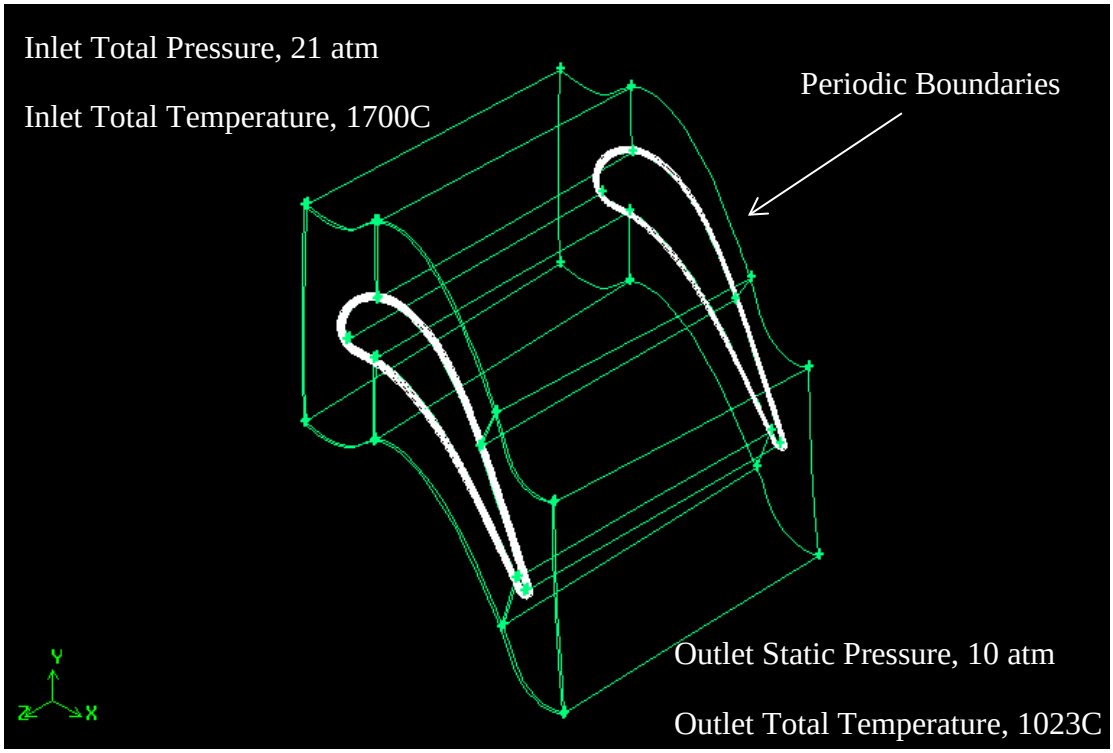

Figure 16 – Summary of boundary conditions

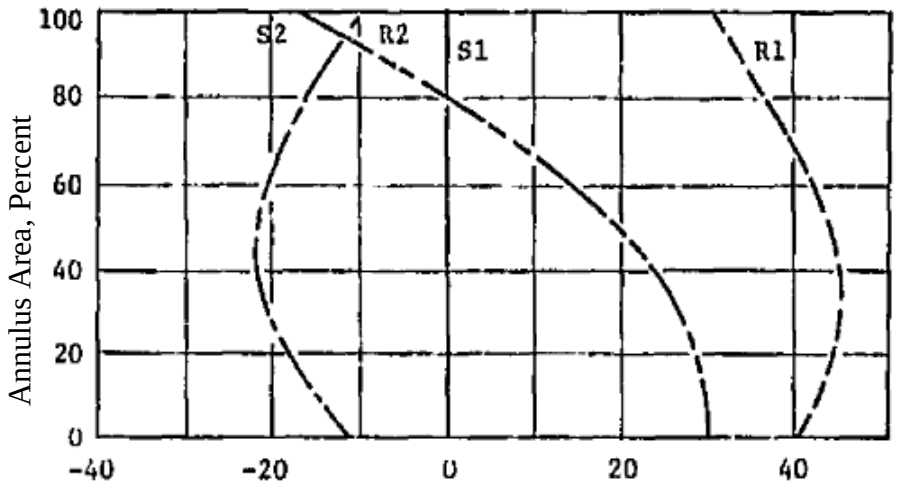

Figure 17– Inlet flow angle for different stages of the energy efficient engine. Provided by Halil et al [3]

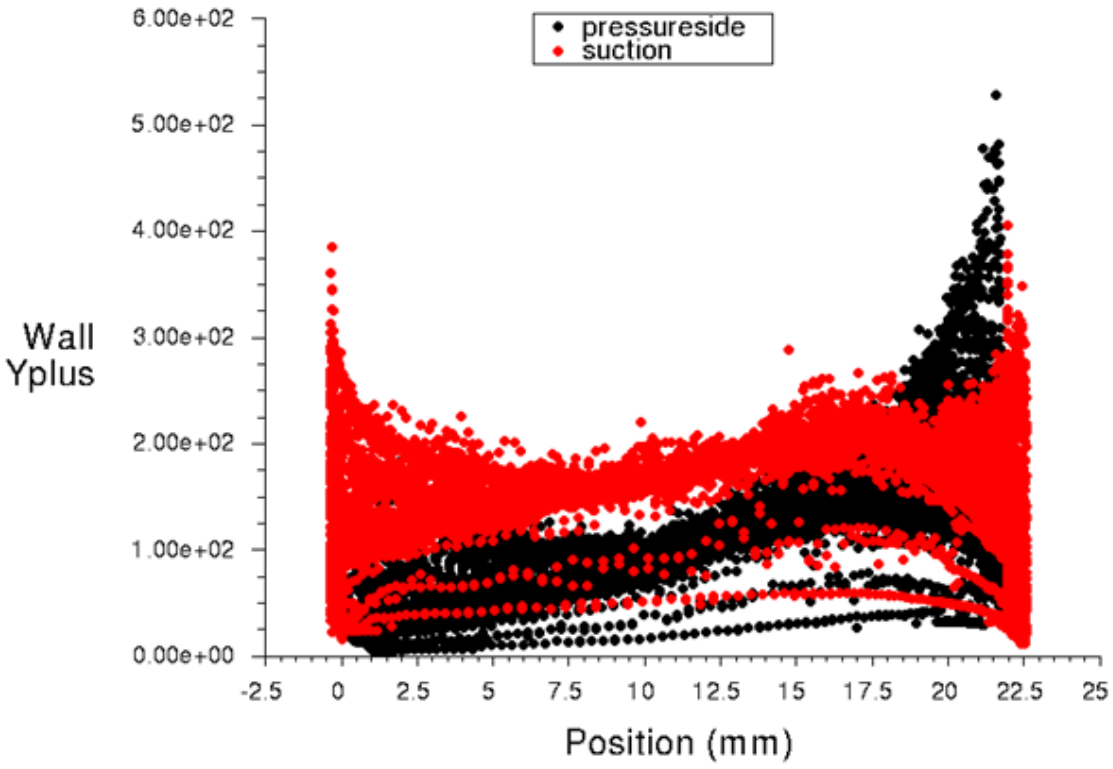

Figure 18 – Y+ values for the 3D mesh and k-epsilon model

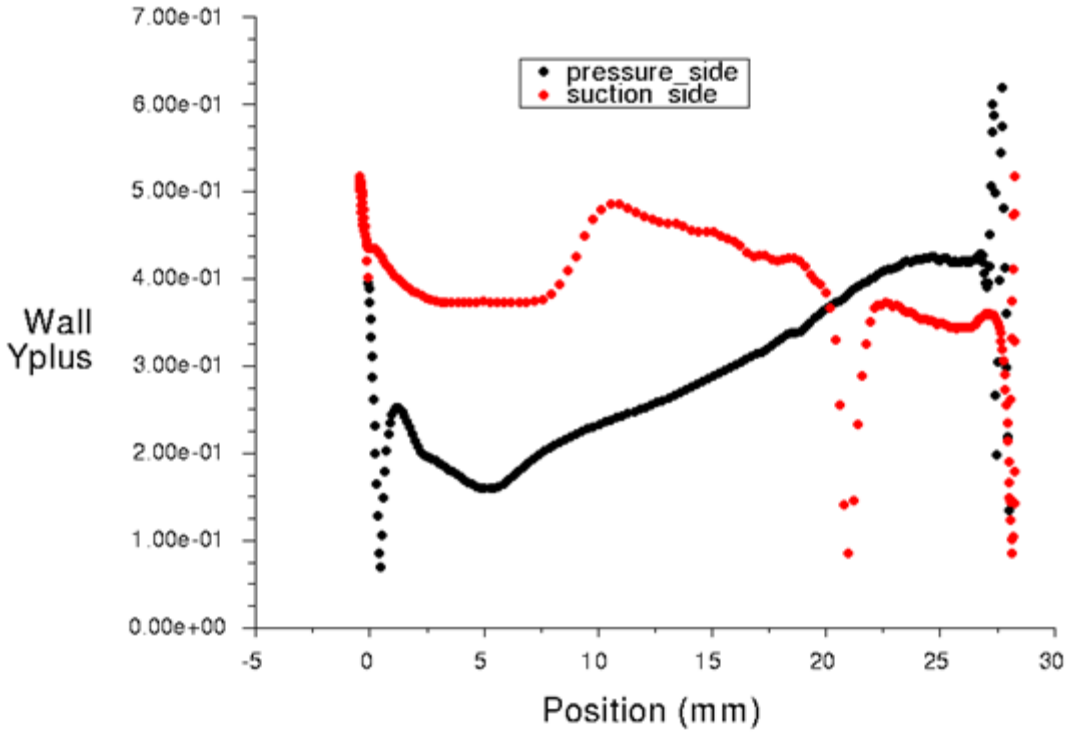

Figure 19 – Y+ values for SST-Transition model controlled to be less than 1 (2D mesh)

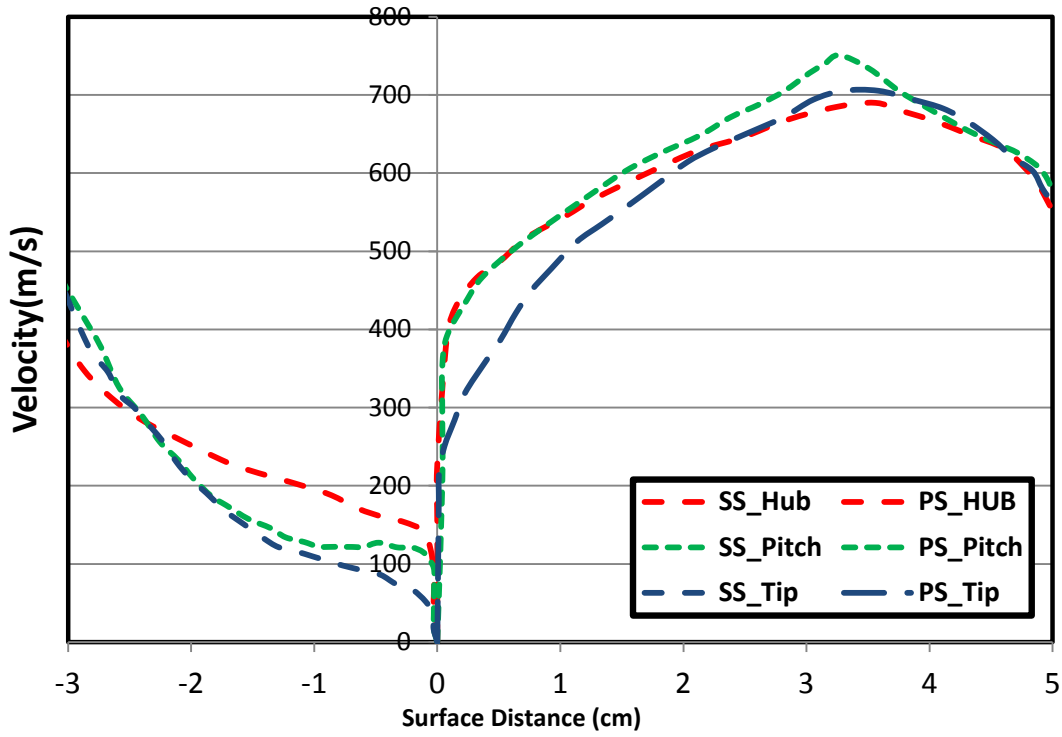

Figure 20– Reference Mach number distribution over the blade, Halila et al [1]

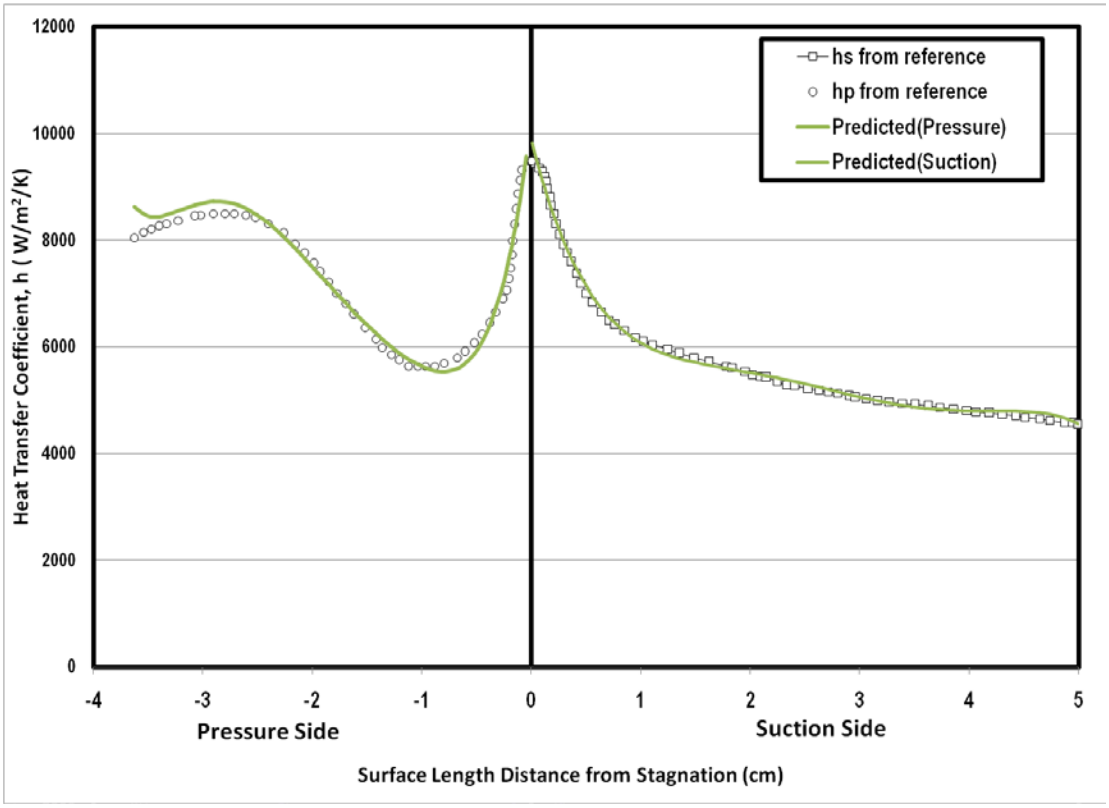

Figure 21– Reference external heat transfer coefficient distribution over the blade, Halila et al [1]

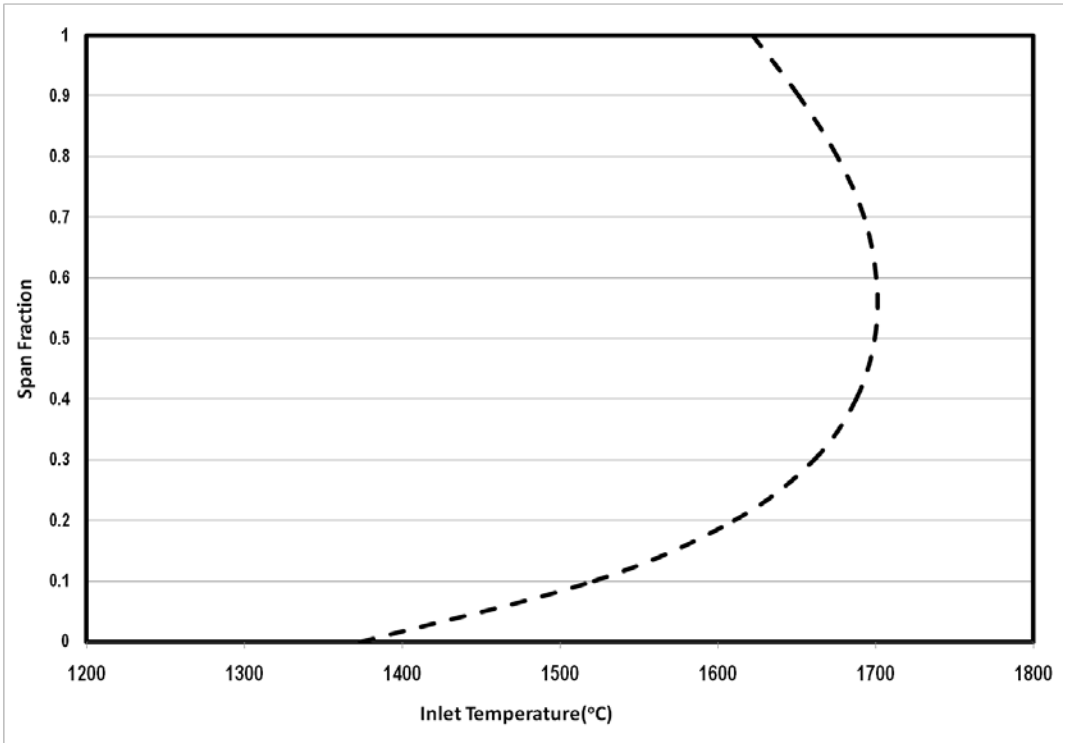

Figure 22– Reference hot gas temperature distribution over the blade, Halila et al [1]

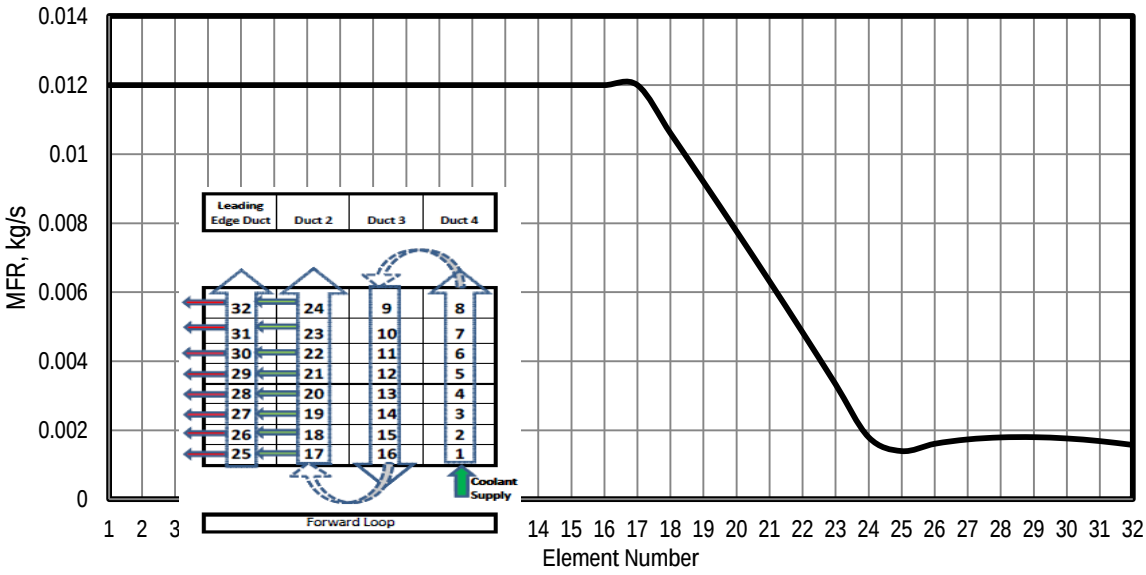

Figure 23– Plot for mass flow rate distribution of the coolant in the forward loop

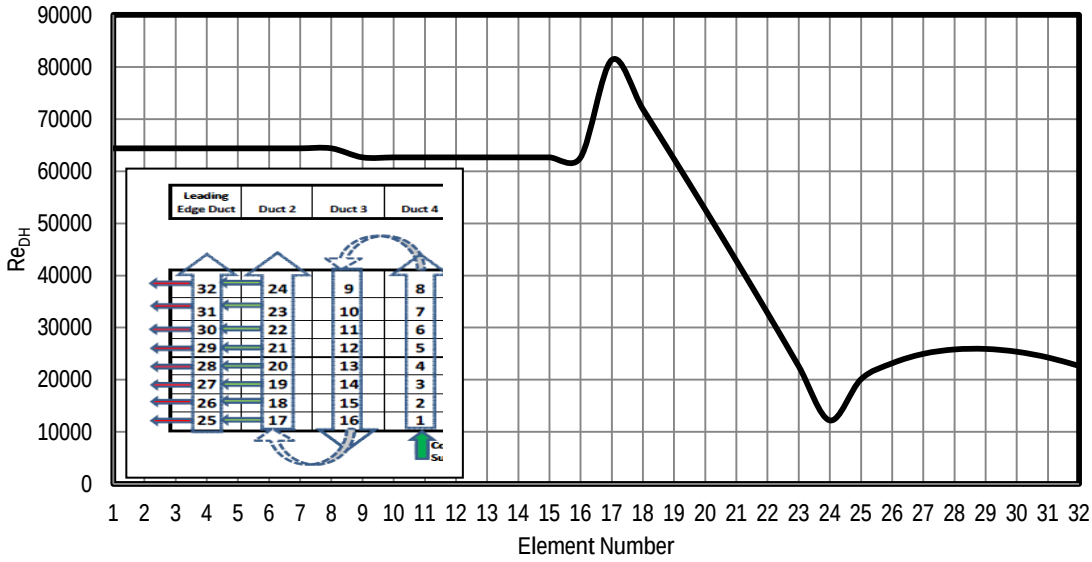

Figure 24– Plot for Reynolds number distribution of the coolant in the forward loop

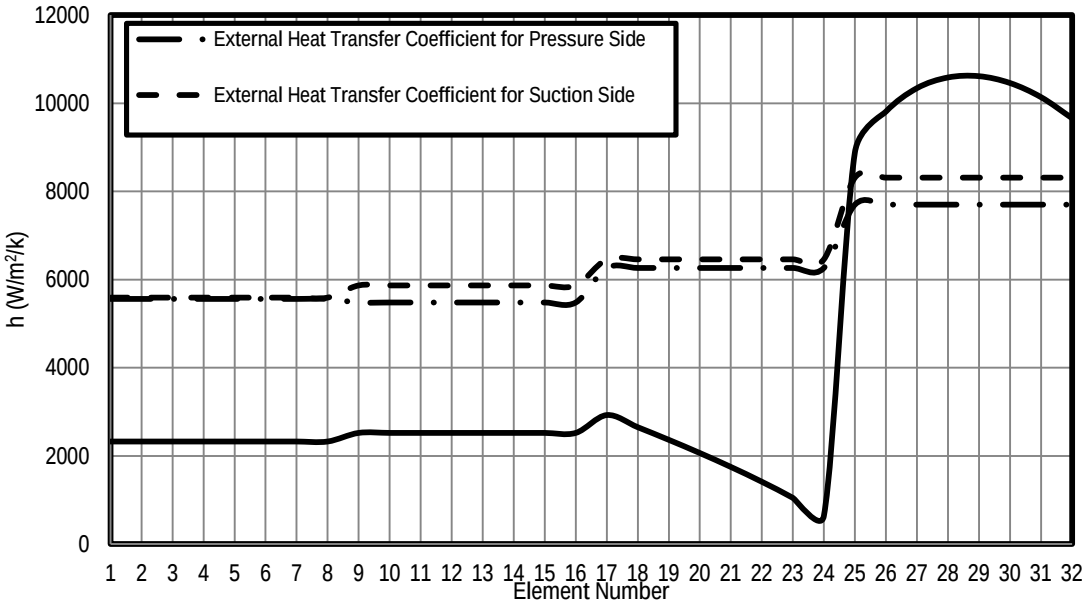

Figure 25–Plot for internal and external heat transfer coefficient distribution

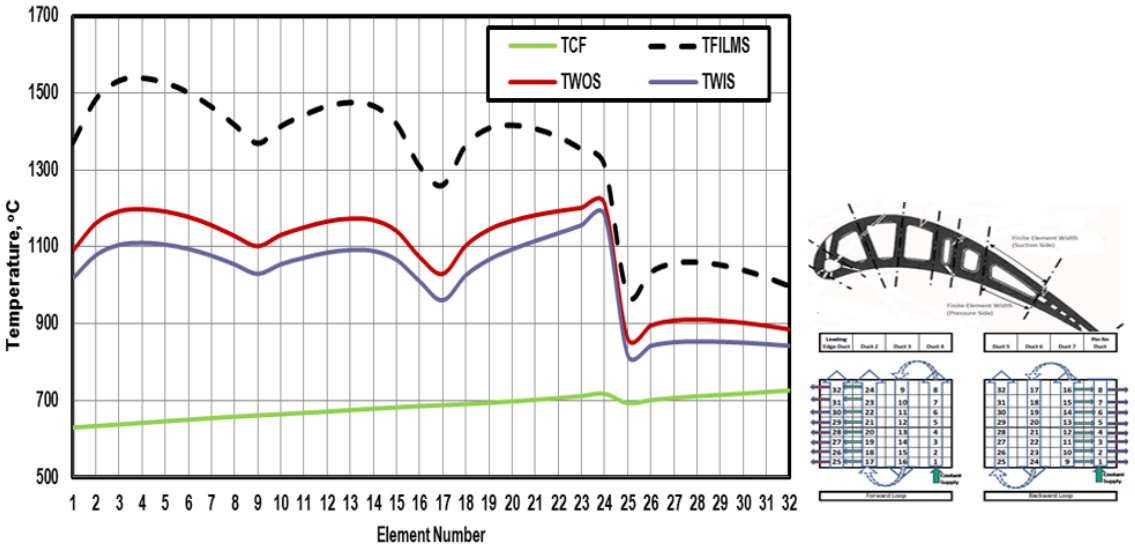

Figure 26– Temperature distribution on suction side pitch line without TBC

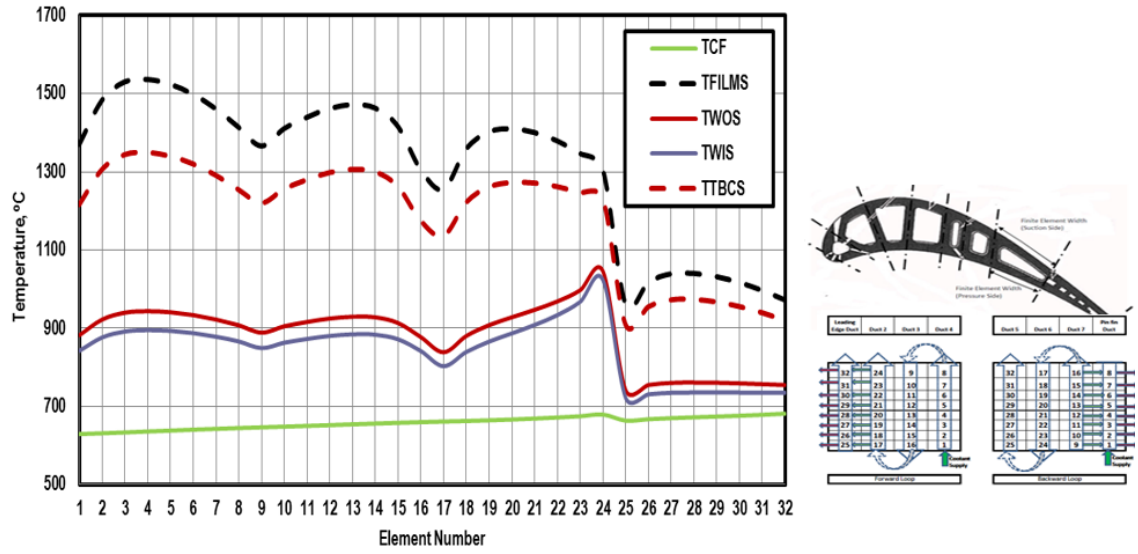

Figure 27– Temperature distribution on suction side pitch line with TBC

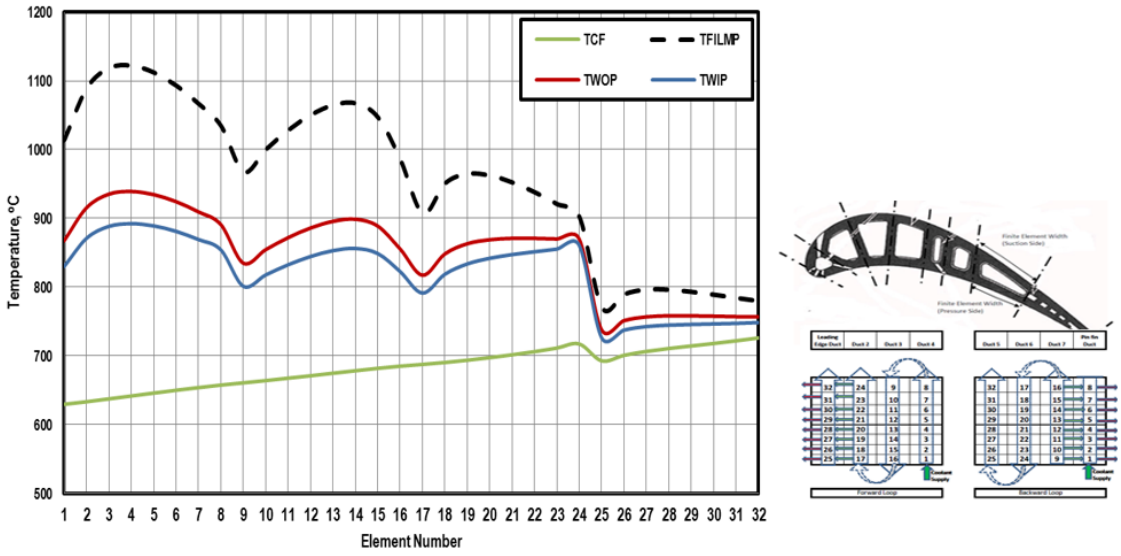

Figure 28– Temperature distribution on pressure side pitch line without TBC

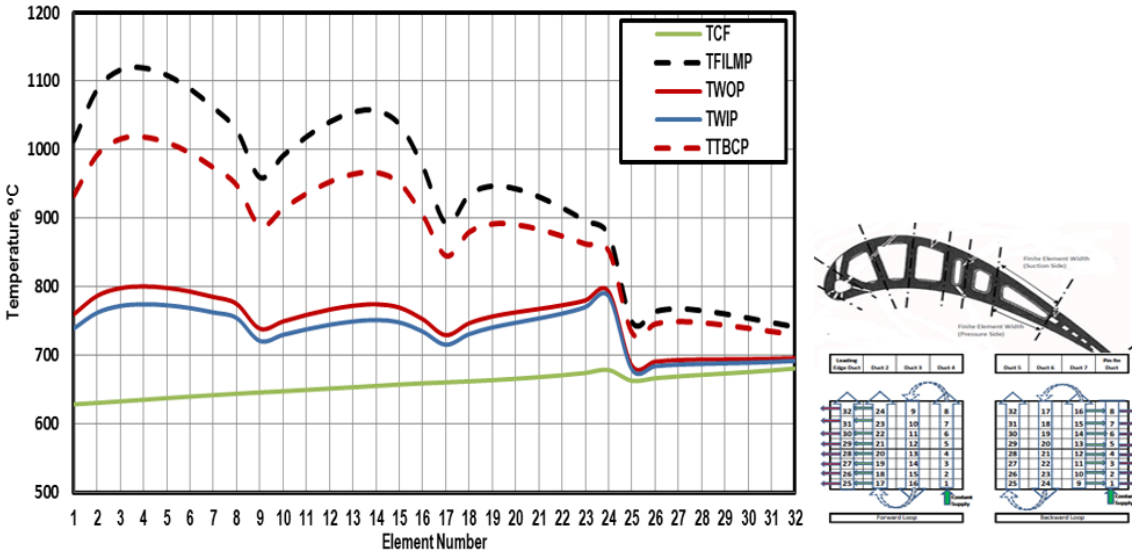

Figure 29– Temperature distribution on pressure side pitch line with TBC

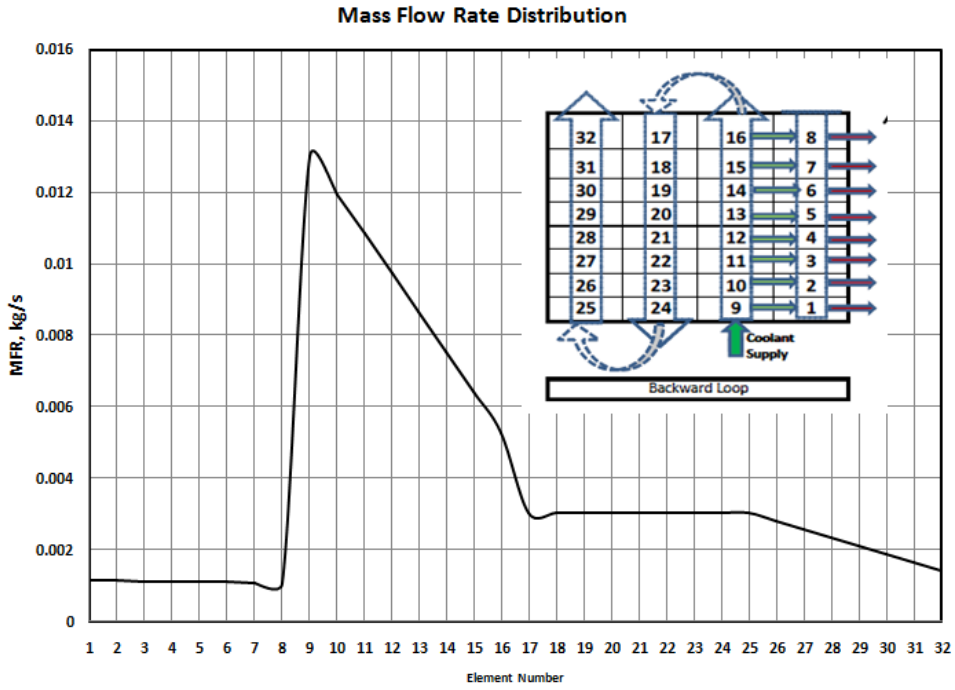

Figure 30– Plot for mass flow rate (MFR) distribution for the backward loop

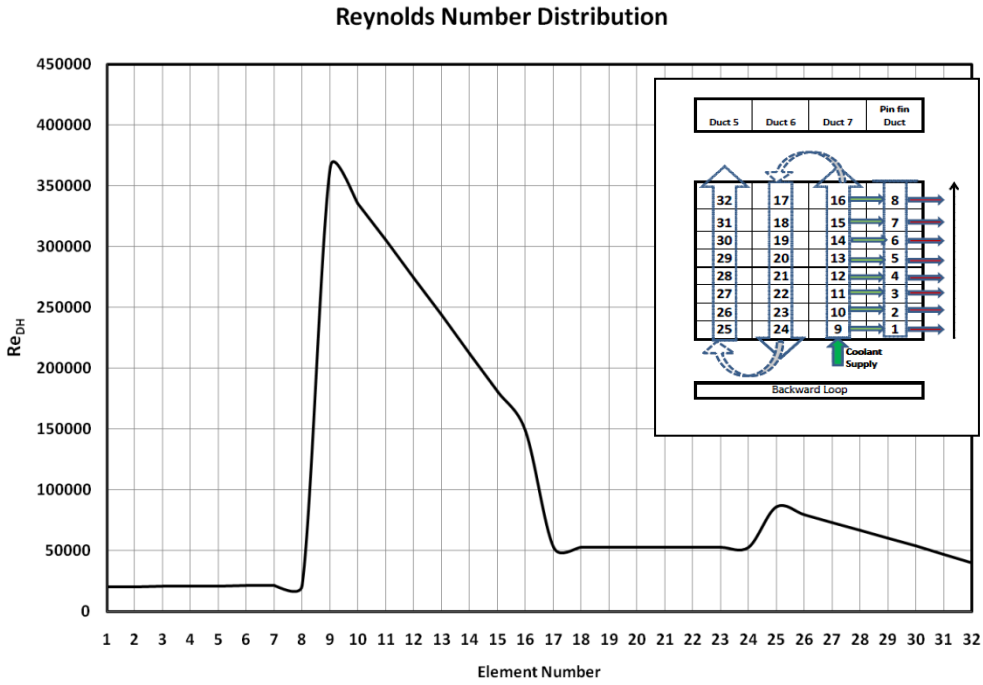

Figure 31– Reynolds number distribution for the backward loop

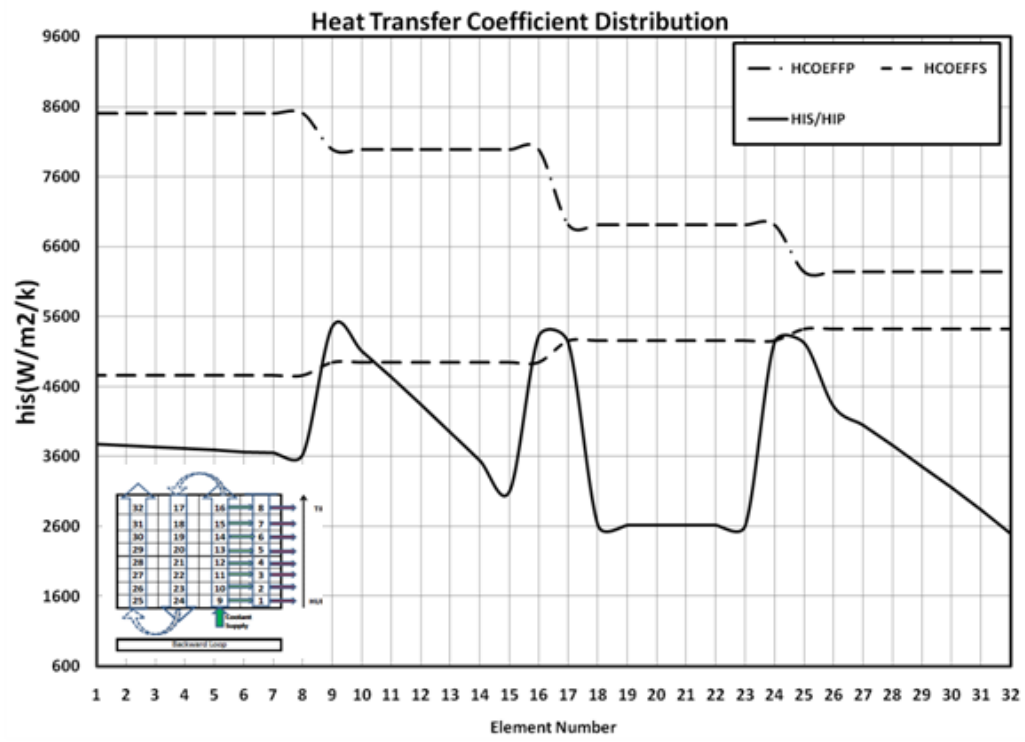

Figure 32– Plot for heat transfer coefficient distribution for the backward loop

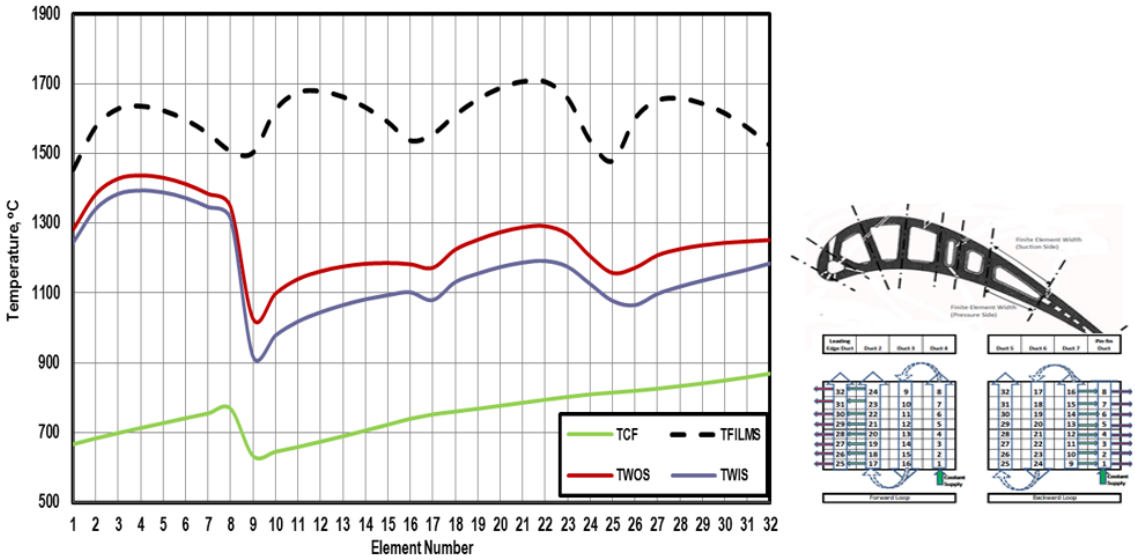

Figure 33–Temperature distribution on suction side pitch line without TBC for the backward loop

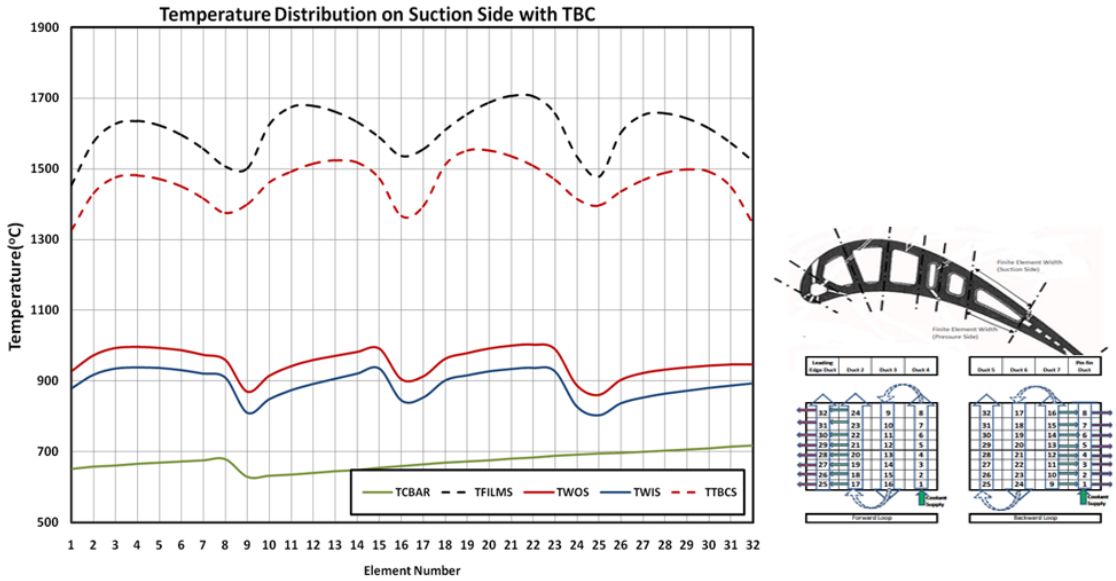

Figure 34– Temperature distribution on suction side pitch line with TBC for the backward loop

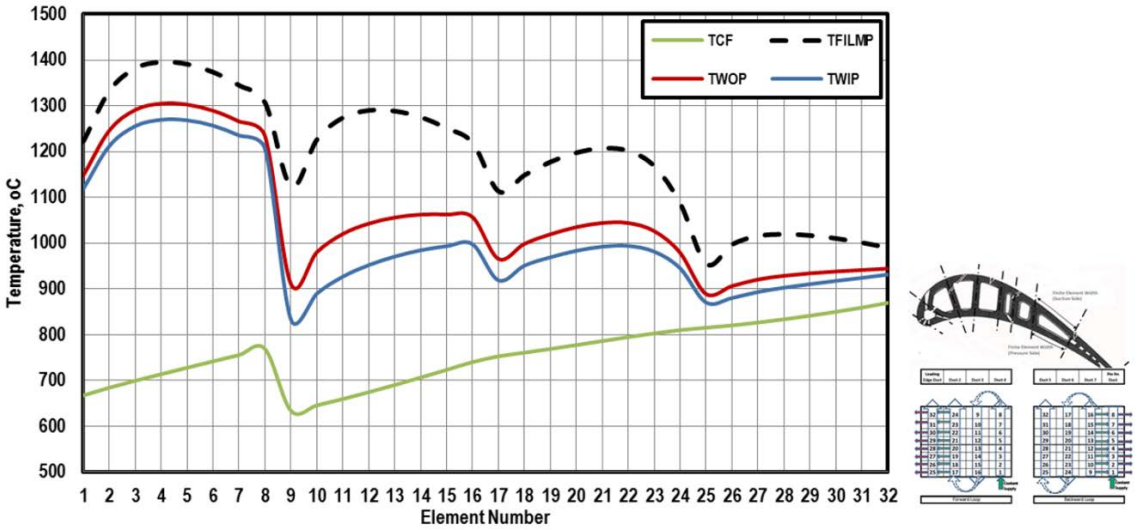

Figure 35–Temperature distribution on pressure side pitch line without TBC for the backward loop

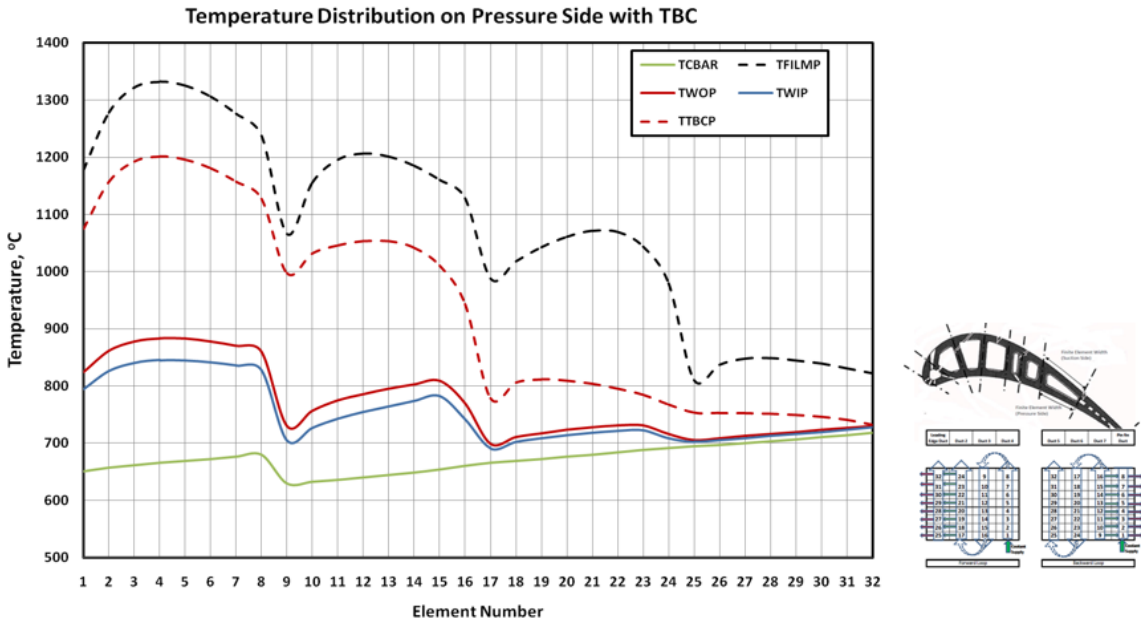

Figure 36– Temperature distribution on pressure side pitch line with TBC for the backward loop

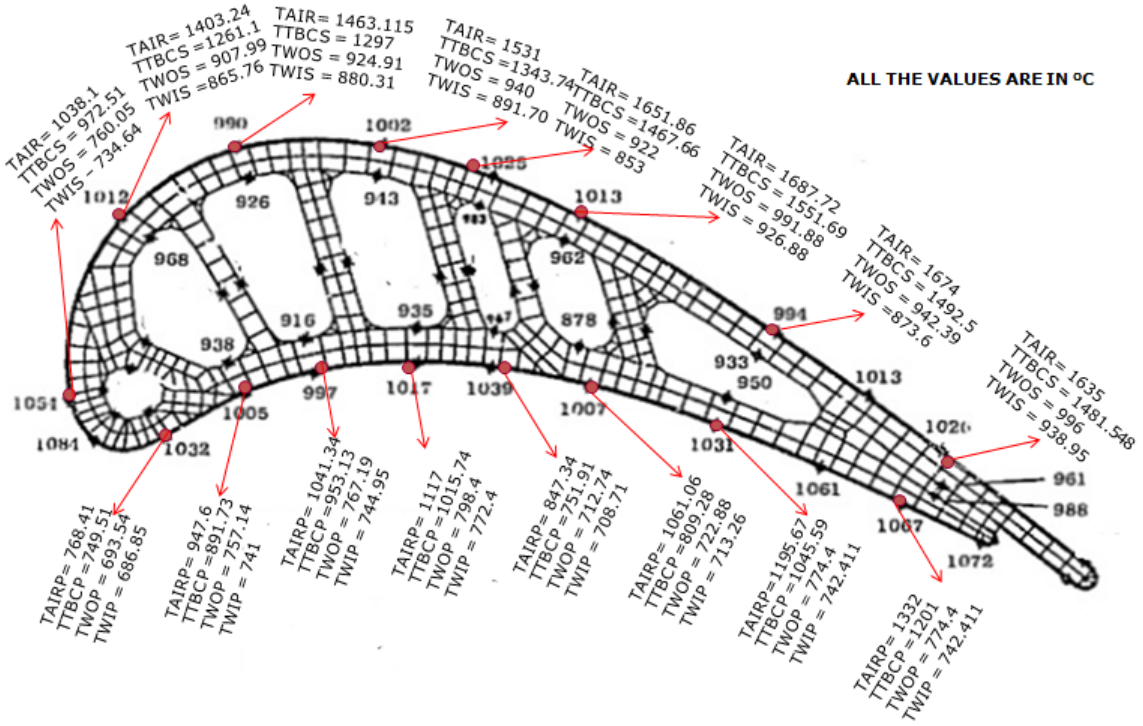

Figure 37– Comparison of temperature results with Halila etal [1].

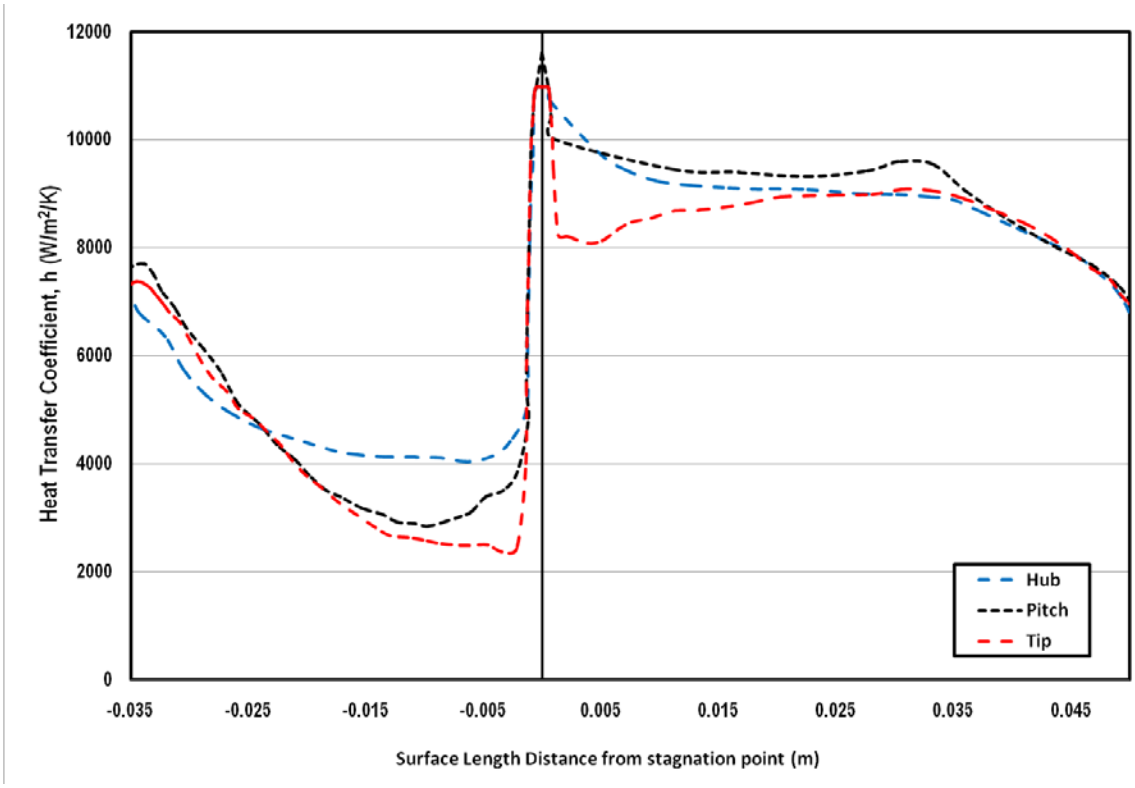

Figure 38– Heat transfer coefficient distribution in hub, pitch and tip region

Results for CASE II: Prediction of temperature distribution for Rotor Inlet Temperature of 1700^{o}C with spanwise variable heat transfer coefficient Distribution

Backward Loop, from Trailing Edge to Mid-Chord

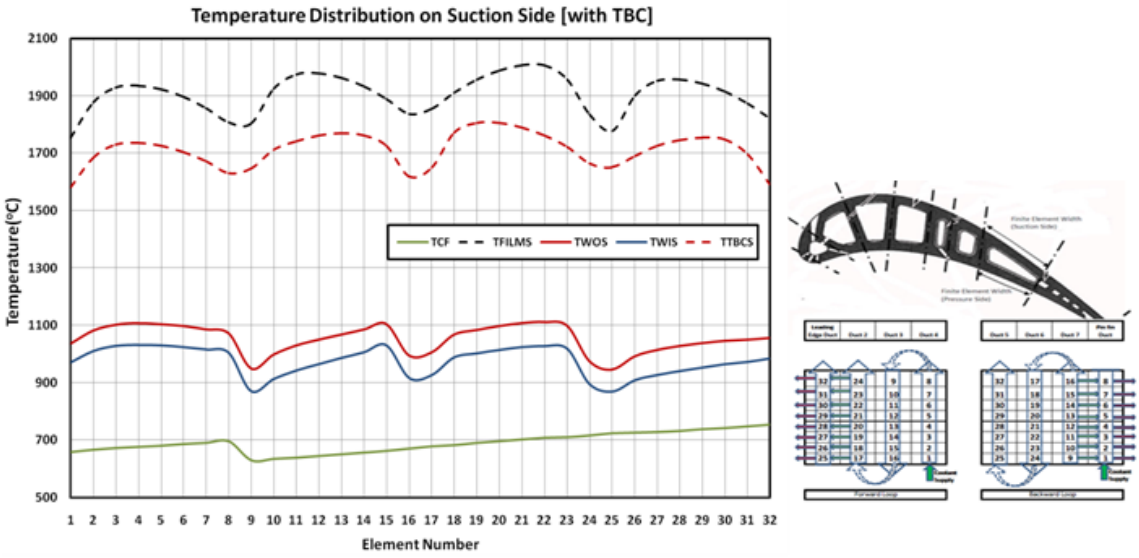

Figure 39– Temperature distribution on suction side pitch line for RIT = 1700^{o}C, Case II

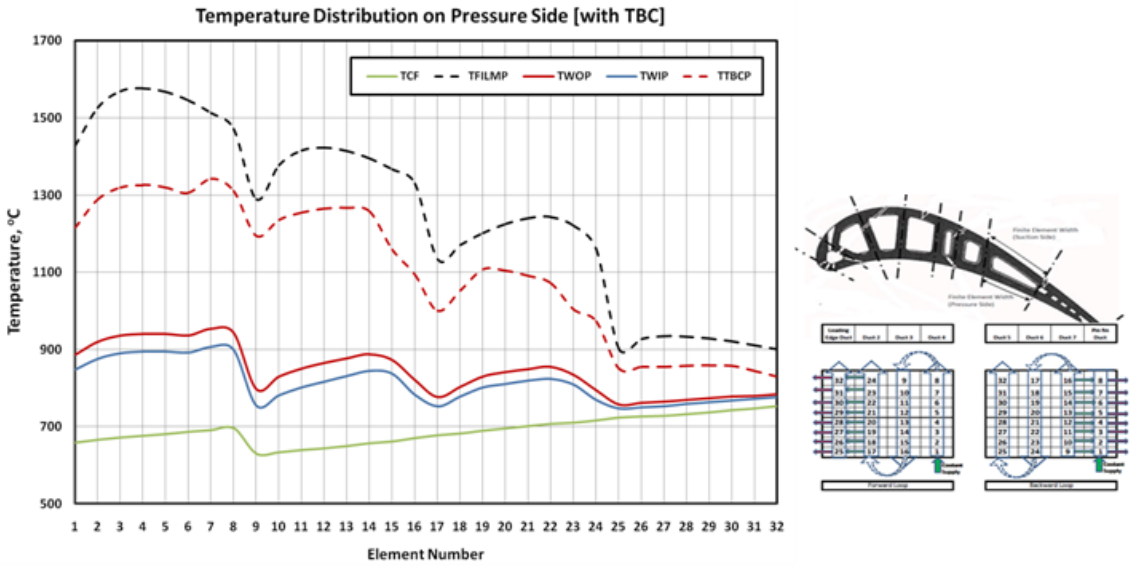

Figure 40– Temperature distribution on pressure side pitch line for RIT = 1700^{o}C, Case II

Forward Loop, from Mid-Chord to Leading Edge

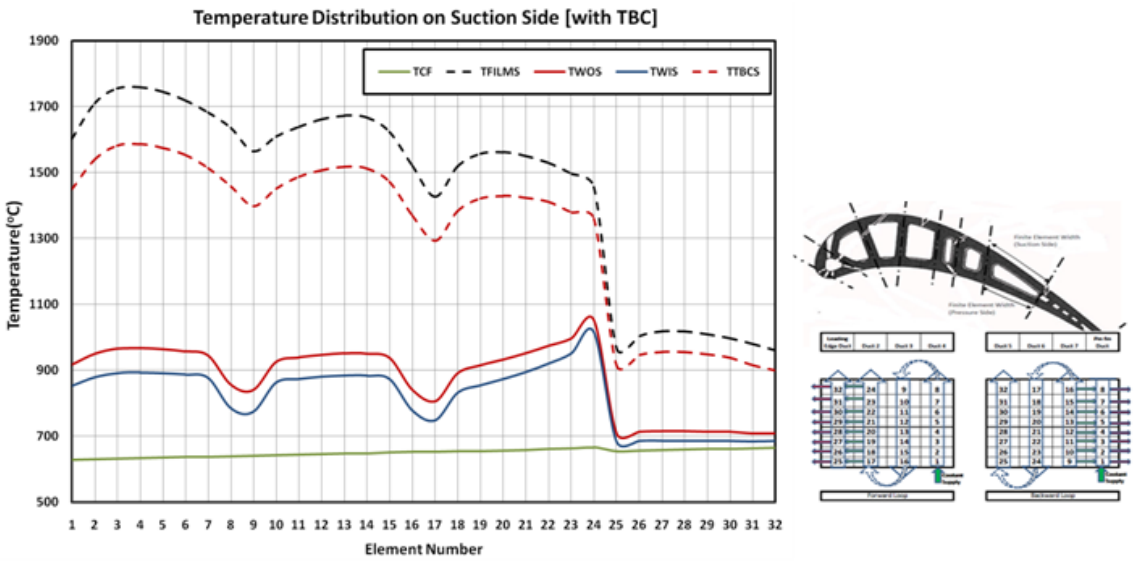

Figure 41– Temperature distribution on suction side pitch line for RIT = 1700°C, Case II

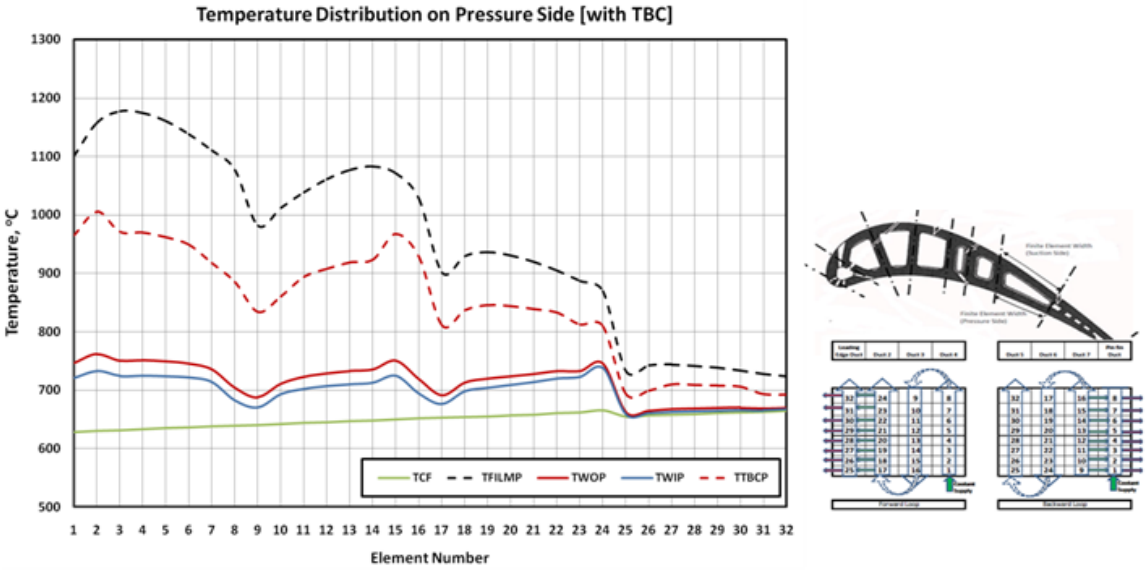

Figure 42– Temperature distribution on pressure side pitch line for RIT = 1700°C, Case II

Tip region temperature distribution

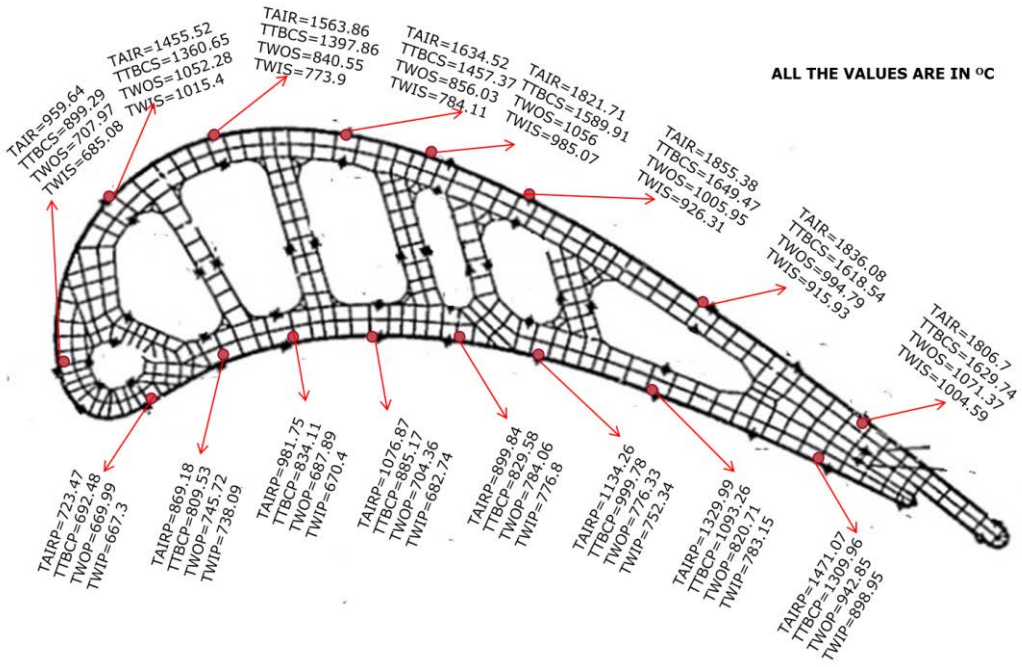

Figure 43– A tip region temperature distribution for the rotor inlet temperature of 1700^{o}C , Case II

Pitch Line Temperature Distribution.

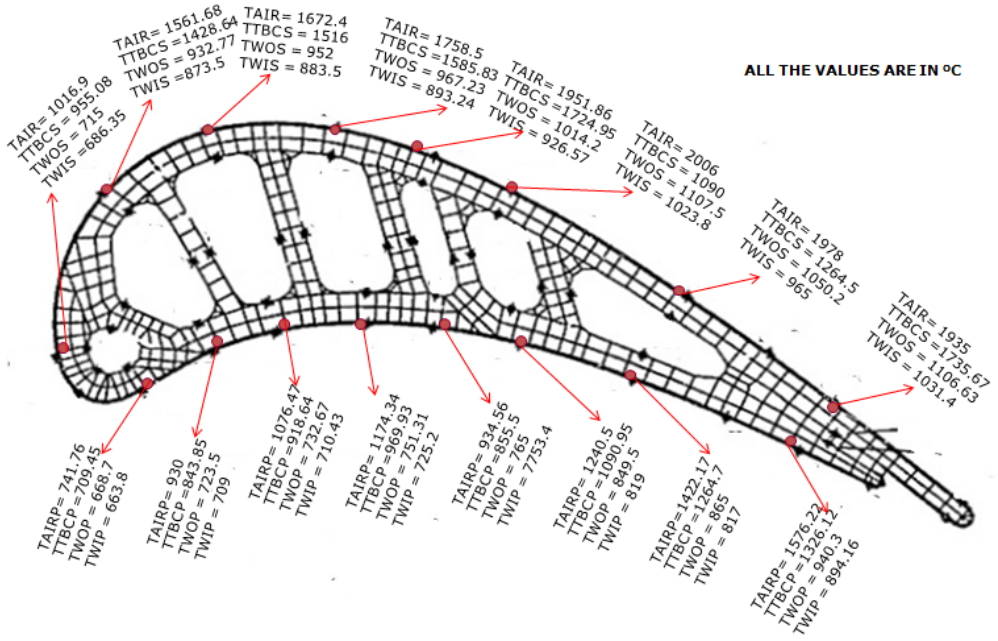

Figure 44– A pitch line temperature distribution for the Rotor inlet temperature of 1700^{o}C, Case II

Hub Region Temperature Distribution

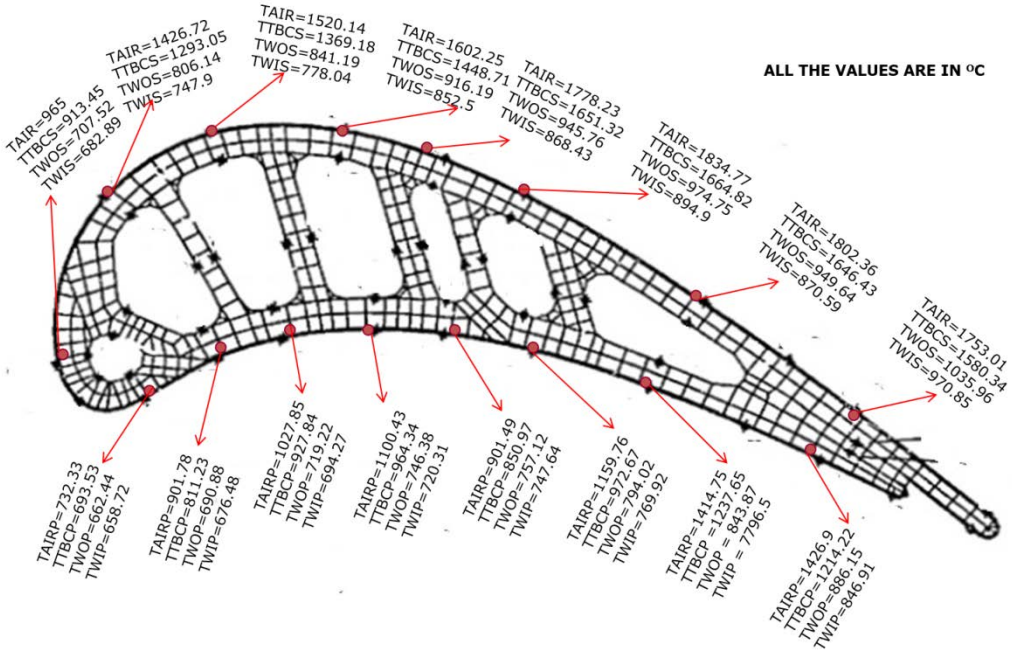

Figure 45– A hub region temperature distribution for the Rotor inlet temperature of 1700^{o}C , Case II

Case III: Prediction of temperature distribution for rotor inlet temperature of 1700^{o}C with transition model

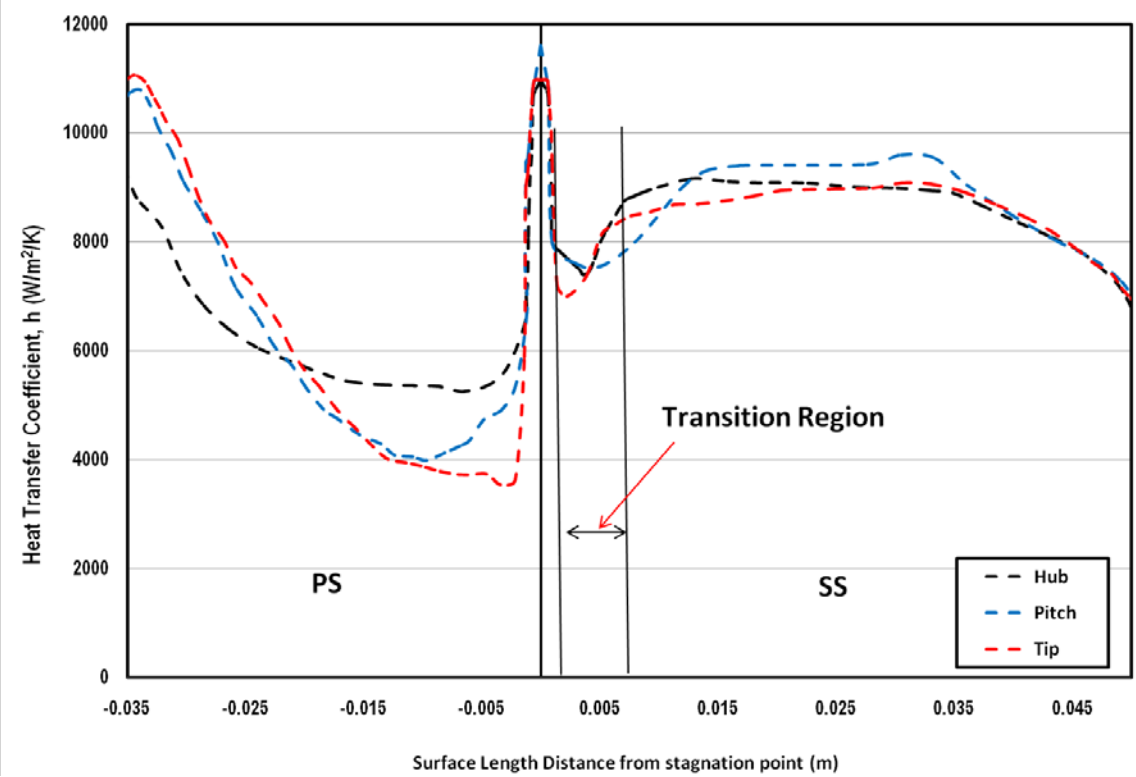

Figure 46– Heat transfer coefficients distributions with transition model, Case III

Backward Loop, from Trailing Edge to Mid-Chord

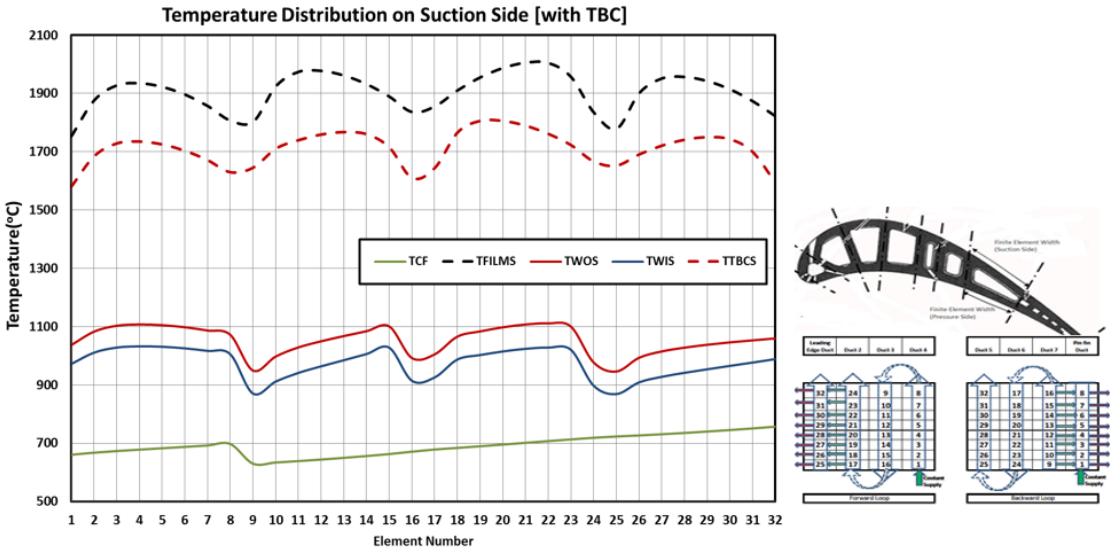

Figure 47– Temperature distribution on suction side pitch line for RIT = 1700°C, Case III

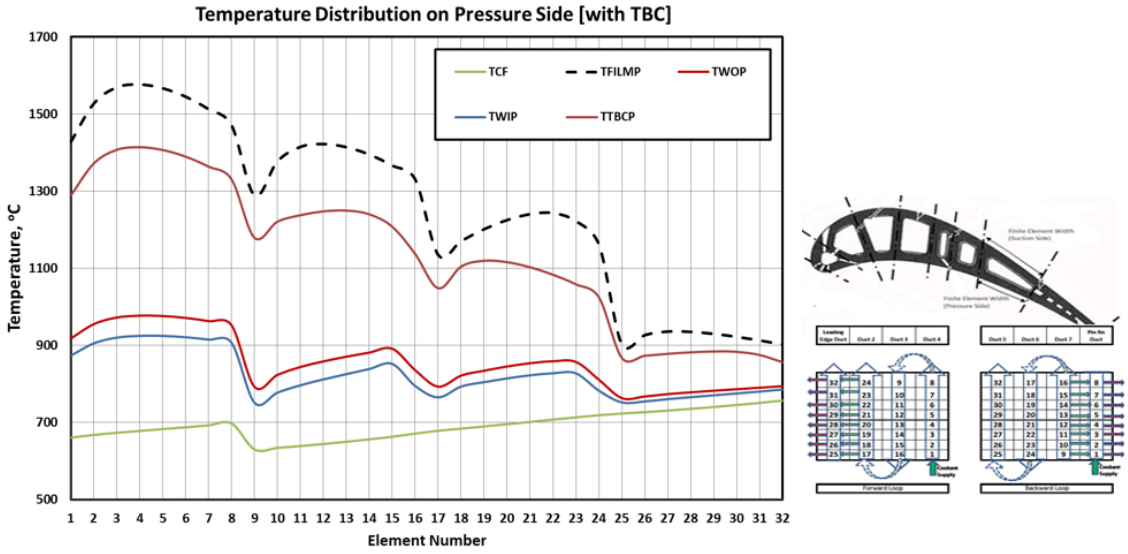

Figure 48– Temperature distribution on pressure side pitch line for RIT = 1700°C, Case III

Forward Loop, from Mid-Chord to Leading Edge

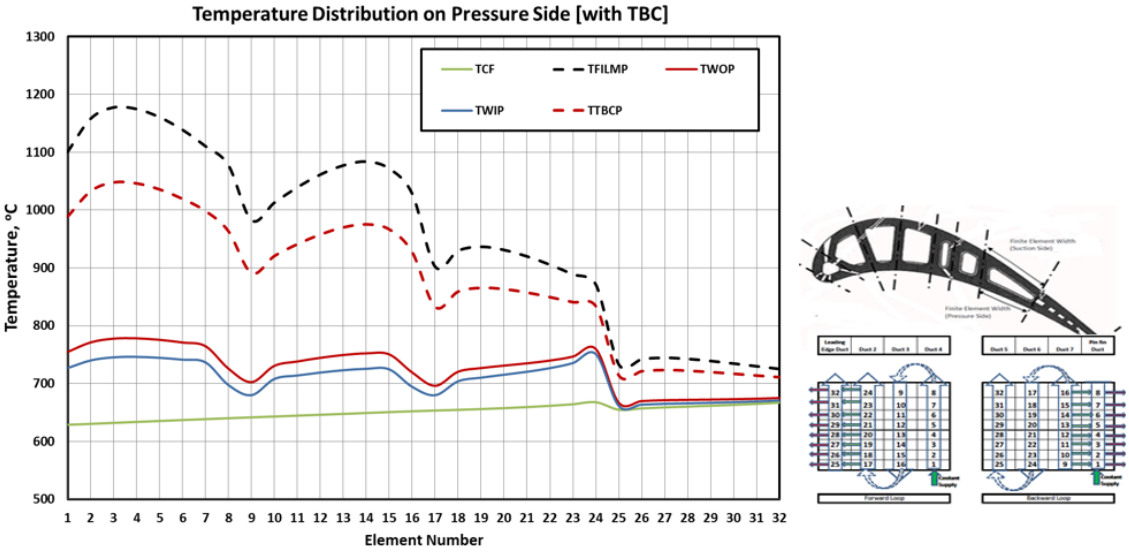

Figure 49: Temperature distribution on pressure side pitch line for RIT = 1700°C, Case III

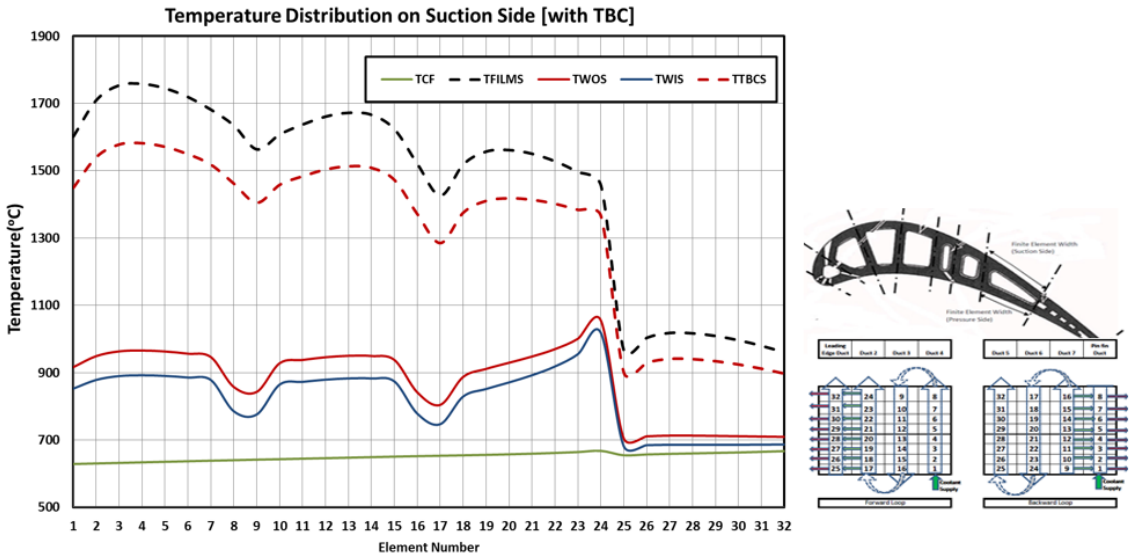

Figure 50: Temperature distribution on suction side pitch line for RIT = 1700°C, Case III

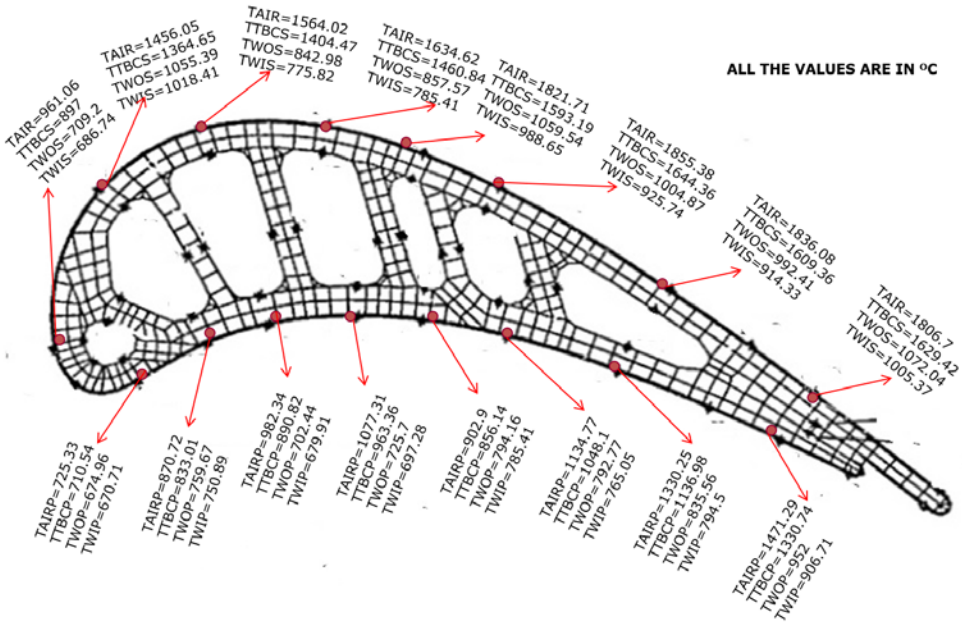

Figure 51– A tip region temperature distribution for the rotor inlet temperature of 1700°C using transition model, Case III

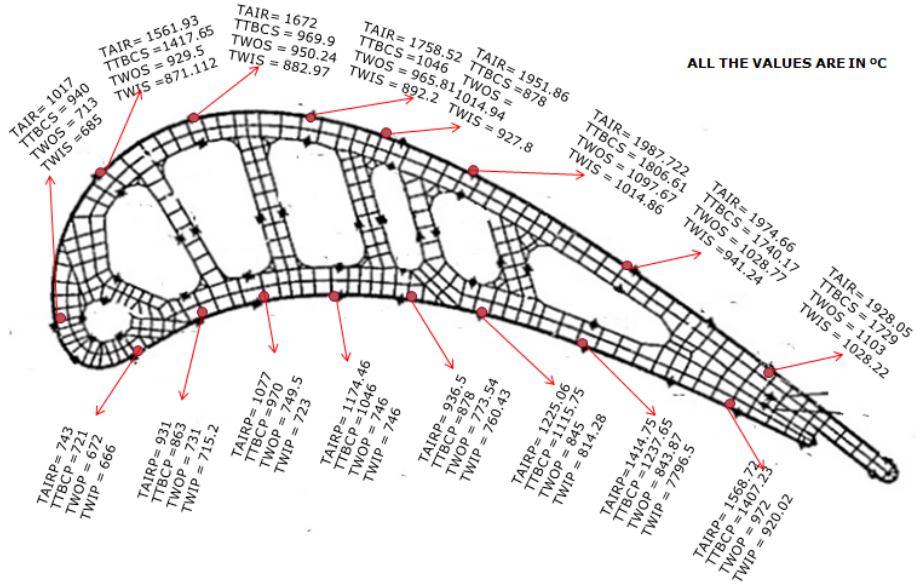

Figure 52– A pitch region temperature distribution for the rotor inlet temperature of 1700°C using transition model, Case III

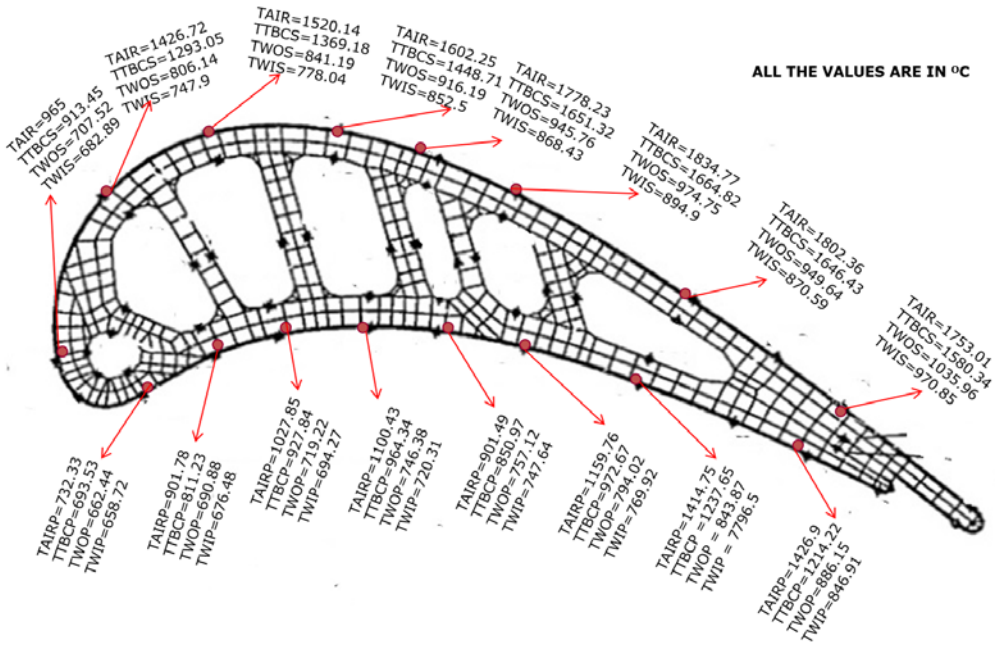

Figure 53– A hub region temperature distribution for the rotor inlet temperature of 1700^{o}C using transition model, Case III

Case IV: Prediction for Samsung rotor-2 blade model

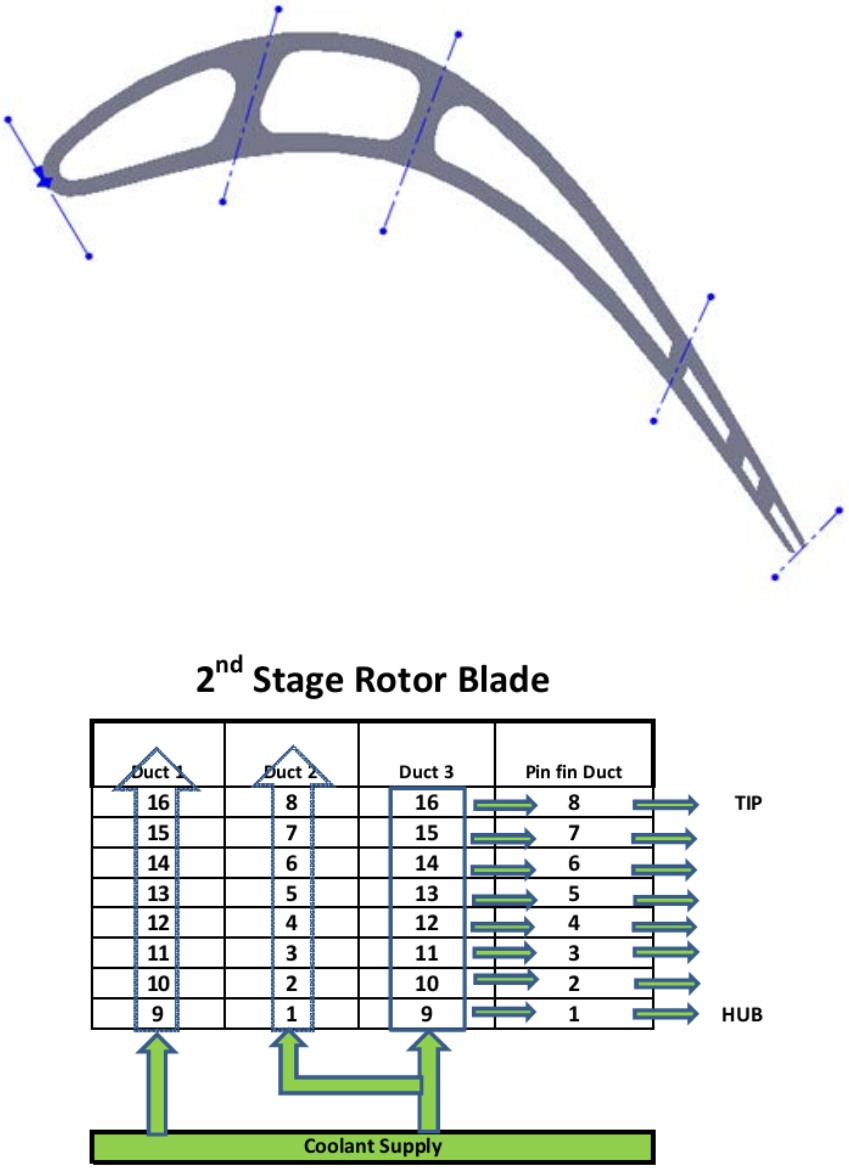

Figure 54– 2D model of Samsung Rotor-2 blade and schematic of the flow loop

Rotor Inlet Temperature Profile [Spanwise]

T[K]=-607764.4831*SPFR^10+2923804.544*SPFR^9-
5856072.843*SPFR^8+6262005.512*SPFR^7-
3753649.543*SPFR^6+1139976.242*SPFR^5-62557.77468*SPFR^4-
58960.28909*SPFR^3+13260.48395*SPFR^2-27.10878095*SPFR+1212.606325;

Rotor Inlet Velocity Profile [Spanwise]

V_{INLET}[m/s]=-299736.377171179*SPFR^10+1415160.47690428*SPFR^9-
2825130.33122626*SPFR^8+3098717.30022373*SPFR^7-
2024593.46766502*SPFR^6+793165.098727245*SPFR^5-
175413.011872371*SPFR^4+18692.8152199246*SPFR^3-
1235.26376694511*SPFR^2+380.157878015824*SPFR+547.462074025032;

Pressure Side Velocity Profile [Chordwise]

V[m/s]=(-1727.57106339930*XPFRAC^10+10857.8933333873*XPFRAC^9-
28729.9410164034*XPFRAC^8+42163.7457979012*XPFRAC^7-
37886.2284680364*XPFRAC^6+21642.2591602242*XPFRAC^5-
7885.83898074005*XPFRAC^4+1787.11335371821*XPFRAC^3-
235.154064424157*XPFRAC^2+14.7173855412453*XPFRAC+0.301976265114326)*
VINLET;

Suction Side Velocity Profile [Chordwise]

V[m/s] = (172194.074264972*XSFRAC^14-
912996.125101467*XSFRAC^13+1698837.98266924*XSFRAC^12-
432896.075266311*XSFRAC^11-
3605043.5606738*XSFRAC^10+7344902.87049321*XSFRAC^9-
7529997.17365646*XSFRAC^8+4827954.72874181*XSFRAC^7-
2044517.61804261*XSFRAC^6+
576138.971536741*XSFRAC^5-105959.834643472*XSFRAC^4+
12157.7648531900*XSFRAC^3-802.510811862545*XSFRAC^2+
27.2728535640343*XSFRAC^1+ 0.516582856024660)*V_{INLET}

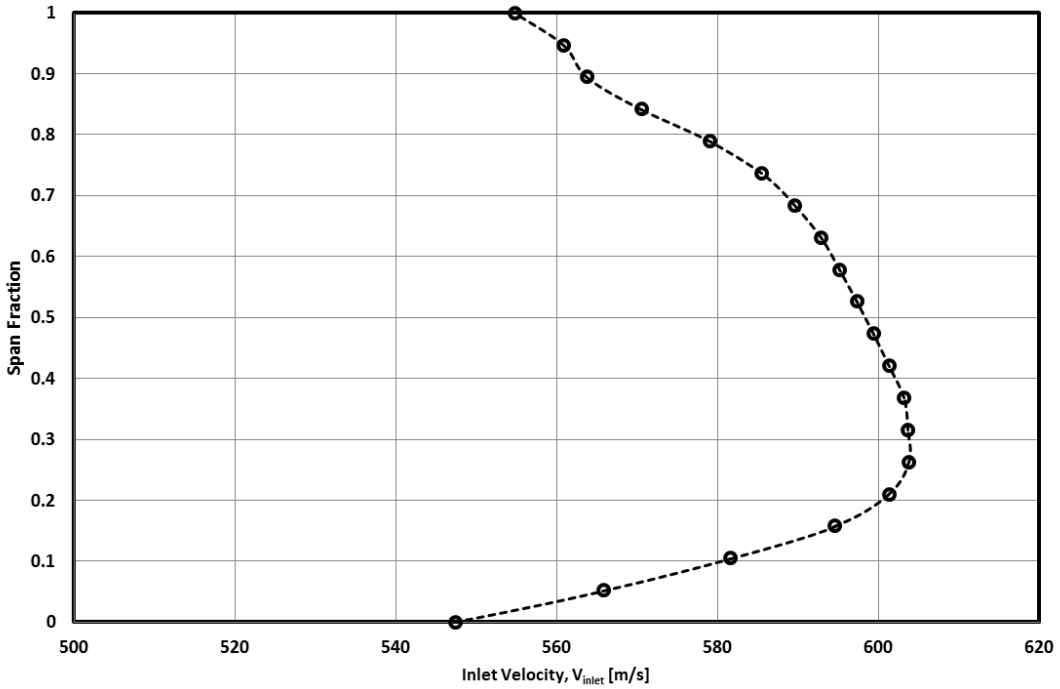

Figure 55– Spanwise velocity distribution, Case IV

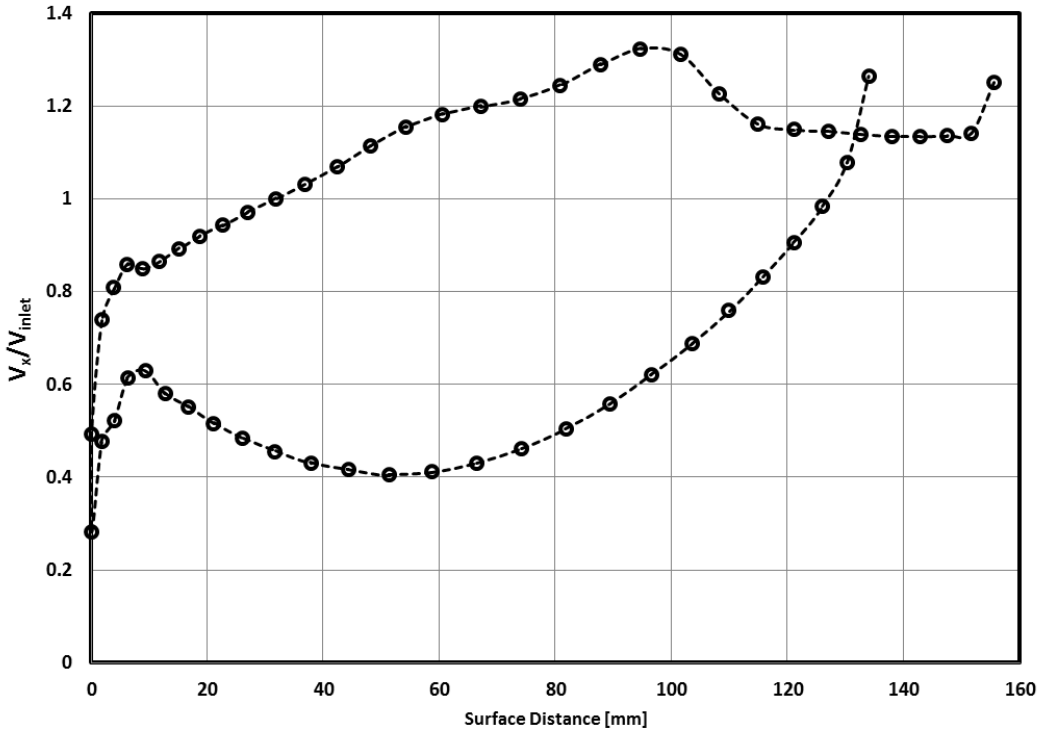

Figure 56– Chordwise velocity distribution [normalized by spanwise velocity] , Case IV

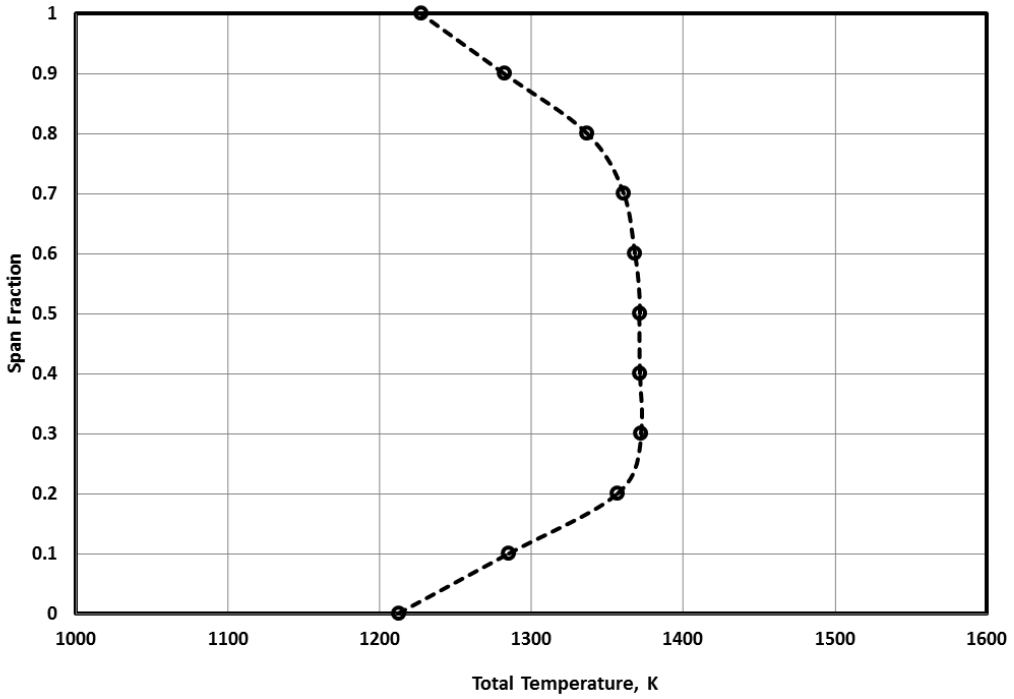

Figure 57– Spanwise reference temperature distribution, Case IV

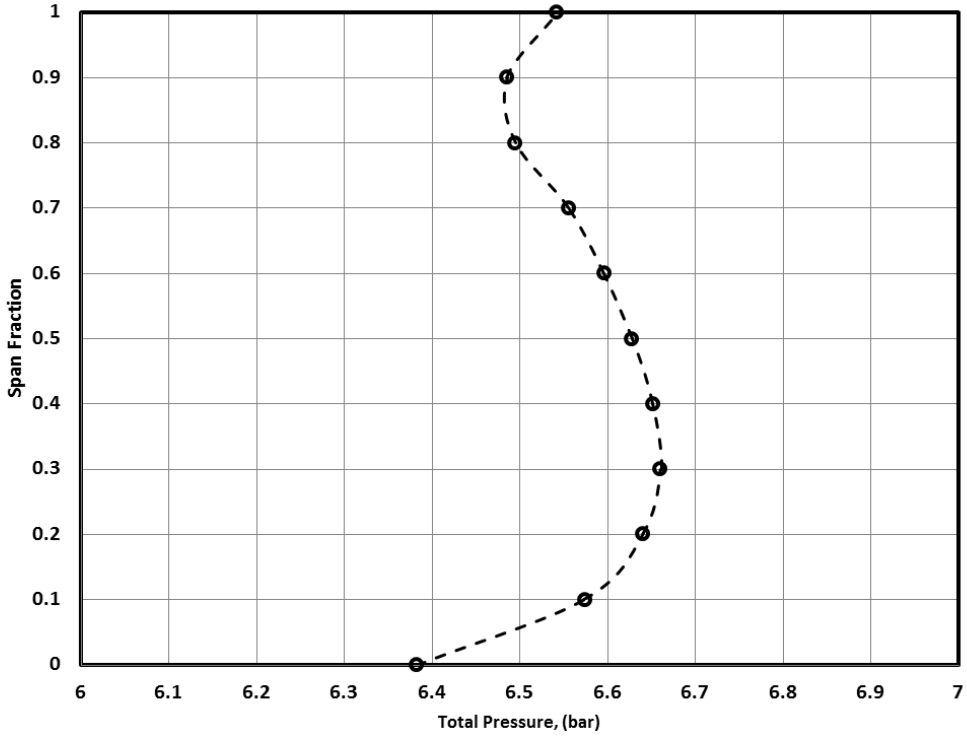

Figure 58– Spanwise total pressure distribution, Case IV

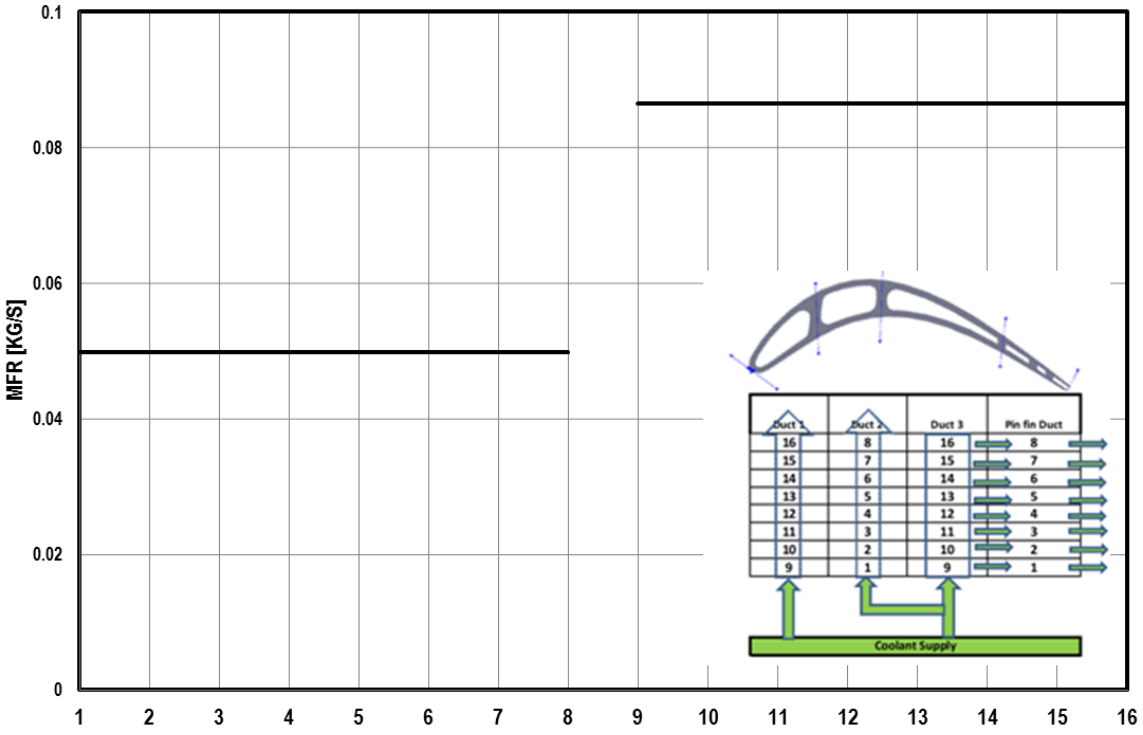

Figure 59– Mass flow rate (MFR) distribution for forward loop, Case IV

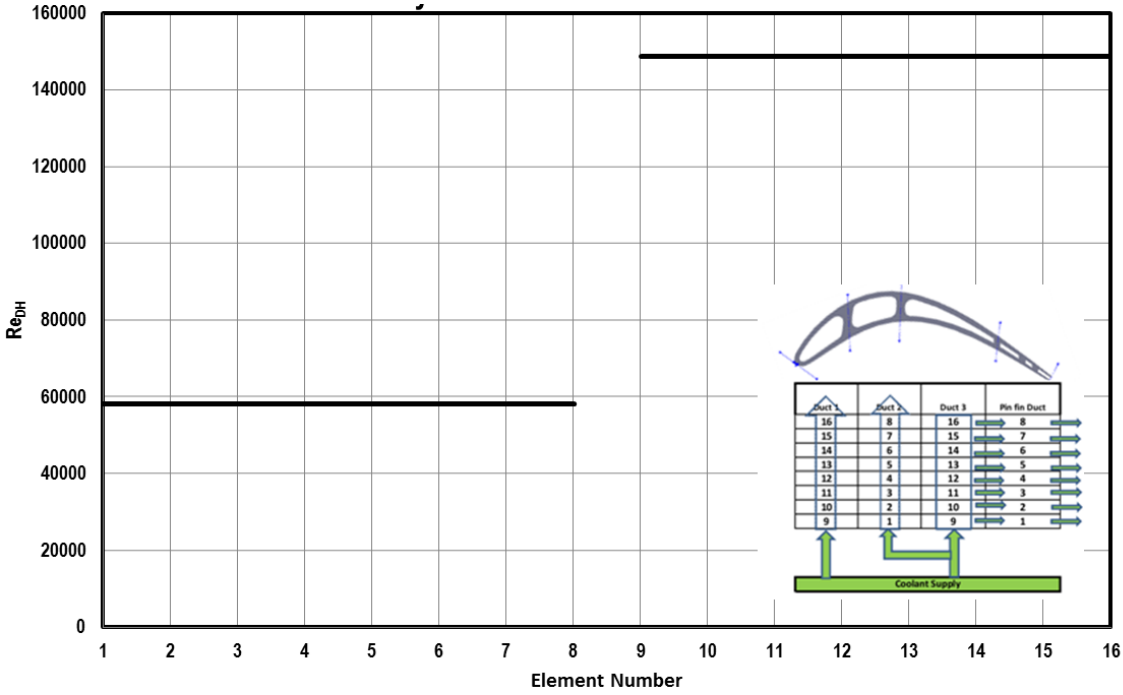

Figure 60– Reynolds number distribution for forward loop, Case IV

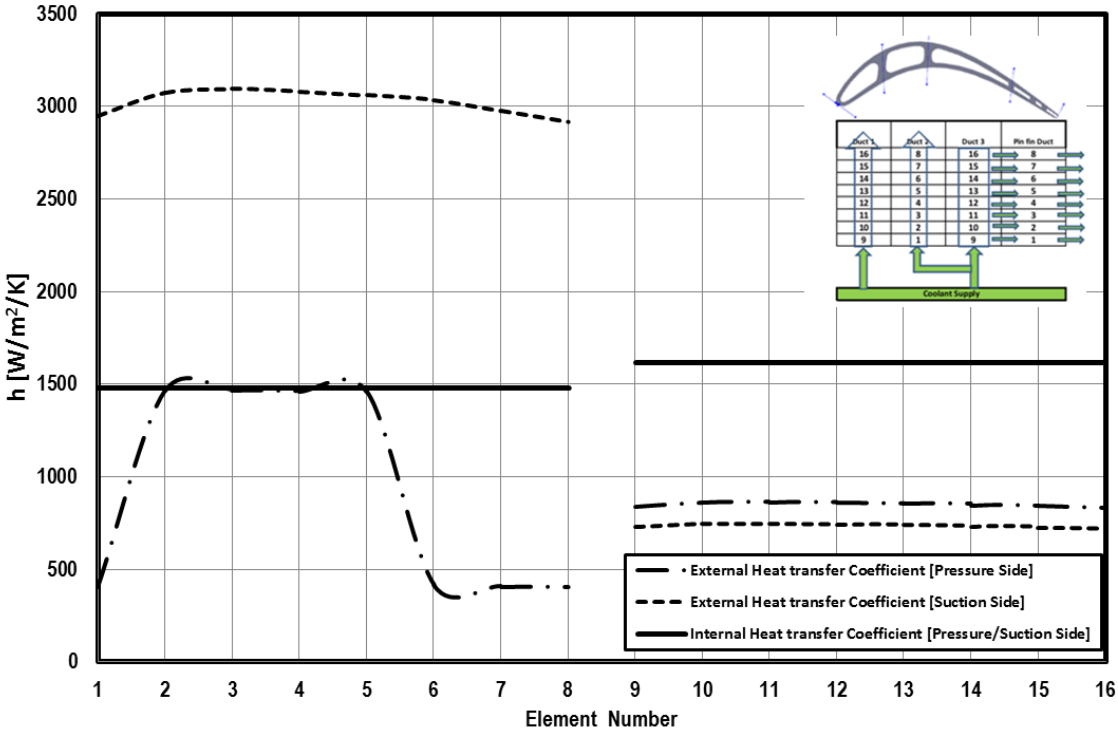

Figure 61– HTC distribution for forward loop, Case IV

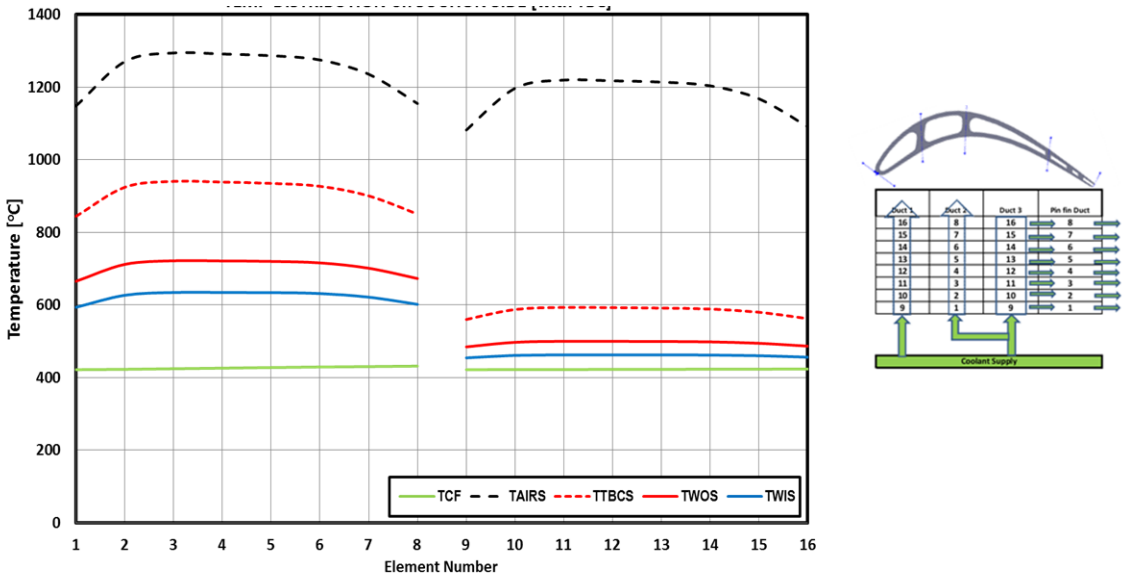

Figure 62– Temperature distribution on suction side for forward loop [with TBC] , Case IV

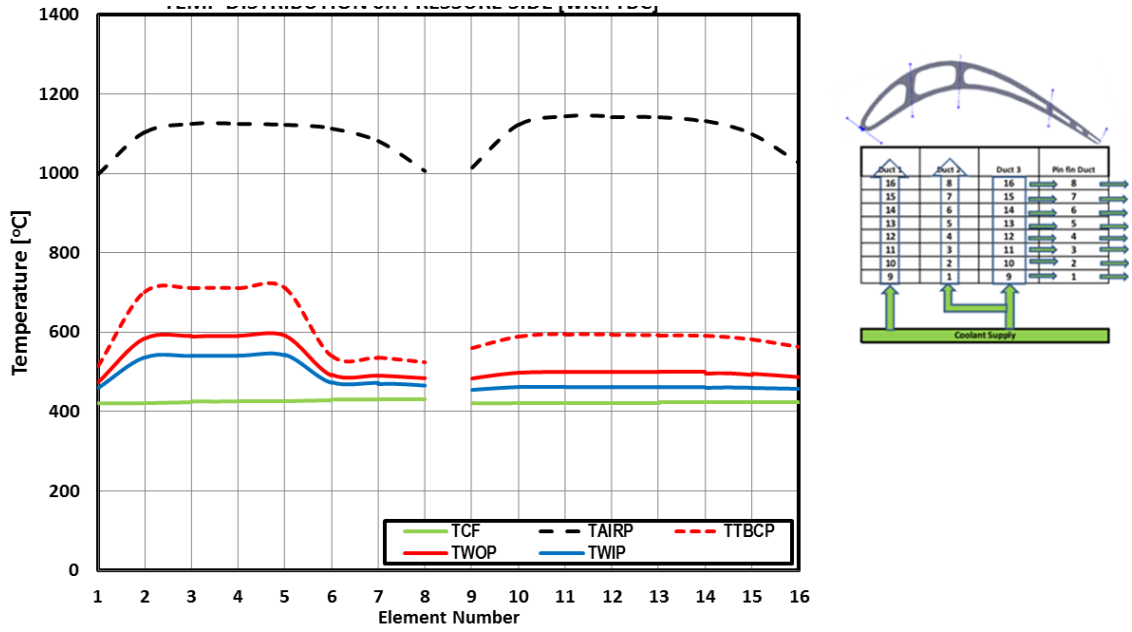

Figure 63– Temperature distribution on pressure side for forward loop [with TBC], Case IV

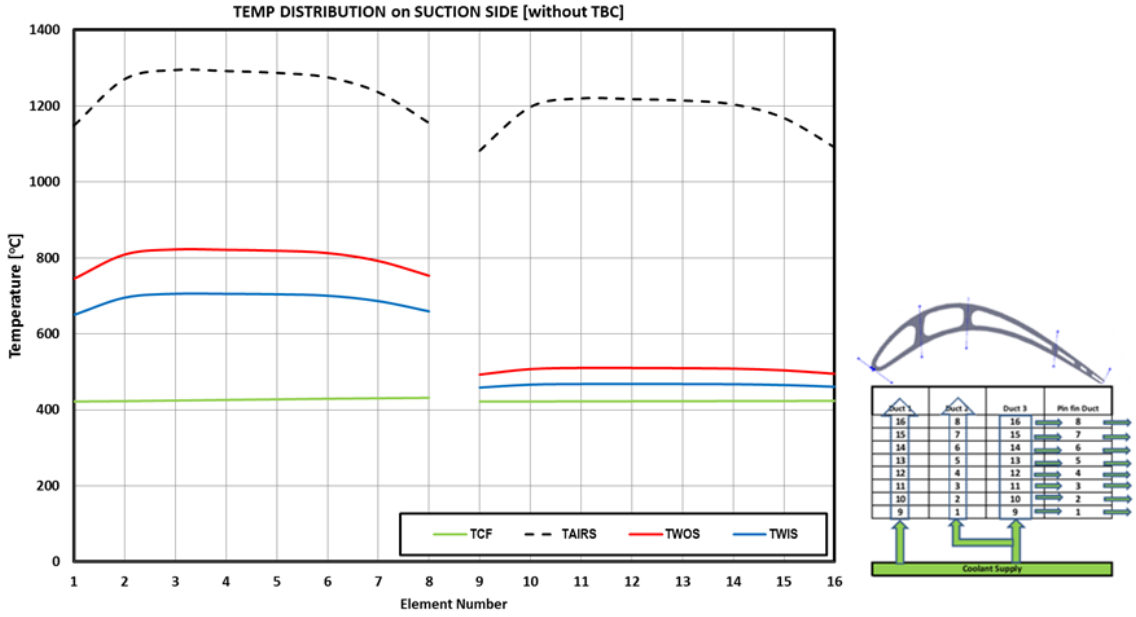

Figure 64– Temperature distribution on suction side for forward loop [without TBC], Case IV

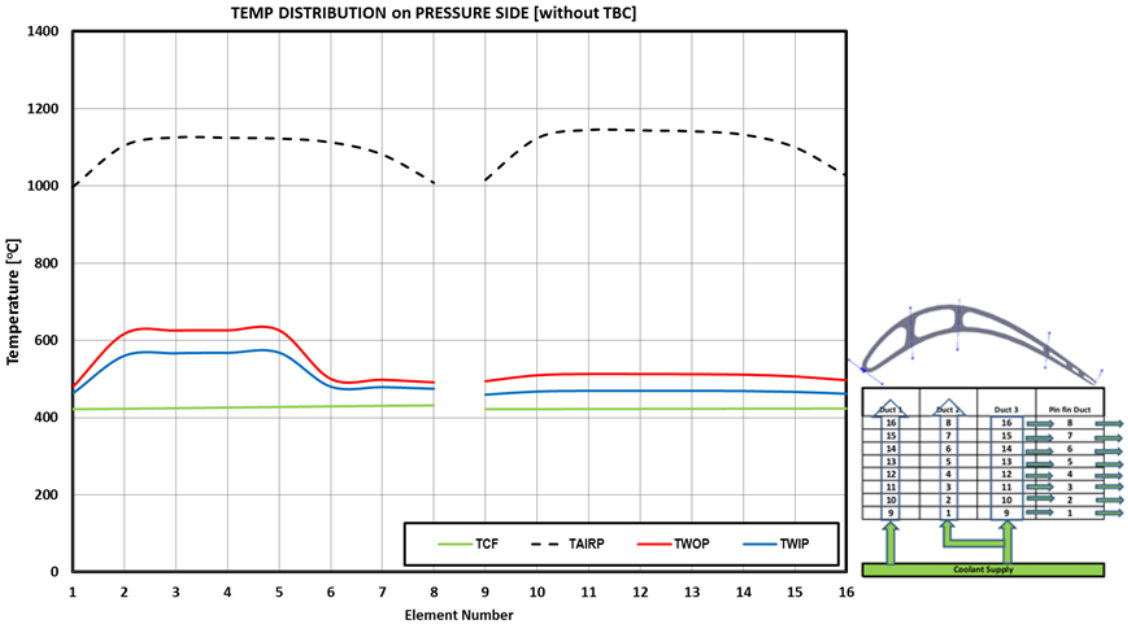

Figure 65– Temperature distribution on pressure side for forward loop [without TBC], Case IV

Backward Loop, from Trailing Edge to Mid-Chord

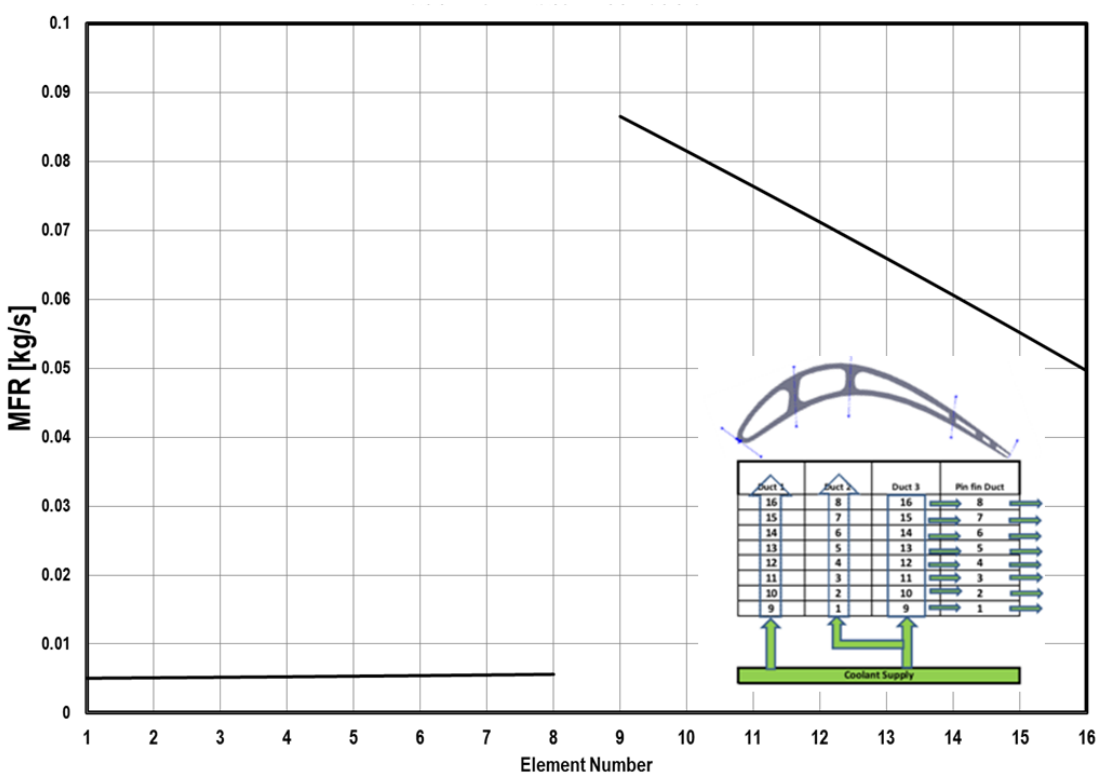

Figure 66– Mass flow rate (MFR) distribution for backward loop, Case IV

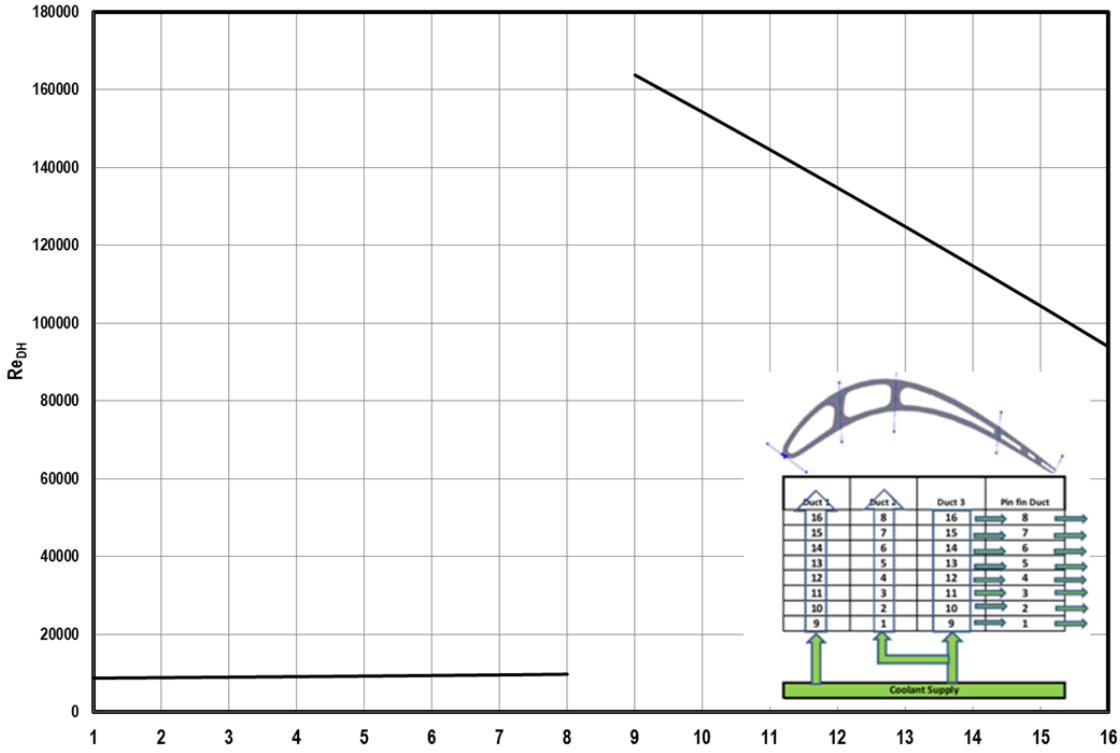

Figure 67– Reynolds number distribution for backward loop, Case IV

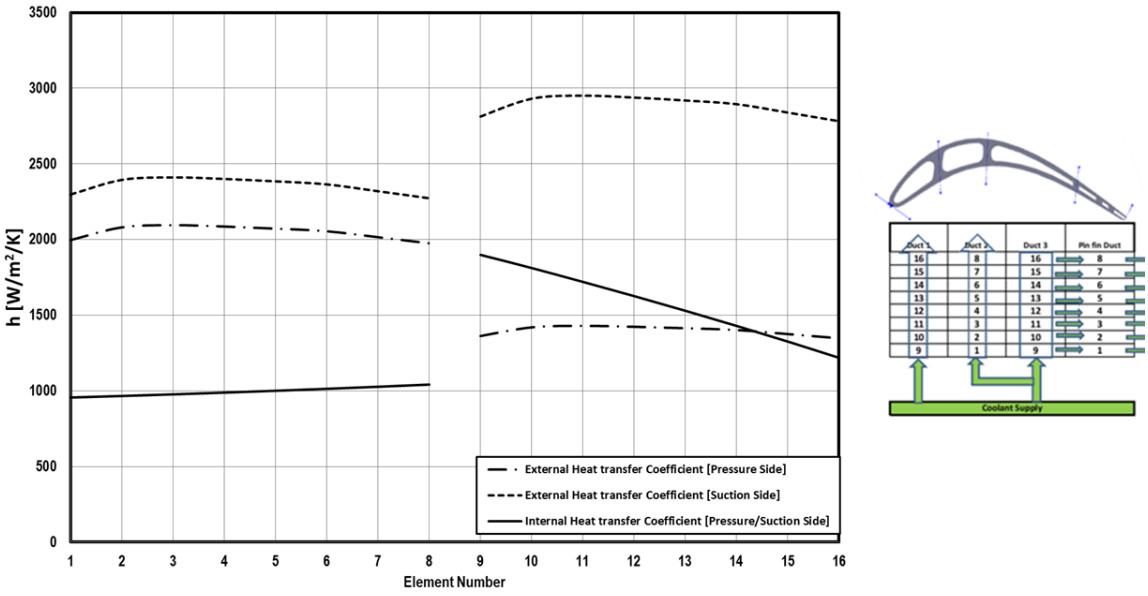

Figure 68– HTC distribution for backward loop, Case IV

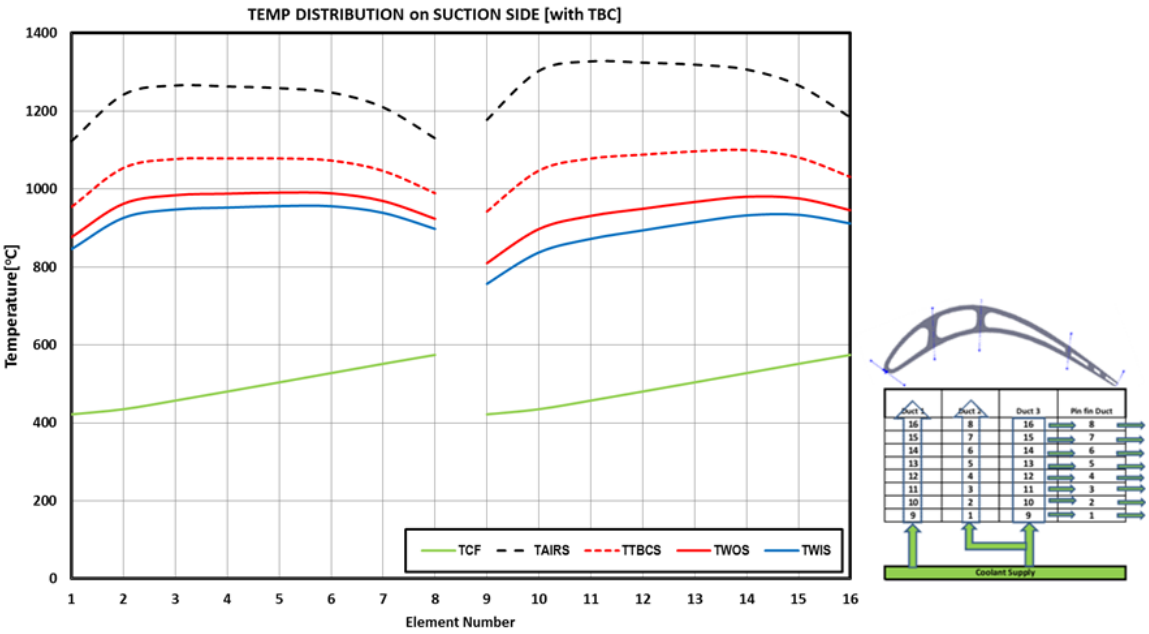

Figure 69– Temperature distribution on suction side for backward loop [with TBC] , Case IV

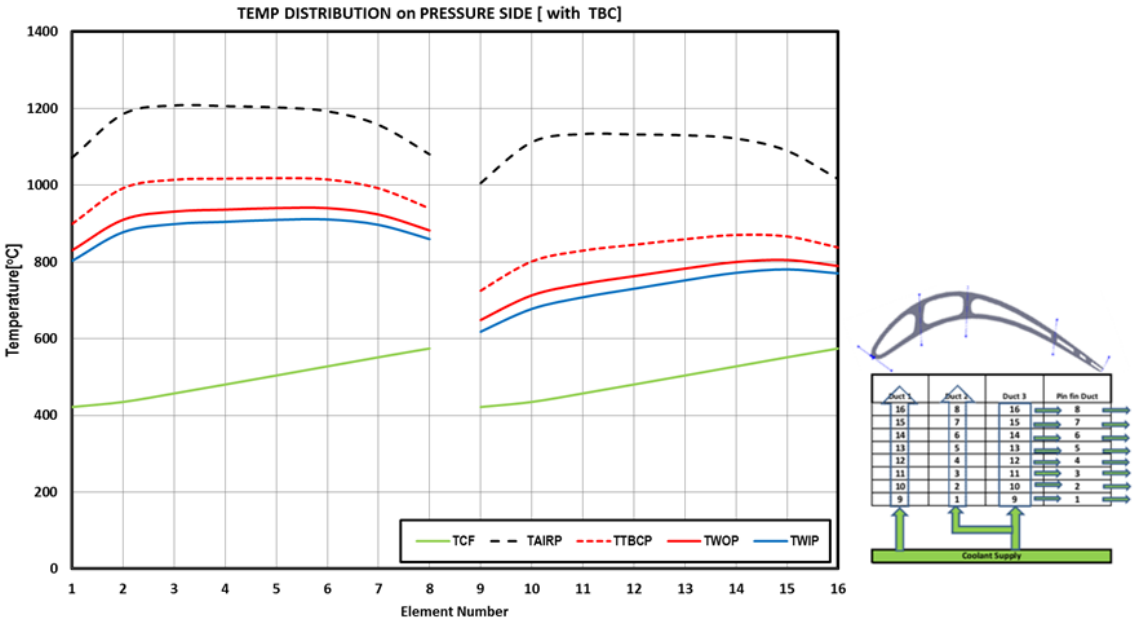

Figure 70– Temperature distribution on pressure side for backward loop [with TBC] , Case IV

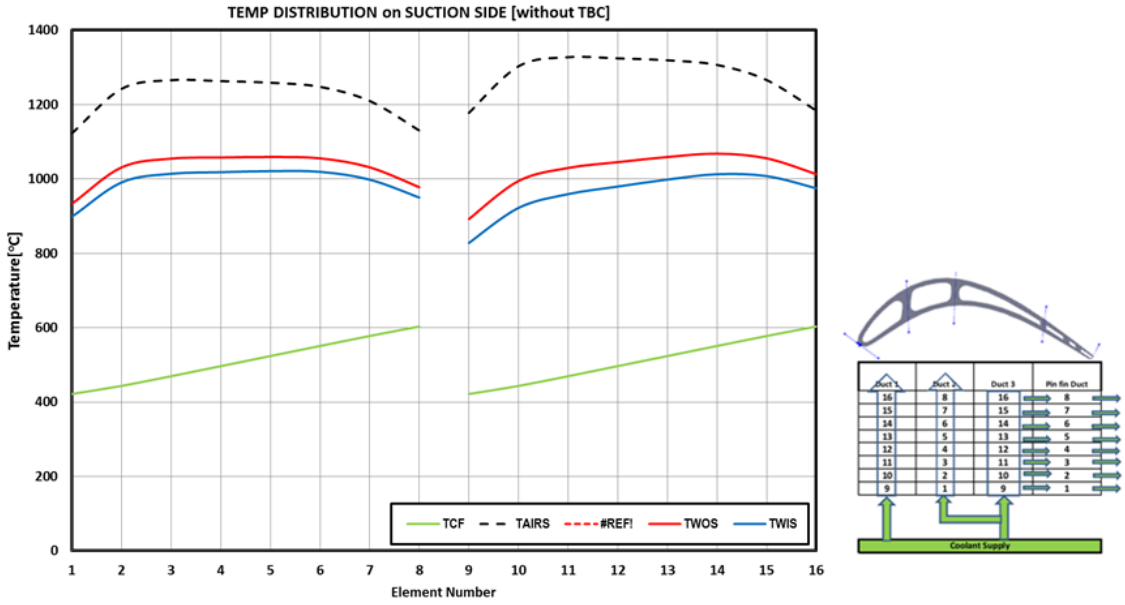

Figure 71– Temperature distribution on suction side for backward loop [without TBC] , Case IV

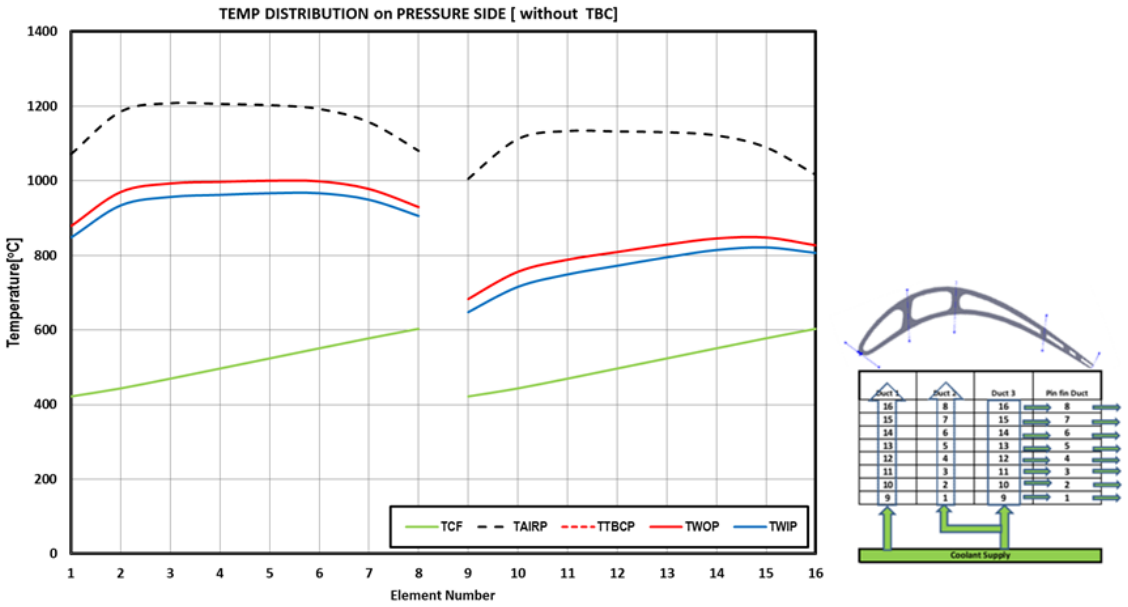

Figure 72– Temperature distribution on pressure side for backward loop [without TBC] , Case IV

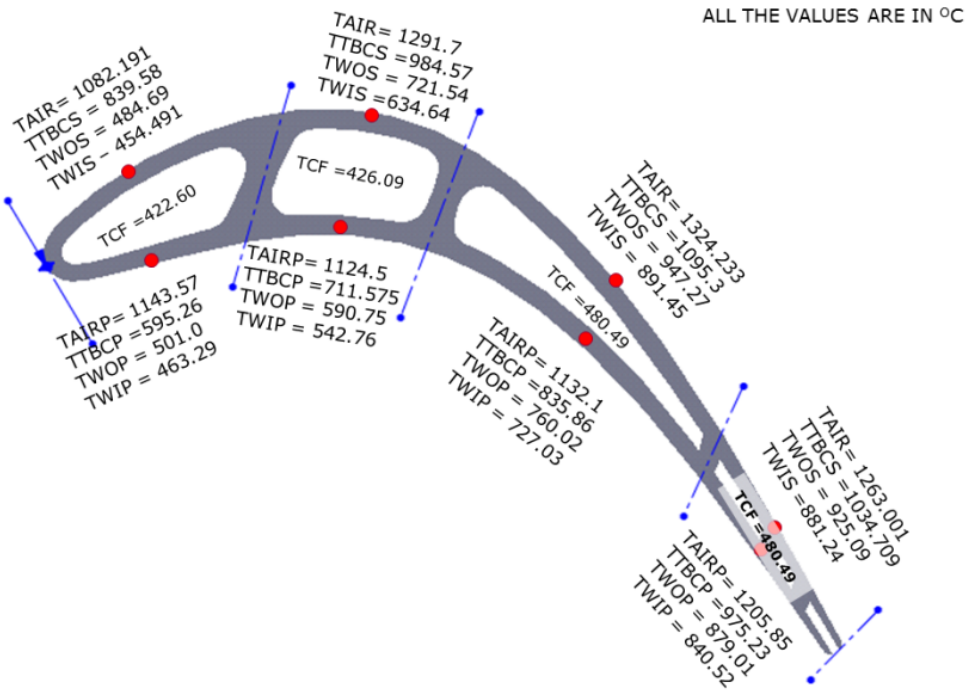

Figure 73– 2D Temperature distribution for Samsung-Rotor2 blade [with TBC] , Case IV

Part IV: Temperature distribution for rotor inlet temperature of 1700^{o}C using heat transfer coefficient results from CFD back in the Code

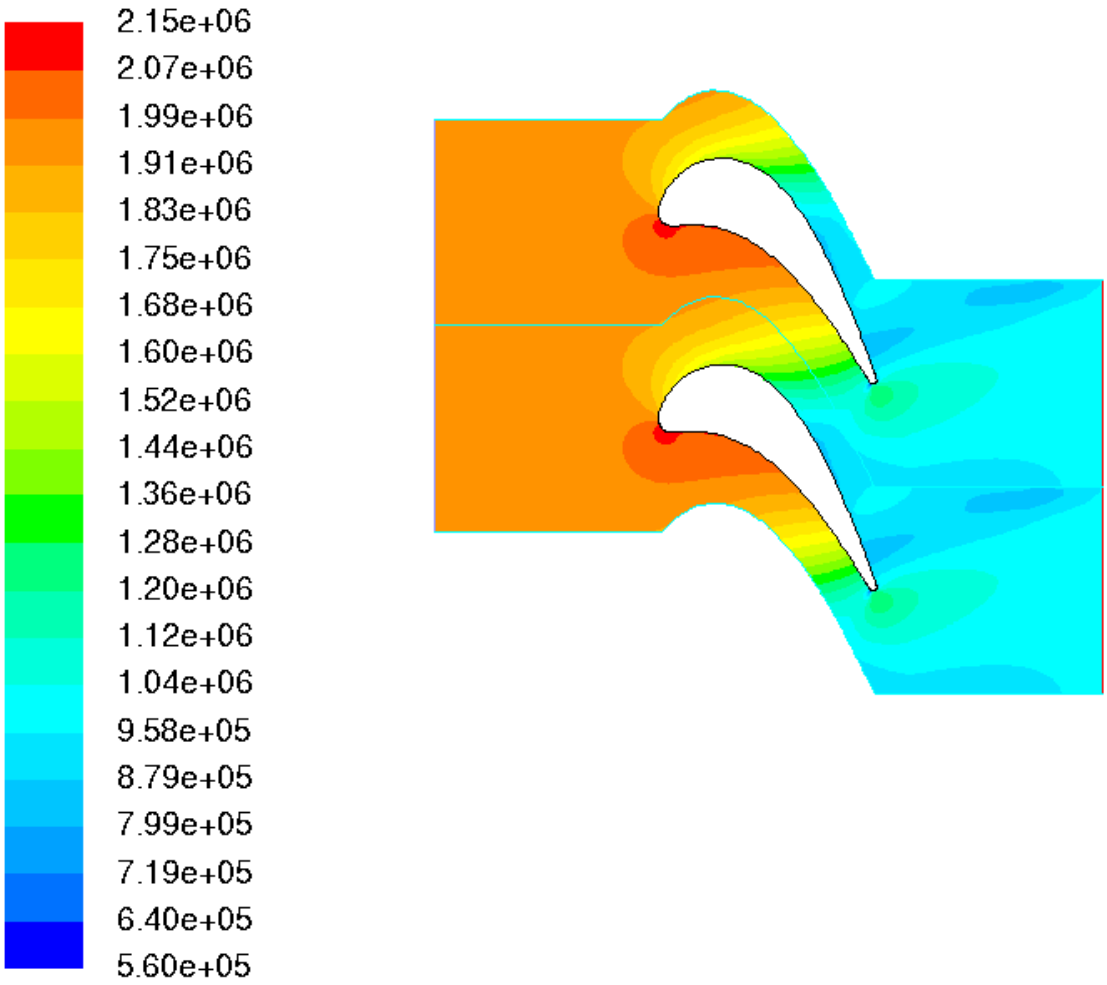

Figure 74–Contours of static pressure, Standard k-epsilon

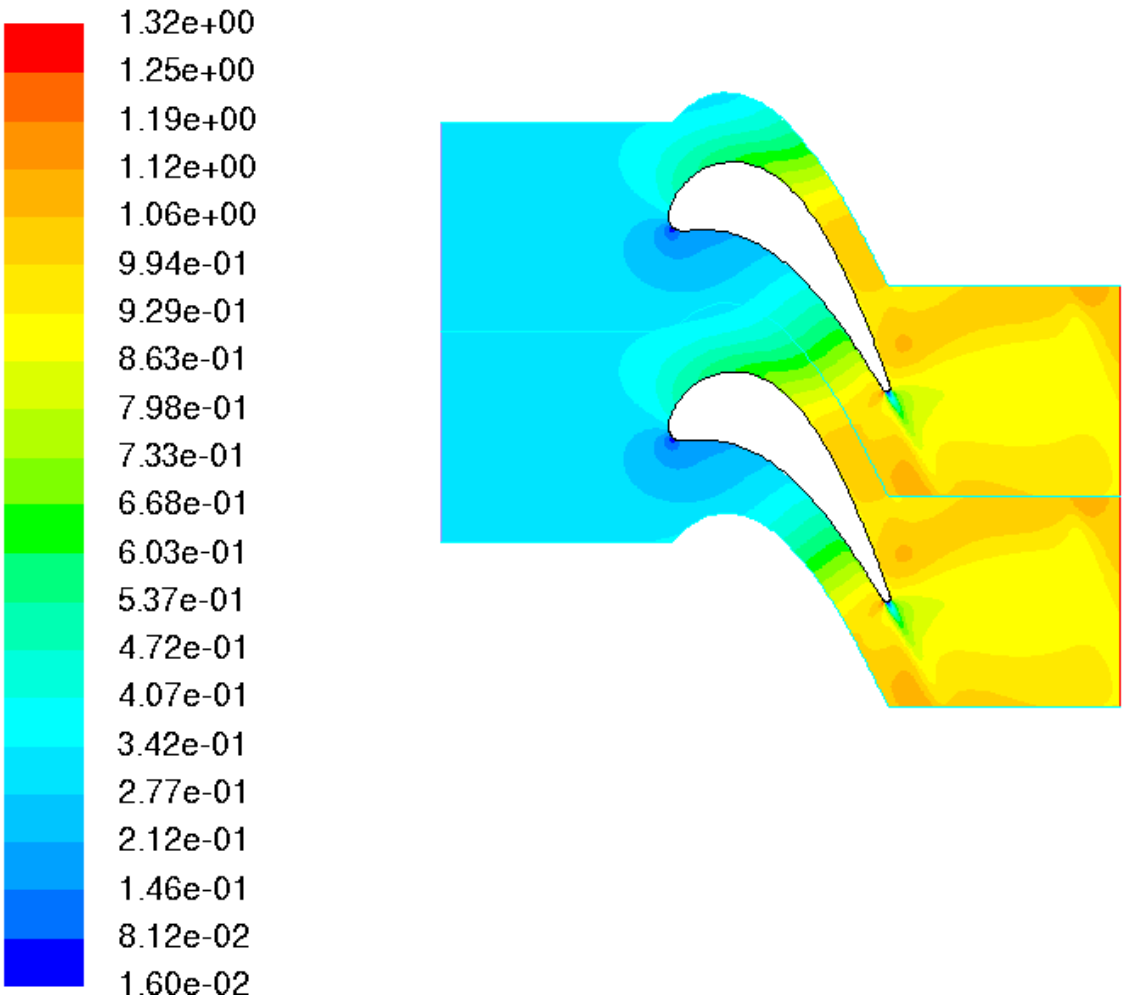

Figure 75– Contours of Mach number, Standard k-epsilon

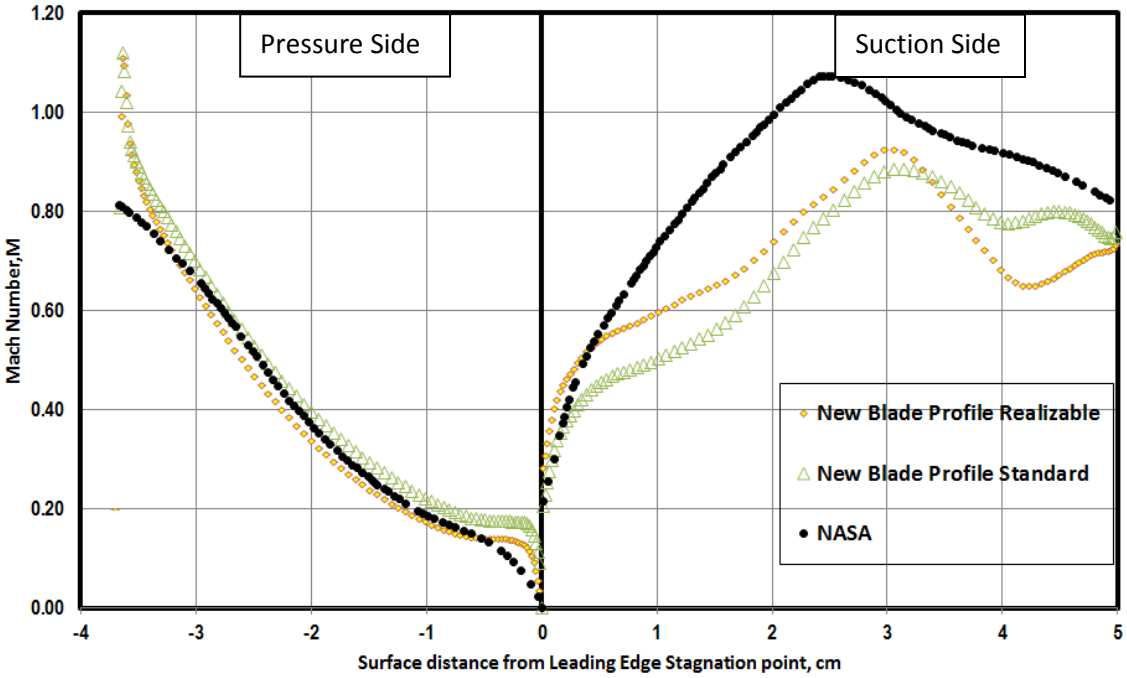

Figure 76- Mach number plot using k-epsilon model

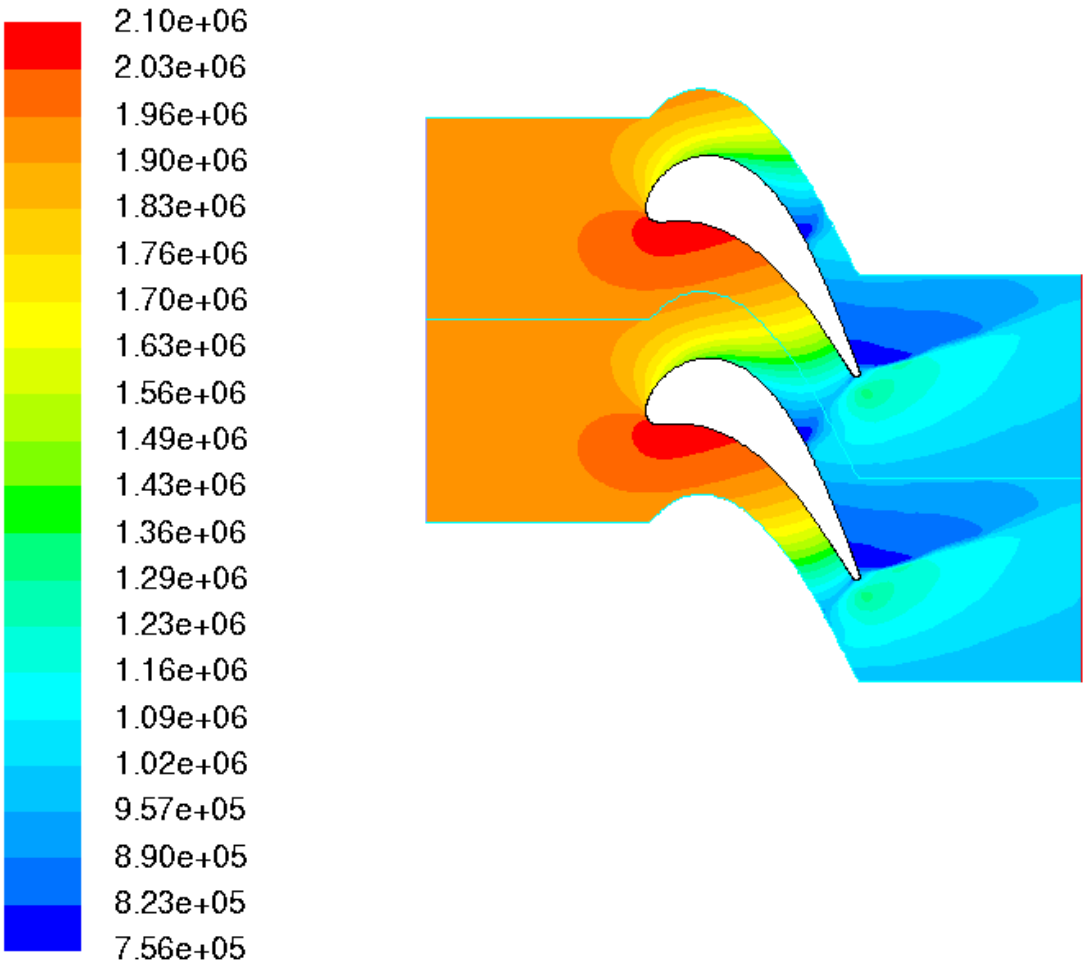

Figure 77– Contours of static pressure for 2D mesh, SST-Transition

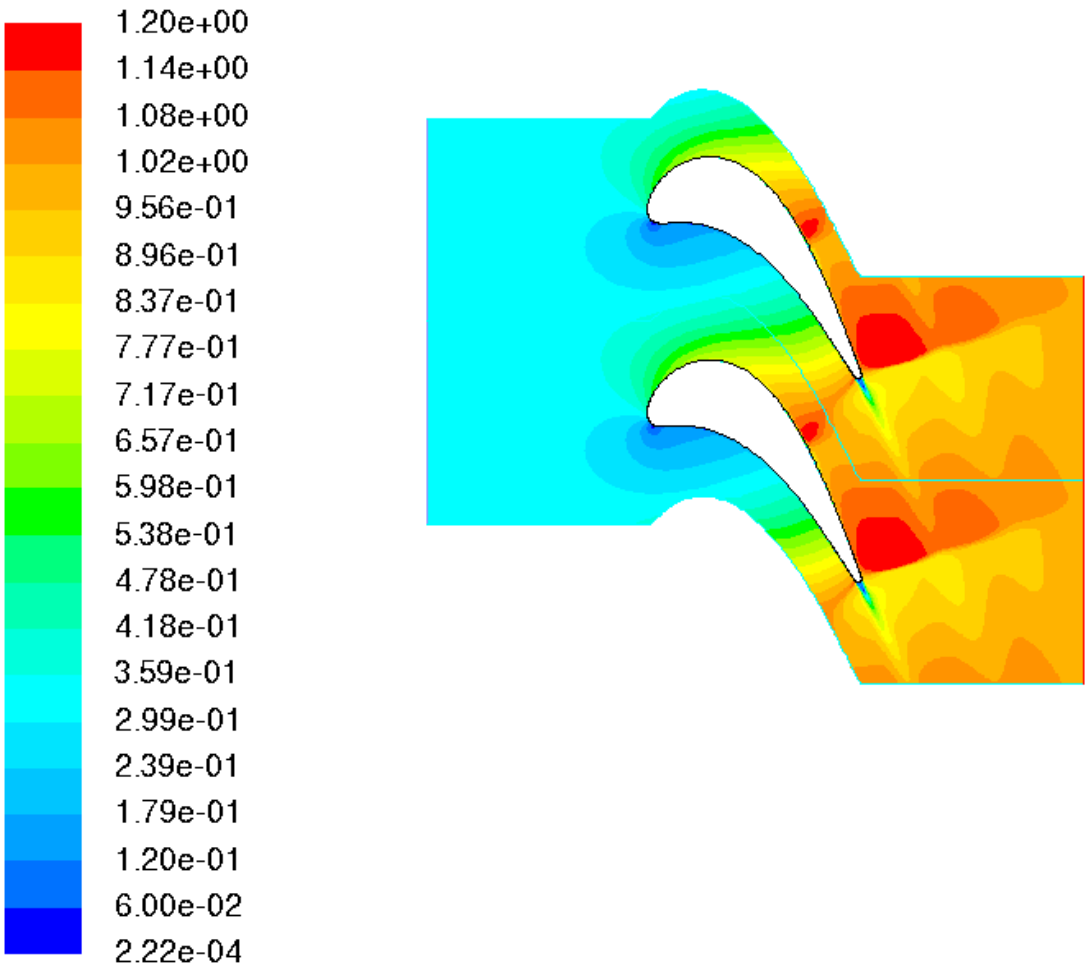

Figure 78– Contours of Mach number for 2D mesh, SST-Transition

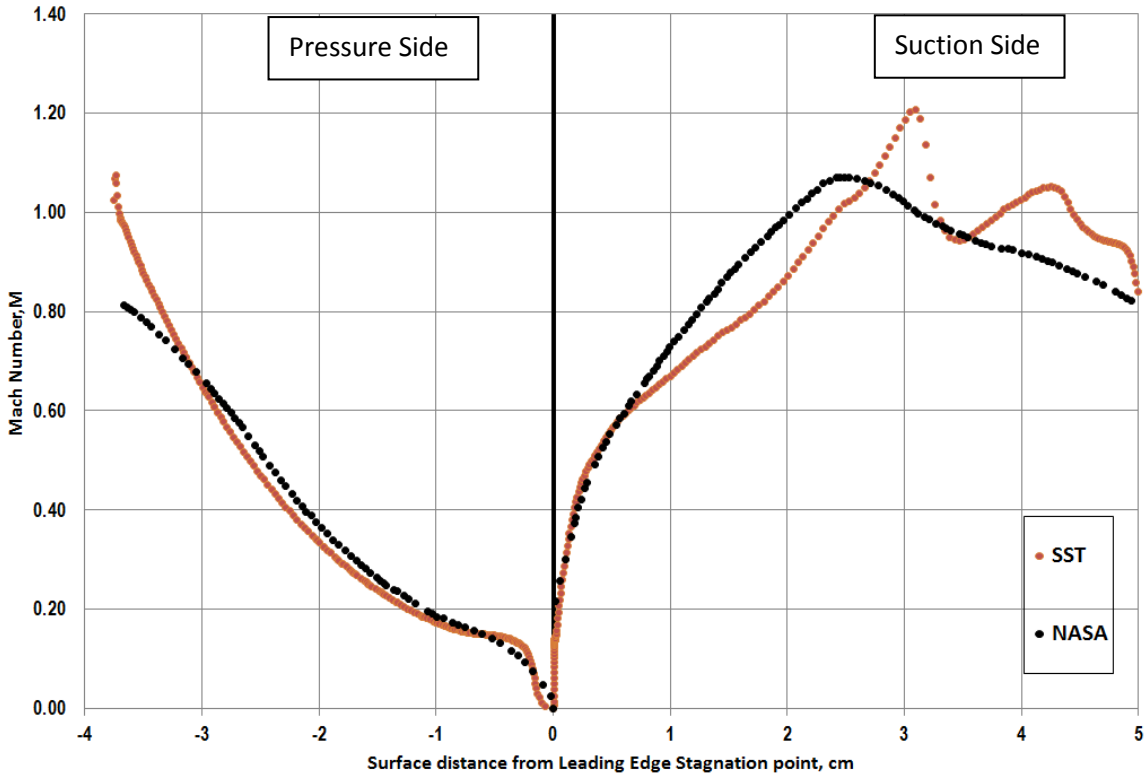

Figure 79– Mach number plot using SST-Transition model, 2D mesh

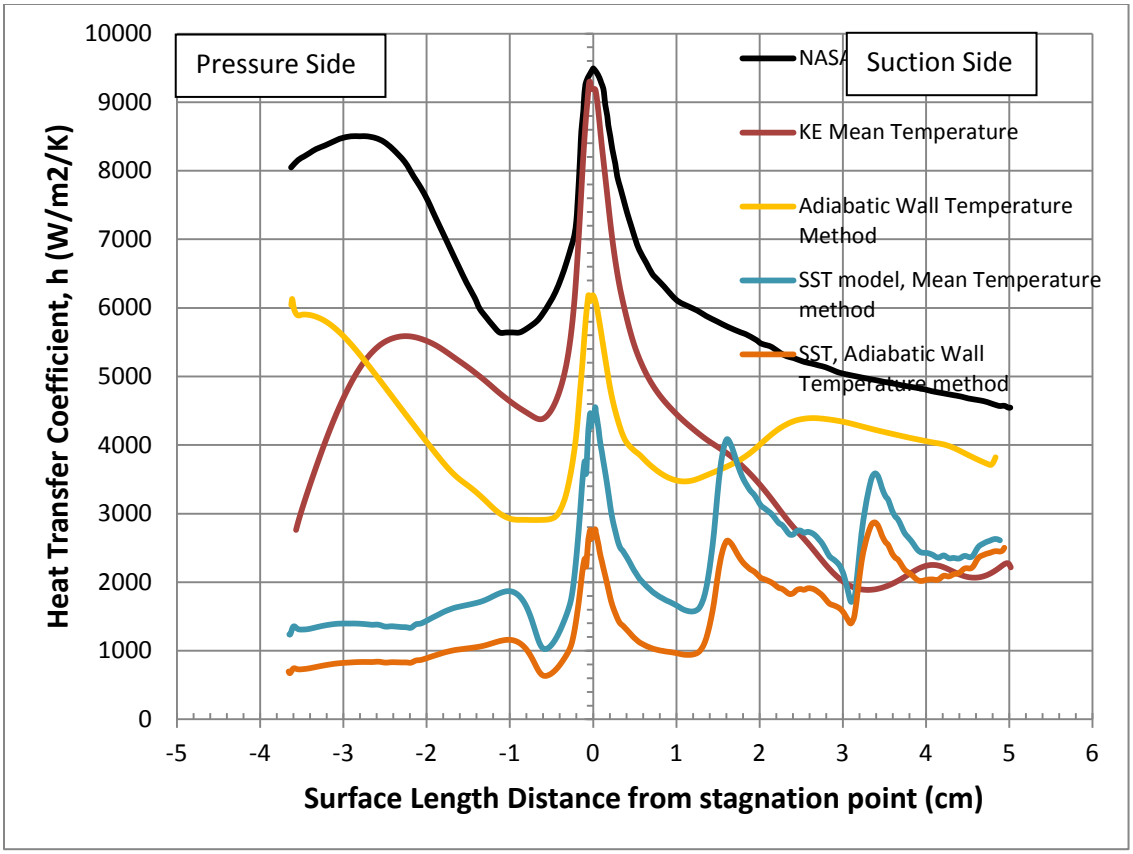

Figure 80– Heat transfer coefficient around the blade from different models, 2D mesh

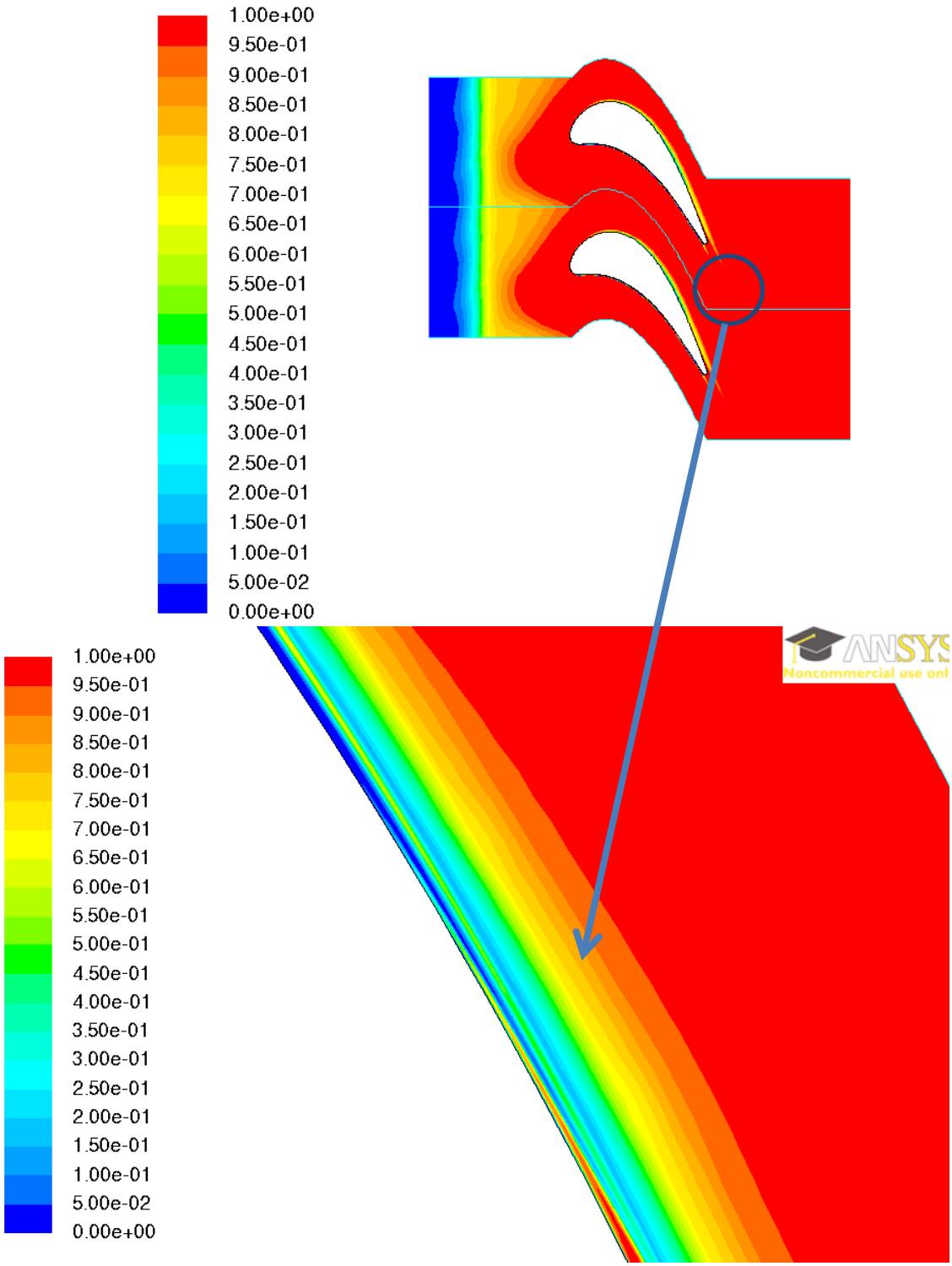

Figure 81-Contours of intermittency near the transition location, 2D mesh

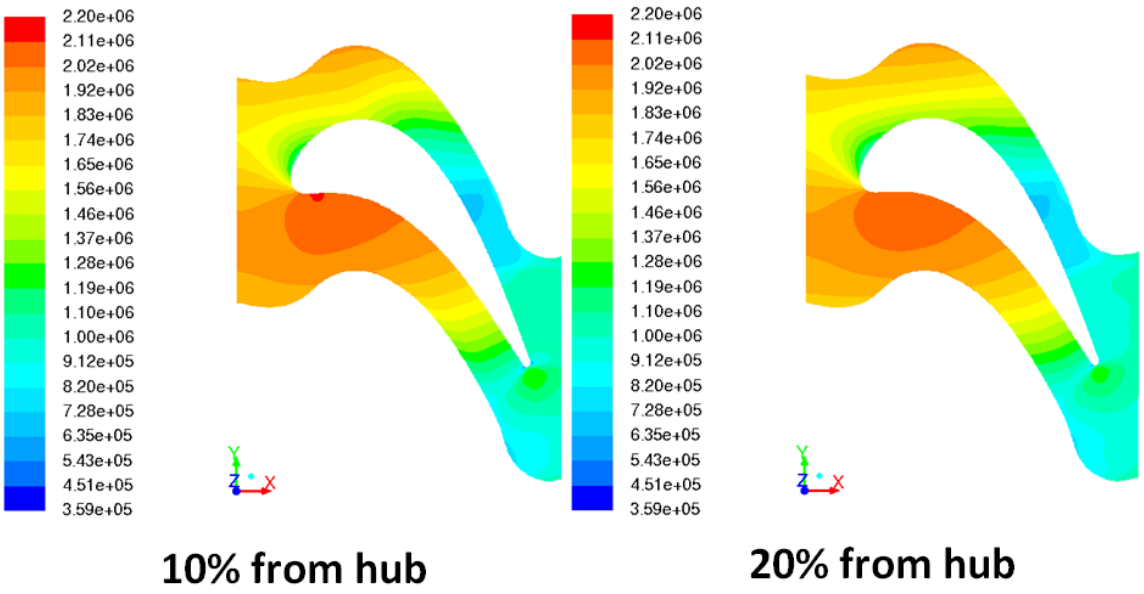

Figure 82– Contours of static pressure close to hub portion , 3D mesh

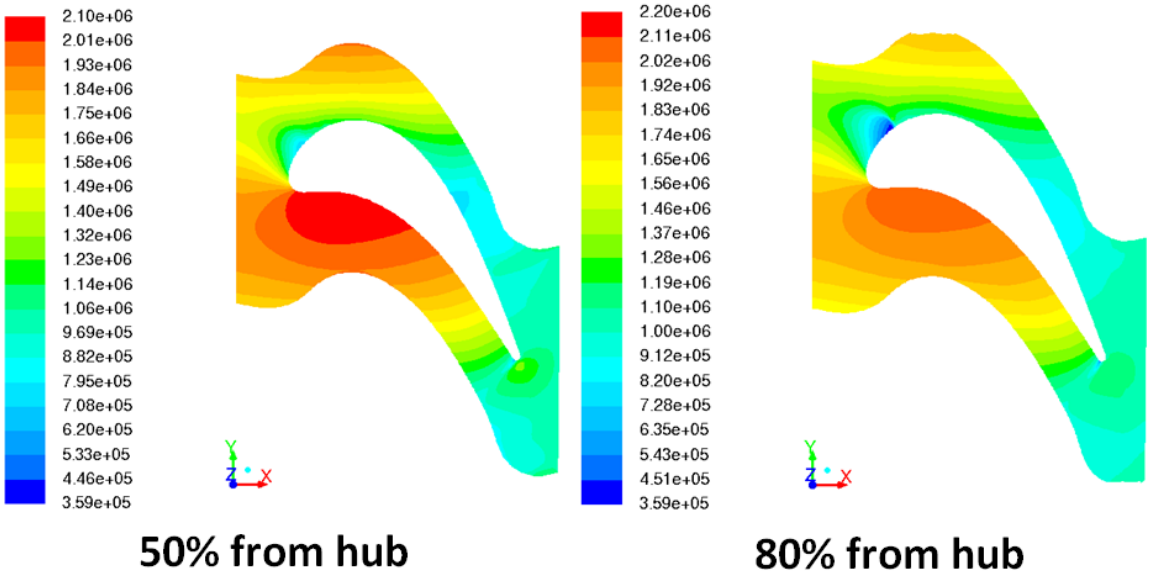

Figure 83– Contours of static pressure in midspan and close to tip, 3D mesh

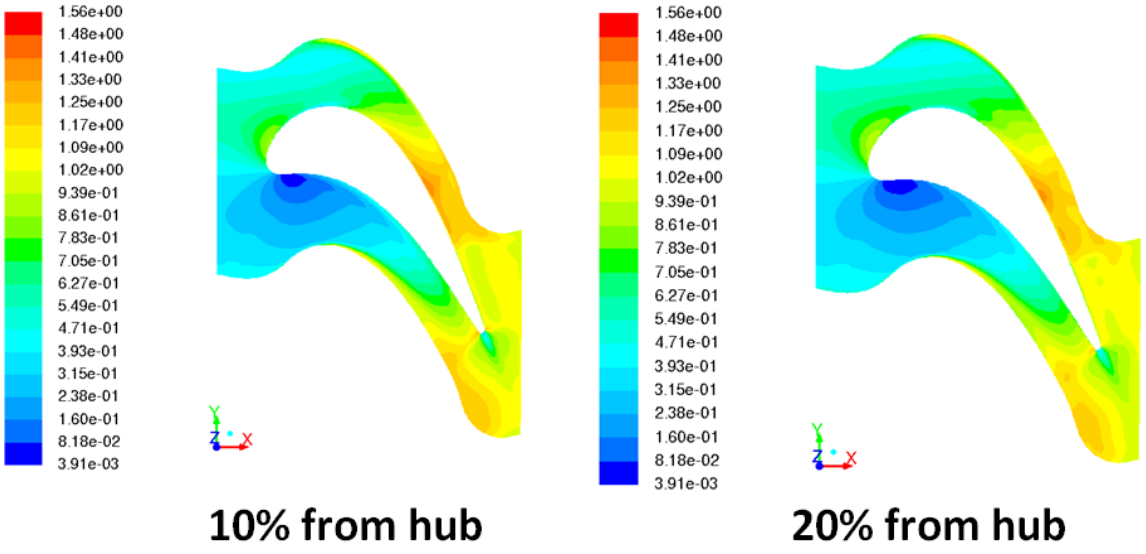

Figure 84– Contours of Mach number, 3D mesh, 10% and 20% distance

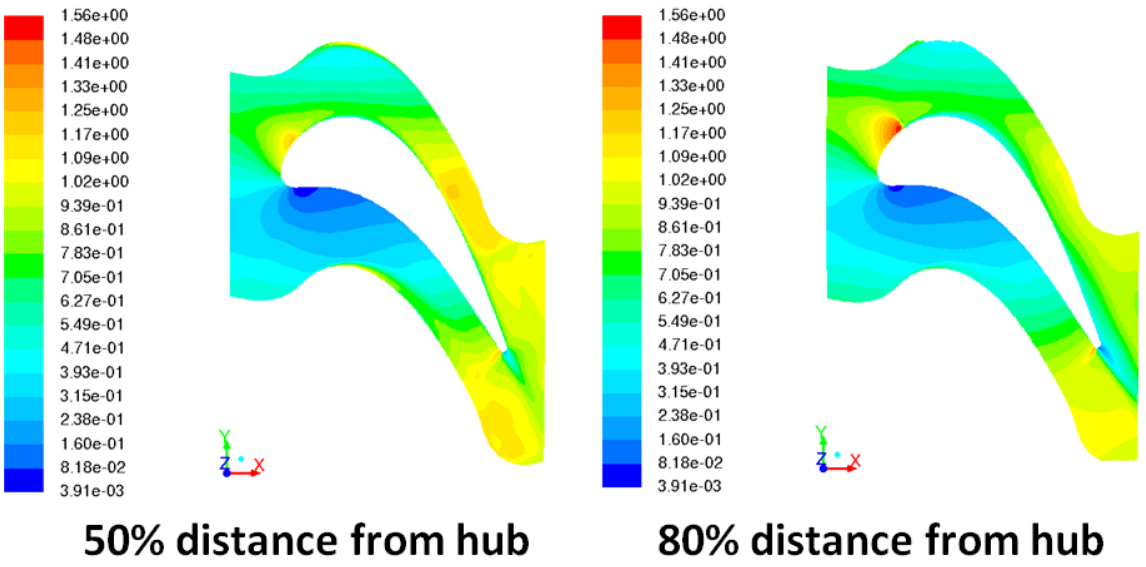

Figure 85– Contours of Mach number, 3D mesh, 50% and 80% distance

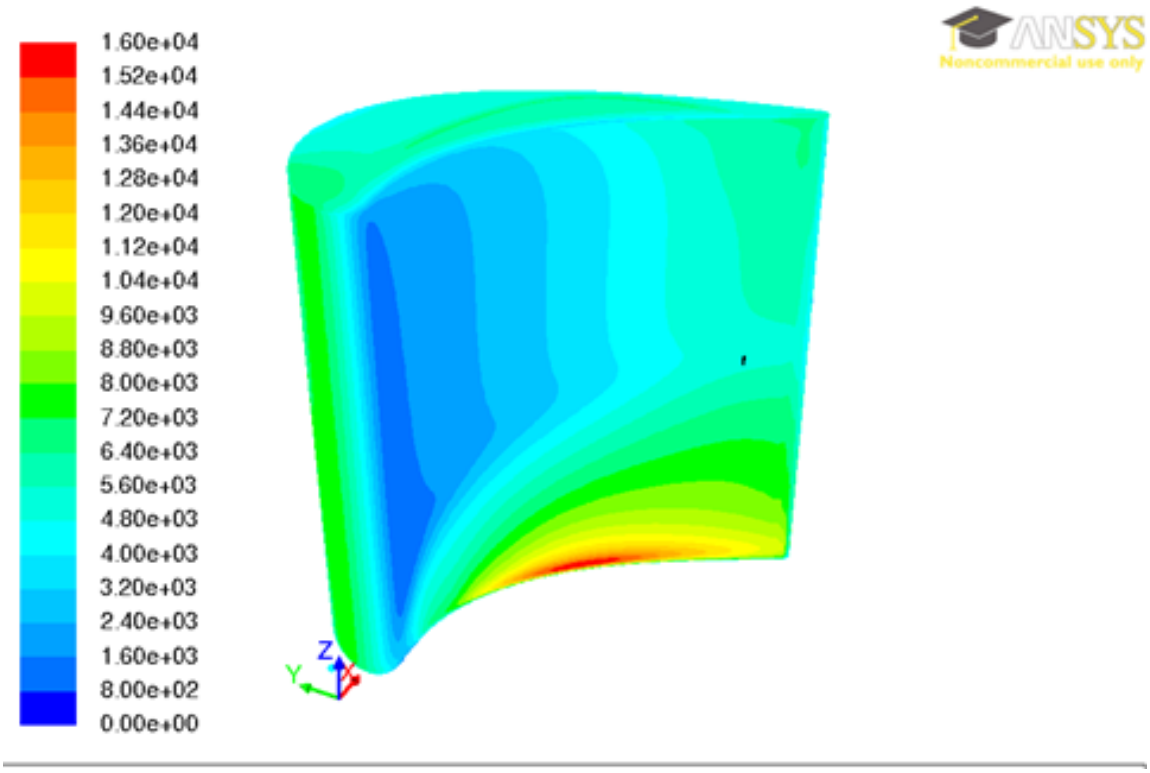

Figure 86– Contour plot of heat transfer coefficient on pressure side

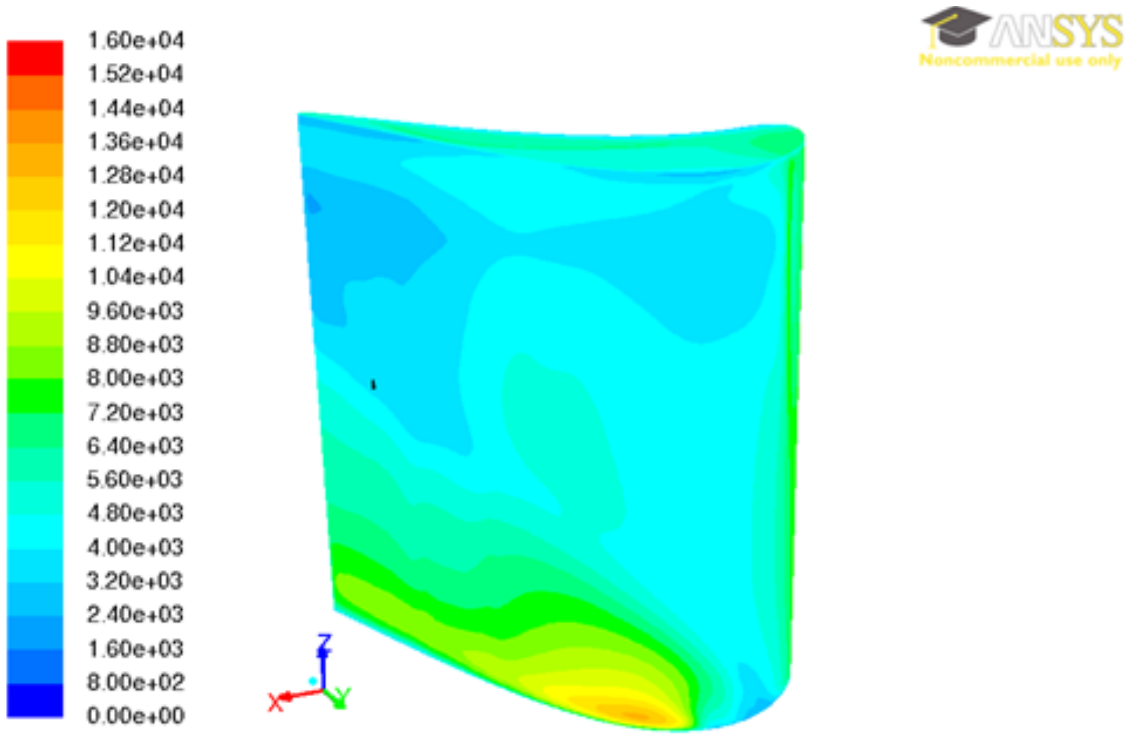

Figure 87– Contour plot of heat transfer coefficient on suction side

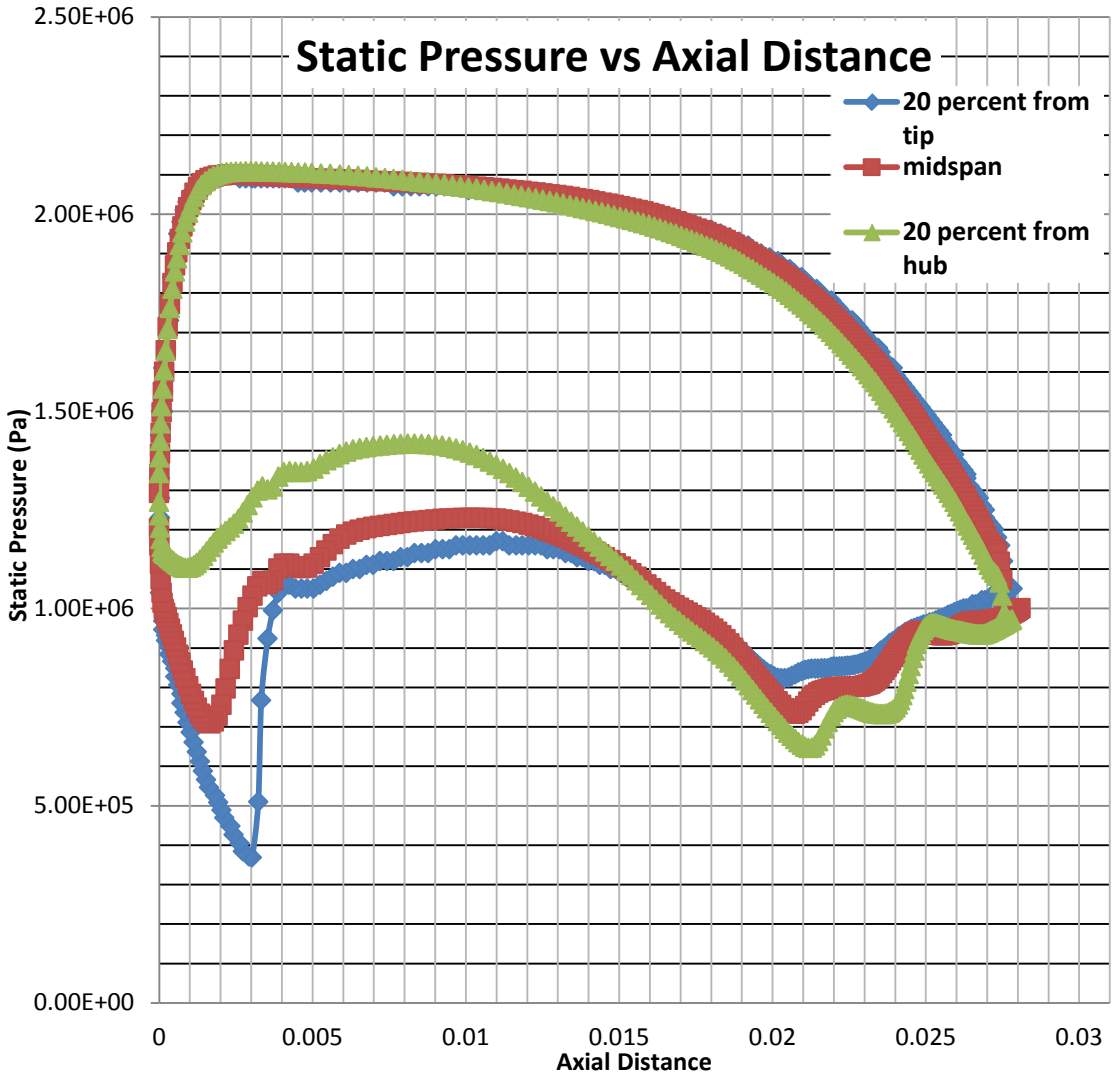

Figure 88– Pressure distributions from near-hub to near-tip locations

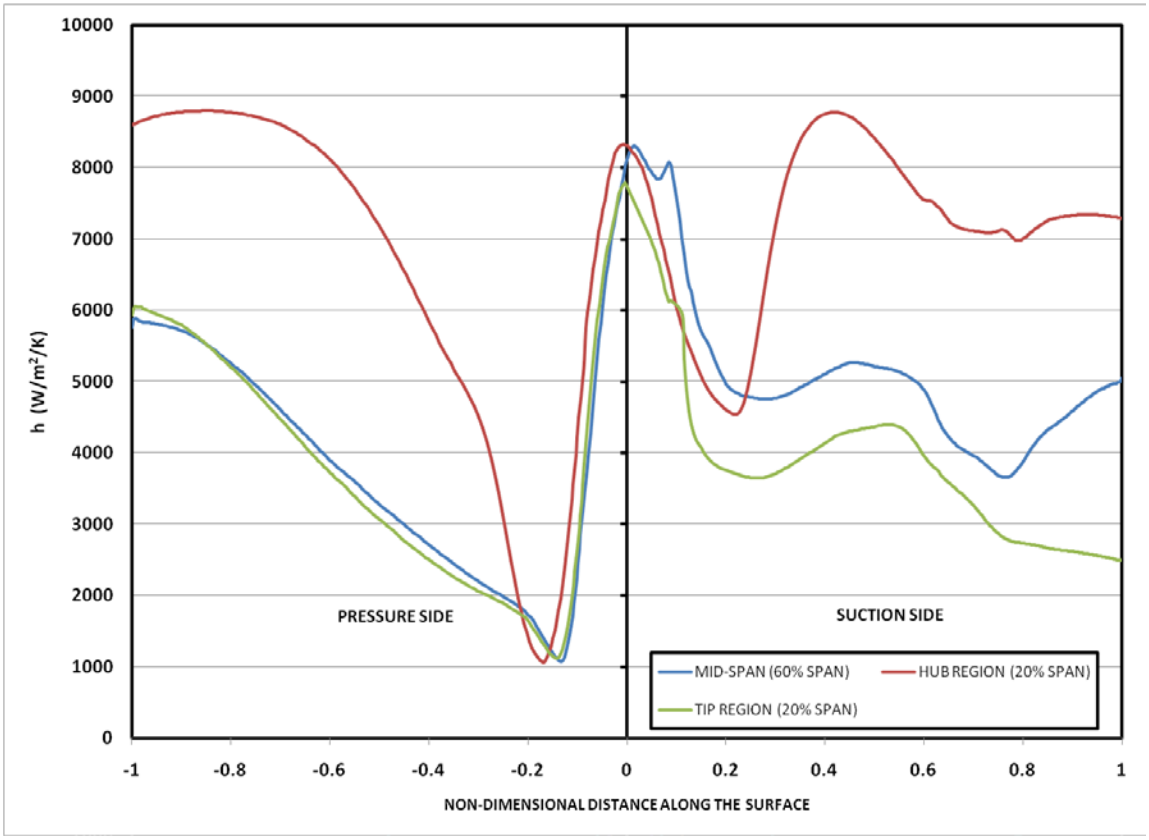

Figure 89– Heat transfer coefficient distributions near hub, midspan and tip of the blade

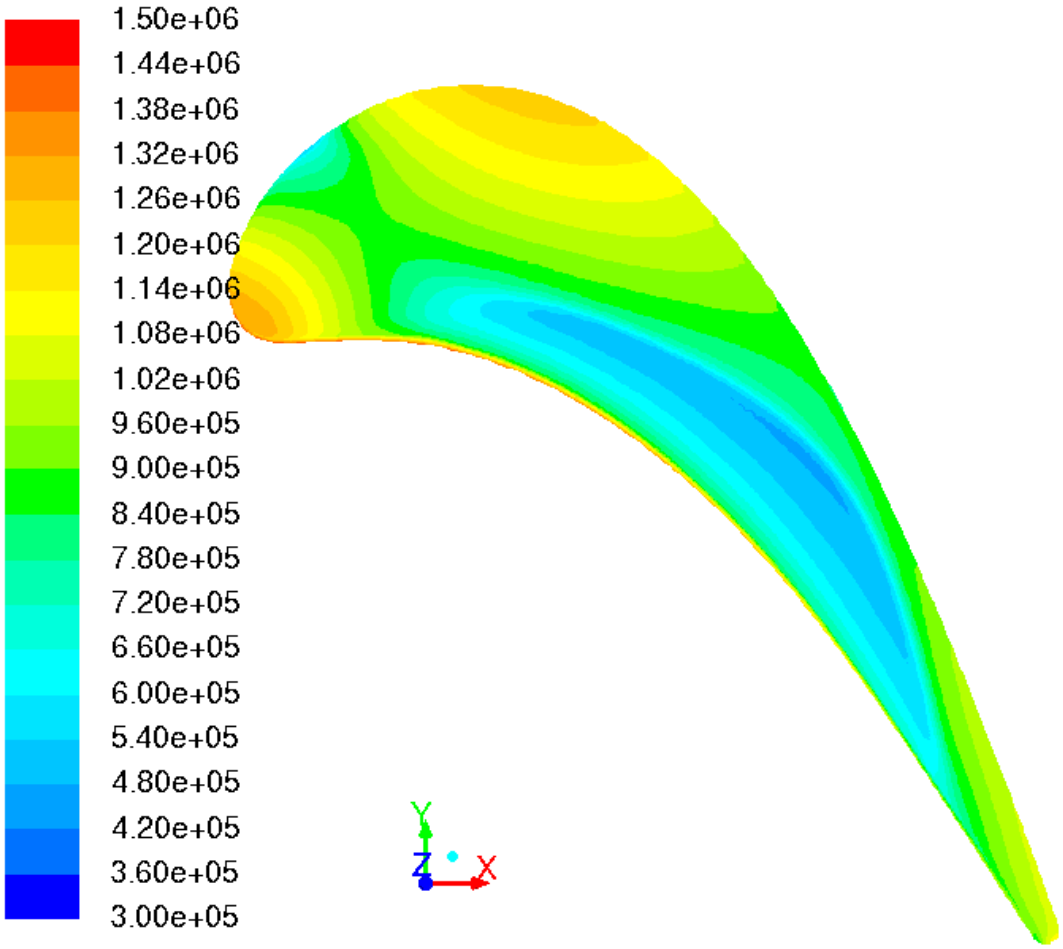

Figure 90– Contours of static pressure for the tip clearance of 0.5 mm and inlet Tu of 15%

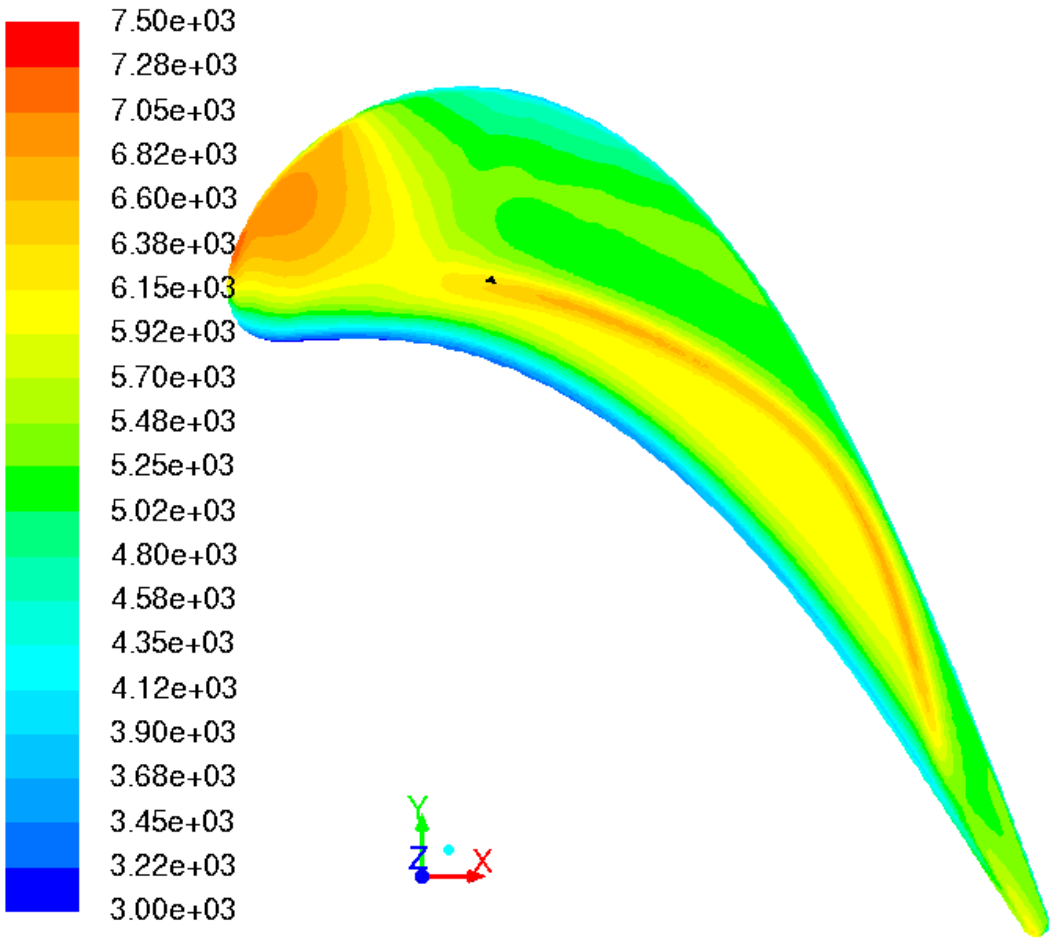

Figure 91– Contours of heat transfer coefficient for the tip clearance of 0.5 mm and inlet Tu of 15%

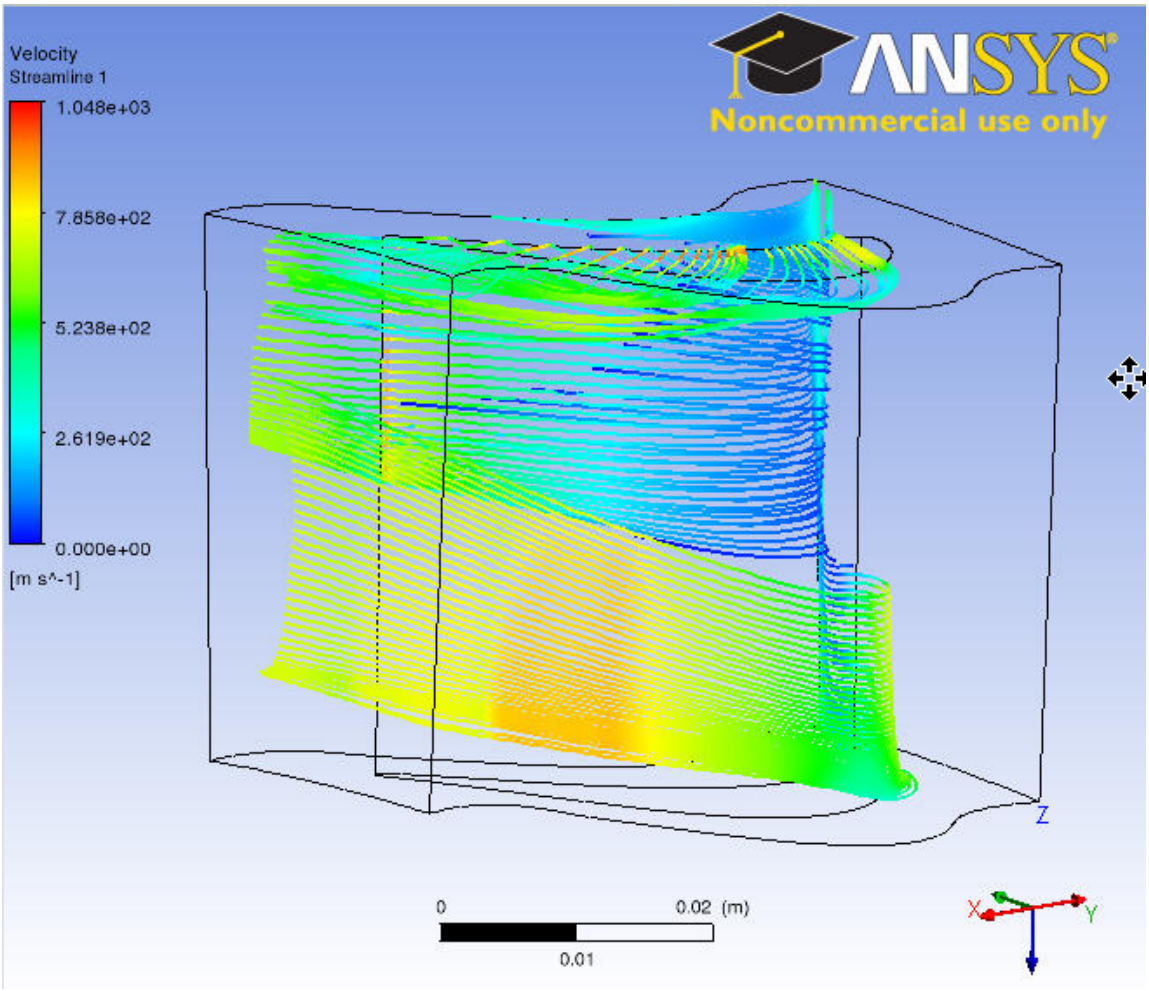

Figure 92– Streamlines on suction side and pressure side, view from suction side

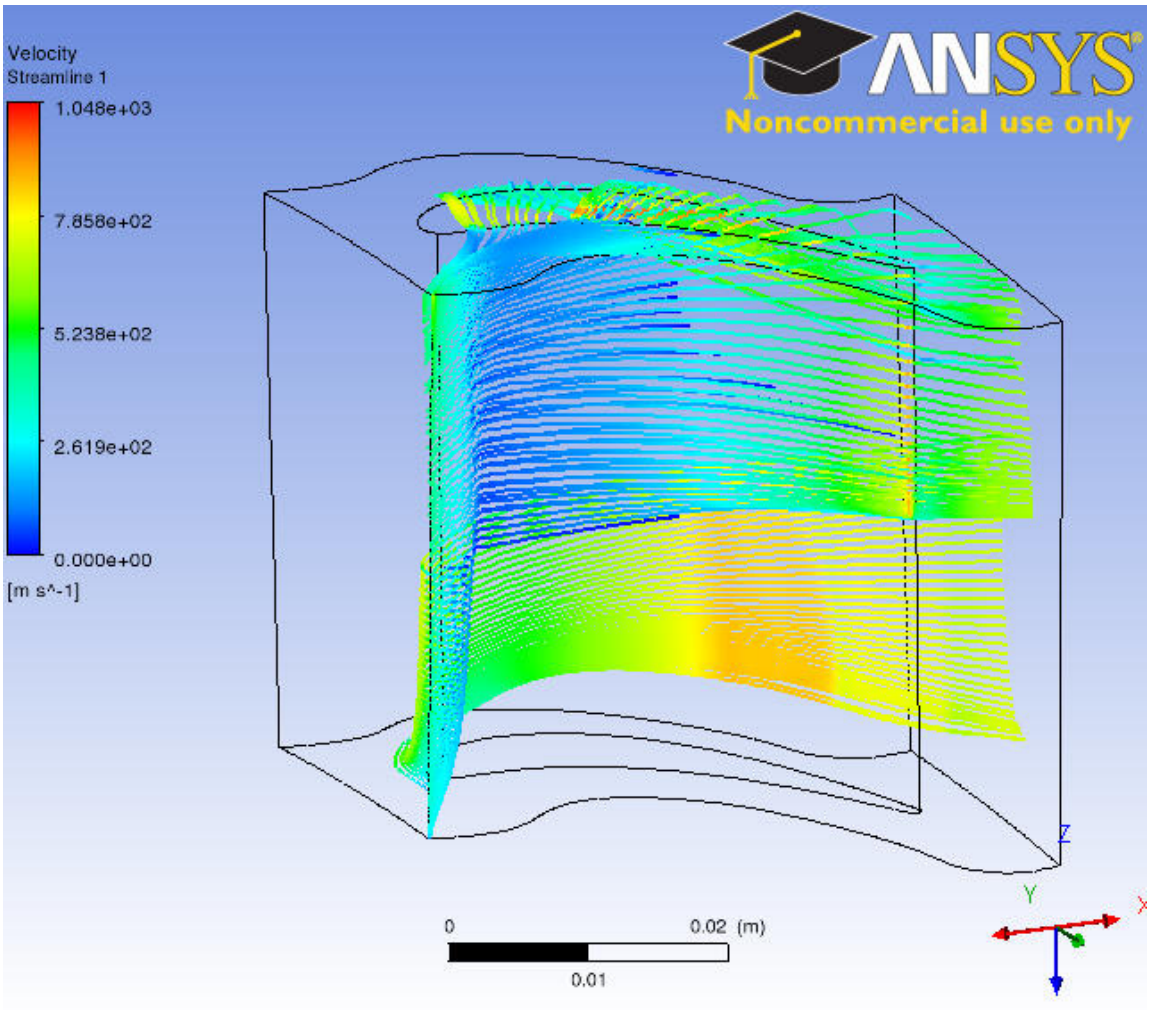

Figure 93– Streamlines on suction side and pressure side, view from pressure side

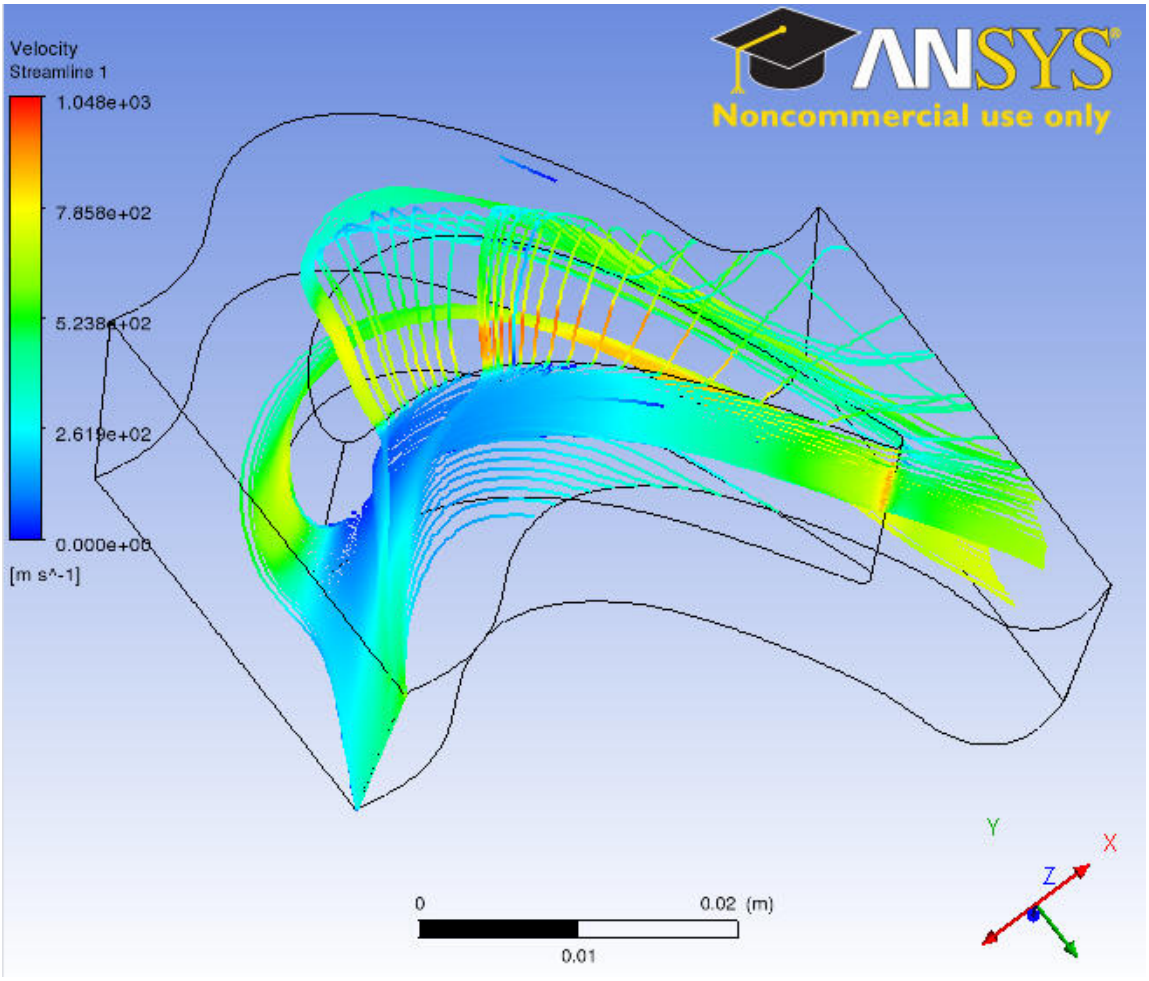

Figure 94– Streamlines on tip of the blade, view from top

Backward Loop, from Trailing Edge to Mid-Chord

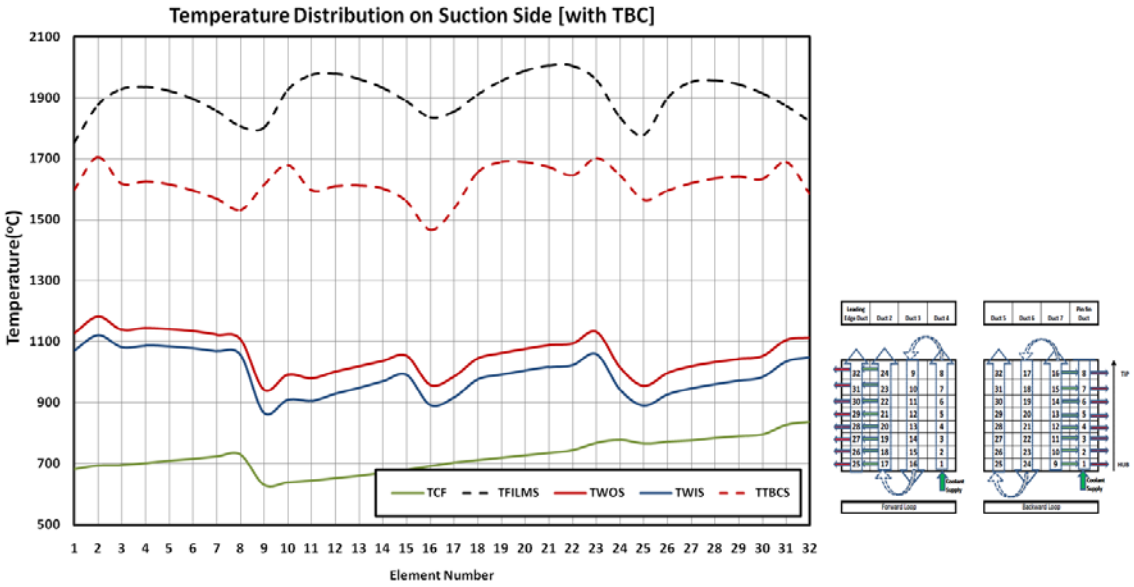

Figure 95– Temperature distribution on suction side for RIT = 1700°C, Backward Loop, Case V

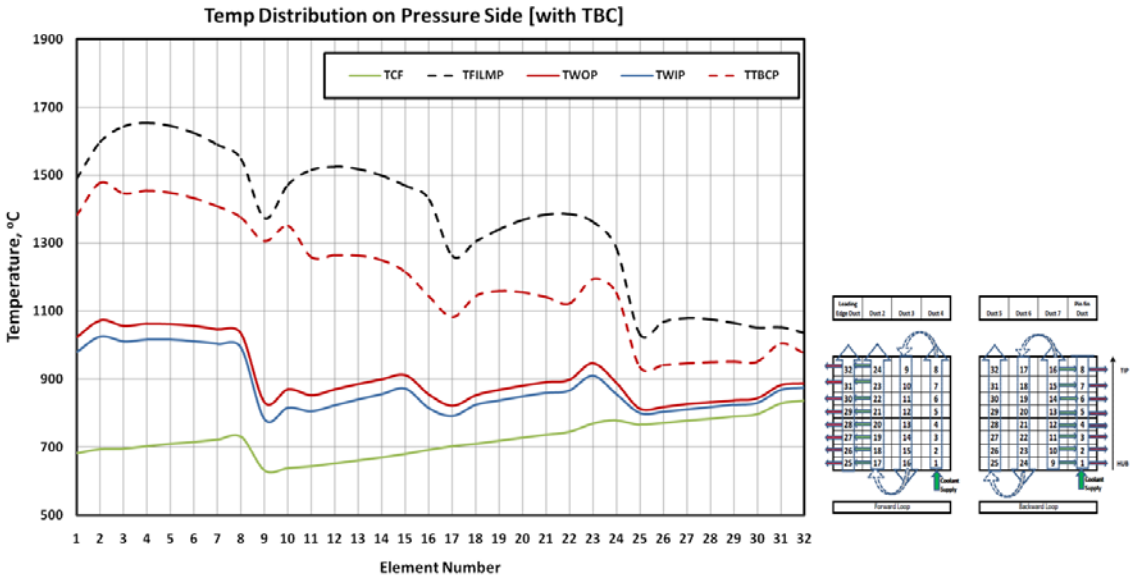

Figure 96– Temperature distribution on pressure side for RIT = 1700°C, Backward Loop, Case V

Forward Loop, from Mid-Chord to Leading Edge

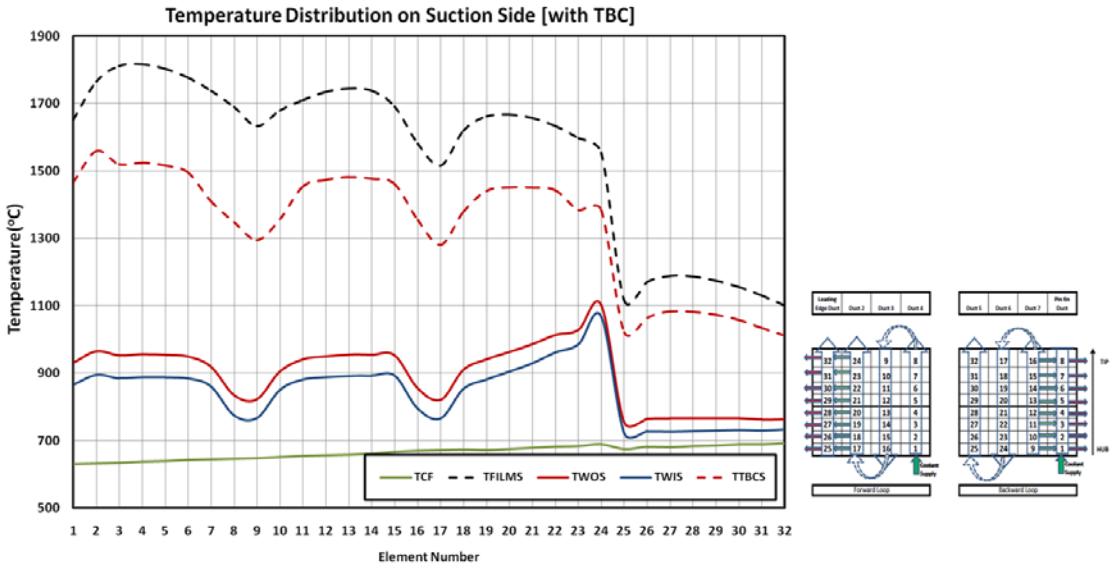

Figure 97– Temperature distribution on suction side for RIT = 1700°C, Forward Loop, Case V

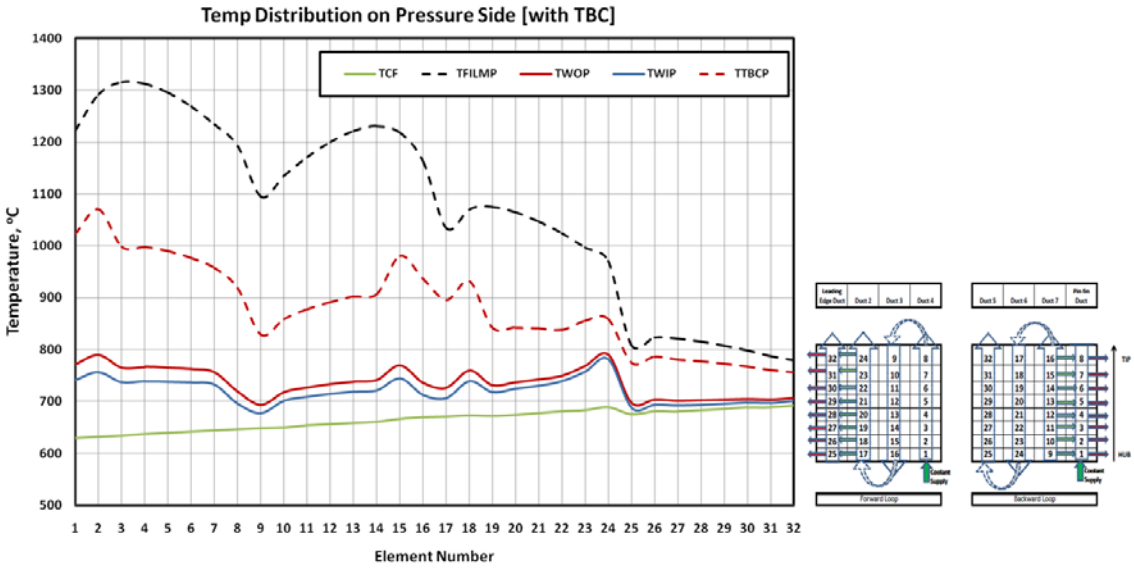

Figure 98– Temperature distribution on pressure side for RIT = 1700°C, Forward Loop, Case V

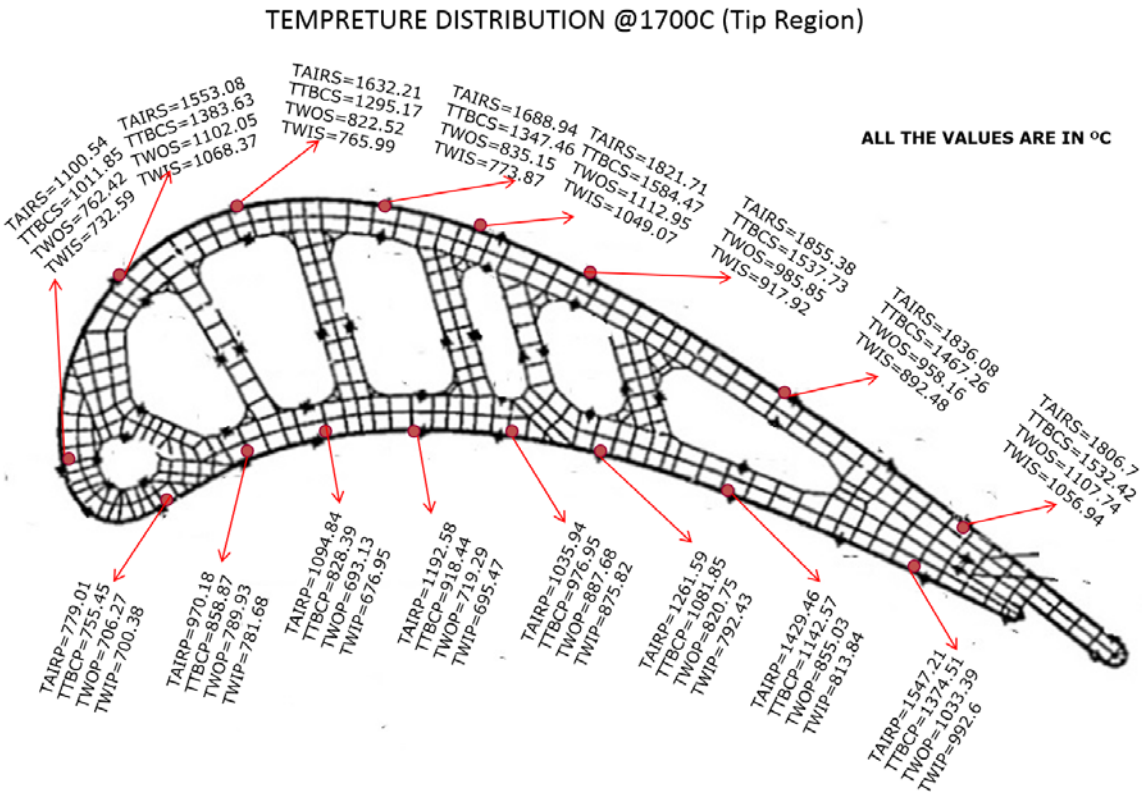

Figure 99– A tip region temperature distribution for the rotor inlet temperature of 1700^{o}C using CFD results for heat transfer coefficient, Case V

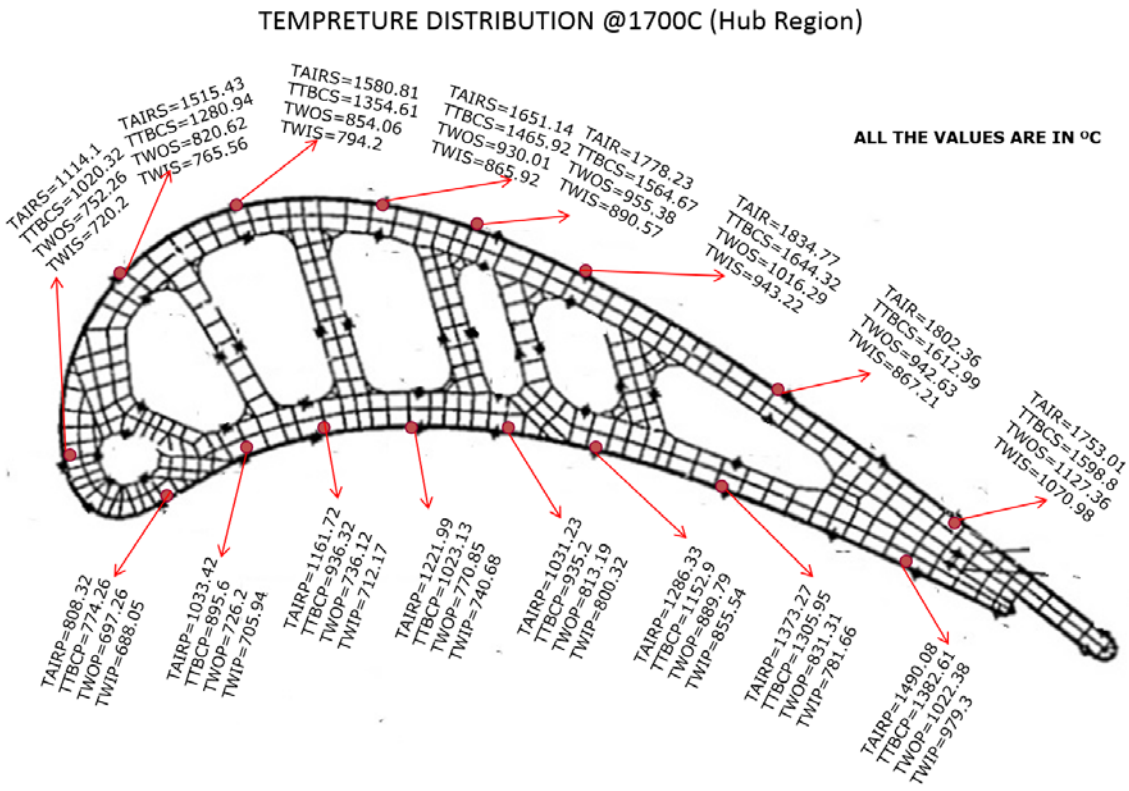

Figure 100– A hub region temperature distribution for the rotor inlet temperature of 1700^{o}C using CFD results for heat transfer coefficient, Case V

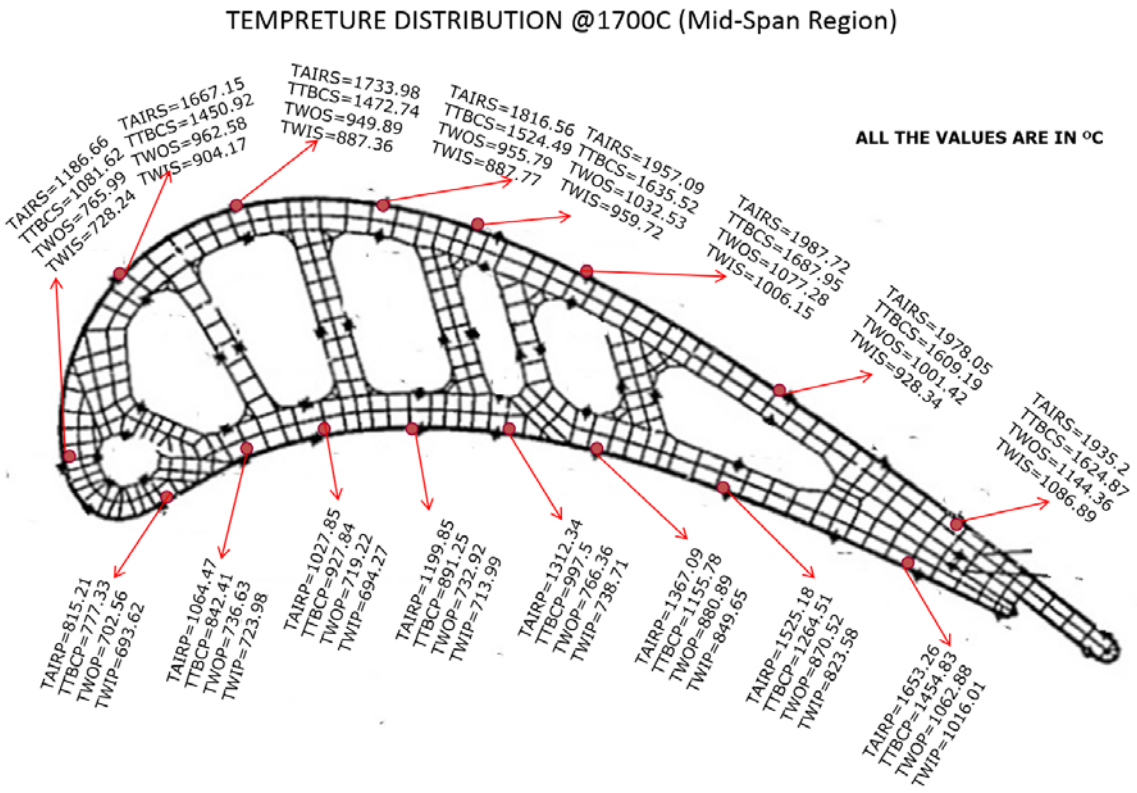

Figure 101– A pitch region temperature distribution for the rotor inlet temperature of 1700^{o}C using CFD results for heat transfer coefficient, Case V